Dissertation

submitted to the

Combined Faculties of the Natural Sciences and Mathematics

of the Ruperto-Carola-University of Heidelberg, Germany

for the degree of

Doctor of Natural Sciences

Put forward by

Pak Hin, Tam

born in: Hong Kong

Oral examination: 17 December 2008

Gamma-ray burst studies using the H.E.S.S. Cherenkov array

Referees: Prof. Dr. Stefan Wagner

Prof. Dr. John Kirk

Kurzfassung

Gammastrahlenblitze (engl. gamma-ray bursts, GRBs) sind gewaltige Ausbrüche der Gammaquanten ($\sim 10^5 - 10^6$ eV), die im Universum entstehen. Eine große Menge Energie wird sekundenschnell ausgelöst. Mit dieser Energie werden Teilchen beschleunigt und Gammastrahlung erzeugt. Gleichzeitig oder gleich nach dem Blitz kann das Emissionsgebiet sehr hochenergetische (engl. very-high-energy, VHE; $\gtrsim 10^{11}$ eV) Gammastrahlung erzeugen, die aber wegen anderer Gammas und des extragalaktischen Hintergrundlichts (engl. extragalactic light, EBL) auf ihrem Weg zur Erde abgeschwächt werden könnten. H.E.S.S. ist eine aus vier abbildenden Tscherenkow-Teleskopen bestehende Anlage in Namibia, die für VHE-Gammastrahlung empfindlich ist. Beobachtungen von 34 GRBs mit H.E.S.S. zwischen 2003 und 2008 wurden ausgeführt. Die meisten Beobachtungen fingen einige Minuten bis Stunden nach dem GRBs an. Kein Beweis für VHE-Gammastrahlung wurde geliefert. Im Rahmen eines relativistischen Expansionswelle-Modells werden die Flüssen aus der Synchrotron-Selbst-Comptonisierung (SSC) mit der experimentellen Daten von GRB030329 und GRB060505 vergleichen. Das Modell ist mit den Daten kompatibel. Wechselwirkungen mit dem EBL wurden berücksichtigt. GRB060602B wurde während seiner ganzen Zeitdauer zufällig von H.E.S.S. beobachtet, wobei kein Beweis für VHE-Gammastrahlung gefunden wurde. Die Entfernung und der Ursprung des GRB060602B bleiben jedoch unklar. Darum werden verschiedenen Möglichkeiten und deren Auswirkungen diskutiert. In der vorliegenden Arbeit wird versucht, eine Aussicht auf die Messung der VHE-Gammastrahlung aus den GRBs zu geben.

Abstract

Gamma-ray bursts (GRBs) are the most intense and unpredictable γ-ray events from the Universe. Without prior signal, an enormous amount of energy is released for seconds, energizing particles and generating the observed $10^5 - 10^6$ eV γ-ray photons. The emitting regions can produce Very-High-Energy (VHE) γ-ray photons of energy $\gtrsim 10^{11}$ eV during and after the burst. These VHE γ-rays may be attenuated in the source or by the extragalactic background light (EBL). The H.E.S.S. array of four imaging atmospheric Cherenkov telescopes (IACT) is sensitive to VHE γ-rays. H.E.S.S. observations of 34 GRBs were carried out during 2003–2008, with the shortest response time being six minutes. No evidence of VHE γ-rays was found. Flux upper limits derived for GRB030329 and GRB060505 are compared and are found consistent with the synchrotron self-Compton flux calculated in the context of relativistic blast-wave model. Absorption by EBL was taken into consideration. Accidentally, GRB060602B was observed with H.E.S.S. throughout the GRB duration, during which no signal of VHE γ-rays was found. The distance scale and origin of GRB060602B remain unclear and different possibilities and implications are presented. Future prospects of VHE γ-ray observations of GRBs are discussed.

Contents

List of Figures

List of Tables

Chapter 1

Introduction

The gamma-ray sky at energies higher than $\sim$100 GeV (i.e., the very-high-energy, or VHE, γ-ray regime) looks very different from what is seen with the naked eyes. The matter able to generate these energetic photons is believed to be highly-relativistic. Gamma-ray bursts (GRBs) are very likely to be generated by highly-relativistic matter. Let us first start with a brief overview of the known extragalactic VHE universe. This is followed by a short presentation of GRB observations, with an emphasis on our knowledge of GRBs as obtained using different γ-ray instruments over the last decade.

1.1 The expanding VHE gamma-ray universe

The first VHE gamma-ray source on the sky — the Crab Nebula — was detected about 20 years ago (Weekes et al., 1989), followed by the detection of the first extragalactic VHE gamma-ray source Markarian 421 (Punch et al., 1992). Subsequently, the known horizon of the VHE gamma-ray universe has increased from $\sim$0.2 kpc to at least $\sim$1 Gpc[1] nowadays (or $\sim$3 Gpc if 3C 279 was actually detected, Albert et al., 2008). The growing VHE γ-ray horizon over the years is shown in Figure 1.1.

As of mid-2008, the known VHE gamma-ray sky consists of about 20 extragalactic objects[2] (Aharonian et al., 2008b). All of them are active galactic nuclei, including BL Lac objects, a radio galaxy (M 87), and (possibly) a Flat Spectrum Radio Quasar (3C 279). On the other hand, other extra-galactic objects, including normal galaxies, galaxy clusters, and GRBs, are also predicted to emit VHE gamma-rays. GRBs, however, can be extremely intense in VHE gamma-rays as predicted in some models (see Chapter 2 for a review), and therefore may be detected even if they are located at high redshifts. Therefore, it is possible that GRBs will become the most distant VHE gamma-ray sources in the future.

---

[1]This luminosity distance D_{L} corresponds to $z = 0.212$, the redshift of 1ES 1011+496 (Albert et al., 2007a). A cosmology of $\Omega_{\mathrm{M}} = 0.27$, $\Omega_{\mathrm{V}} = 0.73$, and $H_0 = 71\,\mathrm{km\,s^{-1}\,Mpc^{-1}}$ is used.

[2]together with more than 50 Galactic objects
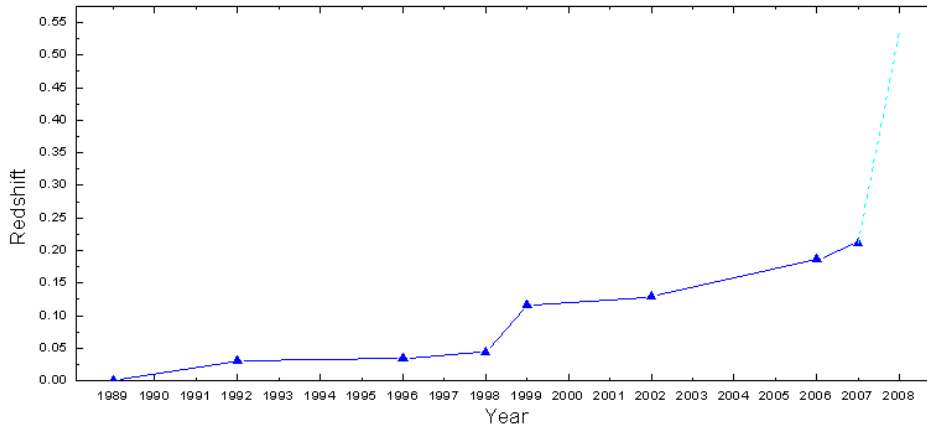
Figure 1.1: Redshifts of the most distant VHE γ-ray emitting objects (with known red-shifts) from 1989 to 2008. The dates were taken from the publication year of the article in major scientific journals where the discovery of the object was first reported. The tri-angles represent the redshifts of the following objects: Crab Nebula (Weekes et al., 1989), Markarian 421 (Punch et al., 1992), Markarian 501 (Quinn et al., 1996), 1ES 2344+514 (Cantanese et al., 1998), PKS 2155-304 (Chadwick et al., 1999), H1426+428 (Horan et al., 2002), 1ES 1101-232 (Aharonian et al., 2006d), and 1ES 1011+496 (Albert et al., 2007a). A detection of 3C 279 at a significance level of $\sim5\sigma$ was reported by the MAGIC Collaboration in 2008, based on the data from 2006 only (Albert et al., 2008).

1.2 A short history of gamma-ray bursts

Gamma-ray bursts (GRBs) are the most intense events in the γ-ray sky. The energy fluence of a GRB is about $10^{-3} - 10^{-8}$ erg cm^{-2} in the soft γ-ray range. Once per day, a GRB shines from any random direction on the sky, lasting for ~10 ms to ~1000 s and never happen again.

Historically, when bursts of gamma-rays were first recorded with Vela satellites in the range of 0.2–1.5 MeV in late 1960s, the term *gamma-ray bursts* was used to refer to them (Klebesadel et al., 1973). *X-ray bursts* refer to another phenomenon discovered in 1975 which peaks at energies smaller than 10 keV (Belian et al., 1976; Grindlay et al., 1976). Figure 1.2 shows typical spectral energy distributions (SED) of these two phenom-ena, together with that of a soft gamma repeater. The nature of X-ray bursts was swiftly understood as thermonuclear reaction on the surface of neutron stars in 1976 (Lewin et al., 1995). In contrast, the advances in understanding GRBs have taken a much longer time. For example, in a review paper by Ruderman (1975), the number of proposed theories was more than the number of then-detected GRBs! A major obstacle is that, during the three decades since the discovery of GRBs, no counterpart in other waveband had been identified. GRBs remained 'dark' in all other wavebands in the electromagnetic spectrum.

Our understanding of GRBs has improved tremendously after the discovery of X-ray and optical afterglows which led to the identification of the GRB host galaxies (van Paradijs et al., 2000). This highlights the fact that obtaining multi-wavelength informa-
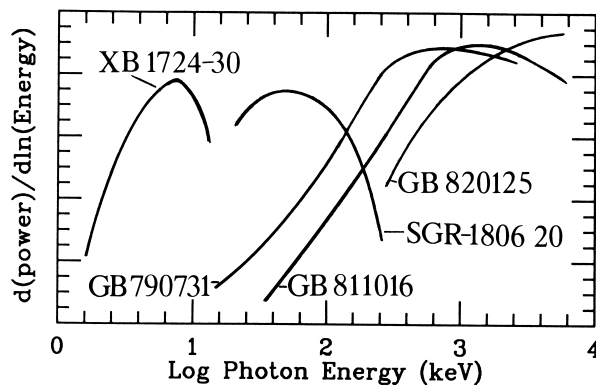
Figure 1.2: An illustrative spectral energy distribution of X-ray bursts, γ-ray bursts, and soft gamma repeater (from Hartmann & Woosley, 1988).

Table 1.1: Gamma-rays in various energy bands, after Weekes (2003)

γ-ray energy	low to medium	high	very high	ultra high
Band (eV)	$10^5 - 3 \times 10^7$	$3 \times 10^7 - 10^{11}$	$10^{11} - 10^{14}$	$> 10^{14}$
Type of detectors	solid state	silicon strip	air Cherenkov	particle shower
Place of detectors	satellite	satellite	ground	ground

tion of GRBs is extremely important to understand their origin and properties.

1.3 Gamma-ray bursts as a broad-band gamma-ray phenomenon

The electromagnetic spectrum above $\sim$100 keV (the γ-ray band) spans at least nine orders of magnitude. It can be sub-divided into four energy regimes based on the detection principles, as shown in Table 1.1. Note that the division lines between adjacent regimes are somewhat arbitrary and there exist overlapping regions where different types of detectors can observe. For example, while the space-based Fermi/LAT detector[3] is expected to detect photons up to $\sim$300 GeV, ground-based Imaging Atmospheric Cherenkov telescopes (IACTs) have proved to lower their energy thresholds to $\lesssim$100 GeV.

The observational status of GRB spectra as obtained by γ-ray instruments is reviewed in the order of: low to medium energy (below 30 MeV), high energy (30 MeV to 100 GeV), and very high energy (above 100 GeV). As we shall see, GRBs are registered in the low to medium energy band, while some more energetic GRBs are also detected in the high energy band, but a firm detection in the VHE band has yet to be established.

---

[3]The Fermi Gamma-ray Space Telescope (FGST) was called GLAST before its launch on June 11, 2008
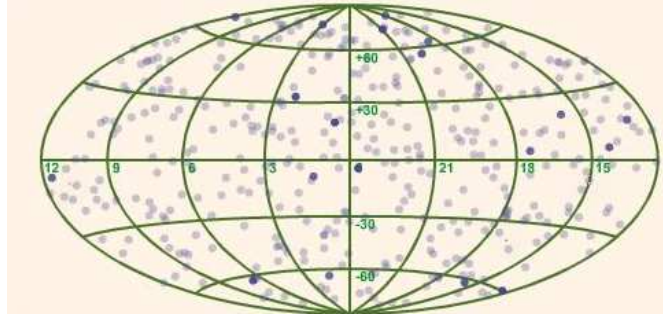
Figure 1.3: Spatial distribution of GRBs detected by *Swift*/BAT over four years of operation. Blue dots indicate those detected between May 23, 2008 and July 15, 2008. The isotropic property of the distribution is apparent (retrieved from http://grb.sonoma.edu).
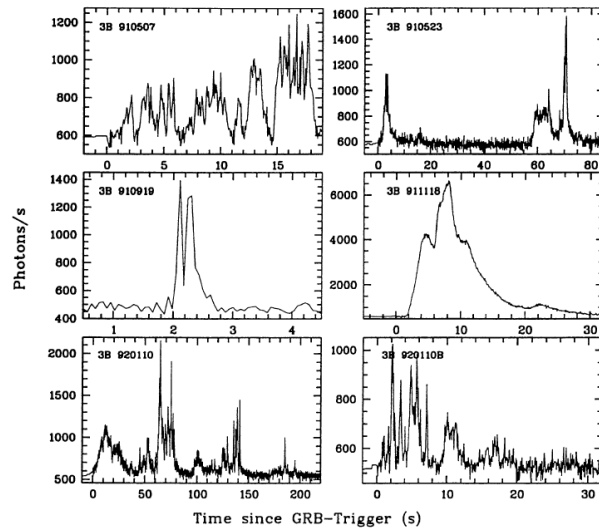
Figure 1.4: Large variety of temporal structure observed in GRBs (from Greiner, 1999)

1.3.1   Burst emission below 30 MeV

During the years when BATSE was in operation, two establishments were made, namely the isotropic distribution of GRBs (see Figure 1.3) and the classification of short/hard and long/soft GRBs (Fishman & Meegan, 1995).

The temporal structure of GRBs is characterized by its large diversity (see Figure 1.4). There is no *typical* temporal structure. GRBs can manifest themselves as single pulses, smooth flares without fine structure, or extremely chaotic and spiky pulses. The variability time scale δT, or the duration of individual spikes, is often much smaller than the total duration of the burst.

Unlike the light curves, the spectra of GRBs manifest in a much more homogeneous fashion. Data from BATSE show that most of the energy of GRBs[4] is released in 100 keV– 1 MeV. Figure 1.5 shows the broad-band spectrum of GRB 990123. Band et al. (1993)

---

[4]Another phenomenon peaked at X-ray energies, namely *X-ray flashes*, has been observed (Heise et al., 2001) and is now identified as related to 'classical' GRBs discussed here.
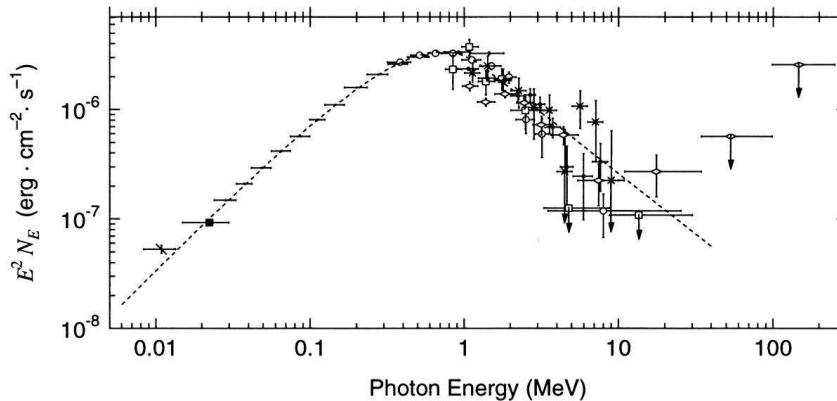
Figure 1.5: The broad-band spectrum of GRB 990123 in the energy range 10 keV – 20 MeV, derived using data from all four instruments on board CGRO (Briggs et al., 1999). The dashed line is a fit using eq. (1.1). The spectrum shows a typical GRB spectrum: it involves a low-energy power law, a single peak at E_{peak} (in this case around 800 keV), and a high-energy power law.

provide a phenomenological fit for most of the observed GRB spectra:

$$
\frac{\mathrm{d}N}{\mathrm{d}\nu} \propto \begin{cases} (h\nu)^{\alpha} \exp(-h\nu/E_0) & \text{for } h\nu < (\alpha - \beta)E_0, \\ ((\alpha - \beta)E_0)^{(\alpha - \beta)} (h\nu)^{\beta} \times \exp(\beta - \alpha) & \text{for } h\nu > (\alpha - \beta)E_0. \end{cases} \tag{1.1}
$$

This functional form is characterized by two power laws joined smoothly at the break energy $(\alpha - \beta)E_0$. The non-thermal spectra of GRBs with power-law tails on both sides have important implications on the radiation mechanisms of GRBs (see Chapter 2). For typical observed values of α and β, the peak of the SED are located at $E_{\text{peak}} = (\alpha + 2)E_0$, which cluster around $\approx$300 keV (Preece et al., 2000). Although observational selection bias may play a role (BATSE sensitivity drops rapidly below $\sim$25 keV and above $\sim$1 MeV, see also Böttcher & Dermer, 2000), this clustering of E_{peak} may be an intrinsic property of GRBs (Preece et al., 2000)[5]. As for *Swift*/BAT, due to its much narrower energy band of 15–150 keV, a simple power law $\mathrm{d}N/\mathrm{d}E \propto E^{-\alpha}$ (with a typical $\alpha \sim 1.6 - 1.8$) is often sufficient to fit the spectra in this range (Sakamoto et al., 2008a).

1.3.2   Burst spectrum between 30 MeV and 100 GeV

Emission above 30 MeV was detected using EGRET from several energetic bursts (Dingus, 1995). In these cases, no evidence of high-energy cut-off was seen. The average spectrum above 30 MeV derived by adding the 53 photons from five EGRET-detected GRBs can be fitted by a power law with a photon index of 1.95 ± 0.25. This is harder than each of the 1–30 MeV spectra of the same bursts, suggesting that spectra of these GRBs extend to higher energies (Dingus, 1995). However, it should be noted that in creating such an 'average' spectrum, a burst with a higher fluence in the EGRET energy band would have a higher weight than a lower fluence burst (as also mentioned in Schaefer et al., 1998,

---

[5]If XRFs, discussed later, form a continuum with GRBs, this clustering may extend to lower energies
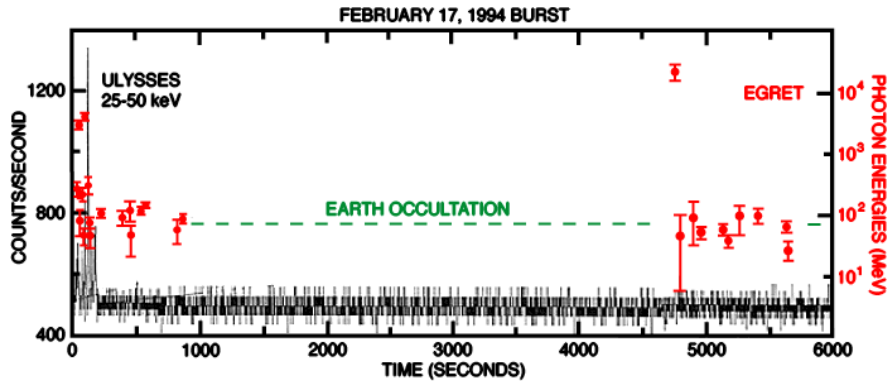
Figure 1.6: GRB 940217 as seen in low-energy γ-ray band with Ulysses and its associated high-energy emission detected with EGRET, including a ∼ 20 GeV photon. The burst position was Earth-occulted for ∼3,700 seconds (Hurley et al., 1994). The high-energy component (in red) has a different temporal evolution than the low-energy component (in black).

for BATSE data). In addition, only bursts with enough photon statistics above 30 MeV are included in this analysis, hence the true 'average' high-energy spectrum (if exist for other GRBs as well) may be softer. Nevertheless, the fact that EGRET detected only the brightest GRBs seen by BATSE suggests that only the "tip of the iceberg" of the high-energy spectra of GRBs has been seen and studied.

The most energetic photon ever detected from a GRB was a ∼20 GeV photon associated with GRB 940217 (Hurley et al., 1994). The burst as seen in low-energy γ-ray band lasted for around ∼200 seconds, but the high-energy emission continued up to ∼1.5 hours after the low-energy emission had faded, including the ∼20 GeV photon. Although the burst position was Earth-occulted for ∼3,700 seconds, emission might continue for the whole 1.5 hours. This is supported by the fact that the count rate and the energy of the high-energy photons were approximately constant before and after the occultation (Figure 1.6). Therefore, a high-energy component seems to be present for this burst, which had a temporal evolution different from the low-energy component.

Another burst which exhibits a distinct high-energy component is GRB 941017. While the low-energy γ-rays (<10 MeV) faded between ∼30s–200s after the BATSE trigger, another spectral component at energies 10–200 MeV remained roughly at the same level during the same period. The high-energy component can be fitted by a power law with a photon index of $\Gamma \sim 1$ and did not show a cut-off, indicating more energy was emitted above 200 MeV (González et al., 2003). Since the frequency-integrated energy is divergent for $\Gamma < 2$, an upper limit of a cut-off is placed at ∼1 TeV to avoid an energy crisis, based on the fact that a burst cannot release more than an energy $\sim 10^{54}$ erg, assuming that the burst is very nearby.

These observations suggest that there exists a high-energy component from some GRBs which evolves differently from the evolution in the soft γ-ray band.

broad-band studies

The intense emission from GRB 840805 allowed for the first detailed study of a GRB spectrum over three decades in energy, from ~ 20 keV to 100 MeV (Share et a., 1986). A recent broad-band study of 15 bright GRBs using γ-ray data taken with two instruments (BATSE/LAD and EGRET/TASC) was carried out by Kaneko et al. (2008), in which GRB 930506 was found to possibly exhibit an extremely high value of $E_{\mathrm{peak}} \sim 167$ MeV.

While the EGRET experiment did not detect MeV–GeV photons from most BATSE GRBs in its FoV (Dingus, 1995), it is possible that some strong bursts (e.g. GRB 930506, GRB 940217, and GRB 941017) may belong to a population of GRBs which exhibit an intense, distinct high-energy component which in principle can extend to the VHE γ-ray band. However, the alternative that all GRBs possess a high energy emission but remain non-detected with the rather low sensitivity of EGRET cannot be ruled out (Dingus, 1995). The two experiments on board Fermi, GBM and LAT, are currently providing us the first opportunity to study GRBs with an even boarder coverage in energies (from $\sim$10 keV to $\sim$300 GeV) — more than six orders of magnitudes)[6].

1.3.3 Searches of counterparts of Gamma-ray bursts above 100 GeV

There are two techniques used to search for GRB counterparts in the VHE γ-ray band ($\gtrsim$100 GeV). The first is to monitor a large part of the sky continuously. This technique is used for EAS because of their large coverage of the sky and their high duty cycle. Several searches are reported (Amenomori et al., 1996; Cabrera et al., 1999; Poirier et al., 2003; Alvarez et al., 2005; Atkins et al., 2005; Abdo et al., 2007; di Sciascio & di Girolamo, 2007). There may be indications of excess photon events in a few cases (Amenomori et al., 1996; Atkins et al., 2000; Poirier et al., 2003), but none of them is conclusive. The HEGRA collaboration reported observations of four satellite-detected GRBs and found an evidence of excess (related to GRB 920925C) in their data taken with the AIROBICC array, at a 2.7σ significance level (Padilla et al., 1998). The Milagrito burst (GRB 970417A, see Figure 1.7) may represent the best evidence for a detection, which shows a *tentative* evidence of an enhancement of events with a (post-trial) $\sim 3\sigma$ significance (a probability of 1.5×10^{-3} of being statistical fluctuation of the background Atkins et al., 2000). If the excess events seen by Milagrito were actually associated with GRB 970417A, the photon energy must be at least 650 GeV and the VHE γ-ray energy fluence must be at least an order of magnitude higher than the 50–300 keV energy fluence (Atkins et al., 2003). However, the null detection from a lot more GRBs with the more sensitive MILAGRO detector (with a much lower background level than its forerunner Atkins et al., 2005) does not confirm the above case and this might indicate that the *tentative detection* was actually a statistical fluctuation of the background.

The second technique is to slew quickly to the GRB position provided by a burst alert from satellites. This technique is used for IACTs, including the H.E.S.S. telescopes, because of their relatively smaller FoV of a few degrees. Using the single 10-m Whipple

---

[6]GRB 080825C is the first GRB reported to be detected in both instruments (Bouvier et al., 2008; van der Horst & Connaughton, 2008).
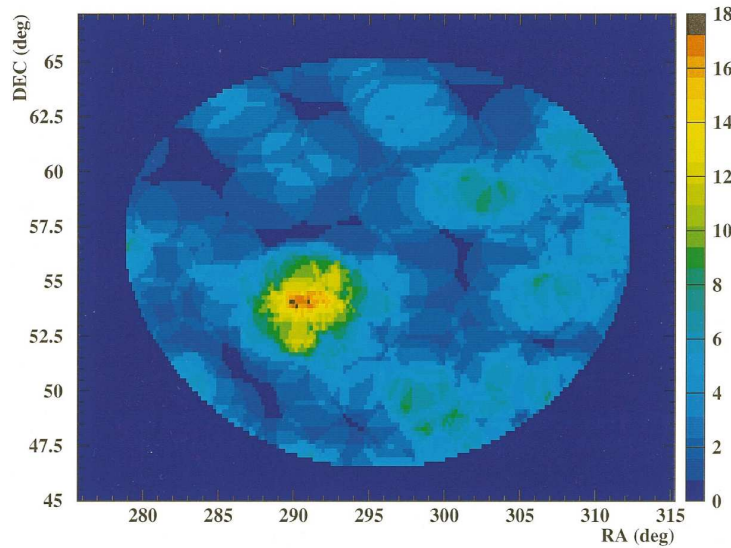
Figure 1.7: The sky excess map from Milagrito observations in the neighborhood of the BATSE position of GRB 970417A during the burst. The probability of the enhancement being a statistical fluctuation of the background is 1.5×10^{-3} (Atkins et al., 2000).

telescope, Connaughton et al. (1997) and Horan et al. (2007) reported observations of 9 BATSE bursts, 5 HETE-II bursts, and 2 INTEGRAL bursts. The delay time is typically minutes to hours with the shortest one being 2 minutes. Götting & Horns (2001) also carried out follow-up observations of GRBs, using the stereoscopic HEGRA Cherenkov telescope system. The solar array, STACEE, was also used to perform GRB follow-up observations, albeit with a lower sensitivity than IACTs (Jarvis et al., 2008). One of the fastest response has been made by the MAGIC telescope, which was able to slew to the position of GRB 050713A, 40 s after the GRB onset, while the *prompt* keV emission was still active. A total of 37 minutes of observations were made and no evidence of emission above 175 GeV was obtained (Albert et al., 2006a). The rapid follow-up observations using this telescope of 8 other GRBs show no evidence of VHE γ-ray emission from these GRBs during the *prompt* or the *early afterglow* phase (Albert et al., 2007b).

These two techniques have their own advantages and limitations, and therefore are complement to each other. While the full-time monitoring of EAS has the privileges of no time delay and a high duty cycle (therefore suitable to search for strong TeV emission during the prompt phase), Cherenkov detectors have lower energy threshold and much higher efficiency of background rejection which make them more suitable to look for VHE signal with an unprecedent sensitivity during the afterglow phase. Several VHE instruments which have been active in GRB observations are listed in Table 1.2.

Apart from the above-mentioned searches of VHE γ-ray counterpart of satellite-detected GRBs, efforts have been made to search for VHE burst-like events, regardless of whether these events are associated with satellite-detected GRBs. These searches are motivated by the following: (1) VHE γ-ray emission associated to a GRB can be detected independently of whether the GRB is registered at all by a satellite (this is especially important during those years when no all-sky monitor of GRBs like BATSE is operating); (2) VHE

Table 1.2: Several GRB observation instruments operating in the VHE gamma-ray regime. EAS = extensive air shower array; IACT = imaging atmospheric Cherenkov telescopes

Instrument	Type	Site	Lat. (°)	Long. (°)	Approx. Slew rate	Evidence of VHE γ-rays from GRBs?
ARGO-YBJ	EAS	Tibet, China	30.2N	90.4E	–	No[a]
GRAND	EAS	Illinois, US	41.7N	86.2W	–	Yes[b]
H.E.S.S.	IACT	Namibia	23.3S	16.5E	$2°\,\mathrm{s}^{-1}$	No[c]
MAGIC	IACT	La Palma, Spain	28.8N	17.9W	$5°\,\mathrm{s}^{-1}$	No[d]
Milagro	EAS	New Mexico, US	35.9N	106.7W	–	No[e]
Sierra la Negra	EAS	Puebla, Mexico	19.0N	97.3W	–	No[f]
STACEE	Solar array	New Mexico, US	35.0N	106.5W	$1°\,\mathrm{s}^{-1}$	No[g]
Tibet-III ASγ	EAS	Tibet, China	30.2N	90.4E	–	No[h]
VERITAS	IACT	Arizona, US	31.7N	111.0W	$1°\,\mathrm{s}^{-1}$	No[i]
Whipple-10m	IACT	Arizona, US	31.5N	111W	$1°\,\mathrm{s}^{-1}$	No[j]

[a]di Sciascio & di Girolamo (2007)

[b]A very tentative (pre-trial) 2.7σ evidence from GRB 971110 (Poirier et al., 2003).

[c]this thesis

[d]Albert et al. (2007b)

[e]Atkins et al. (2005) and Abdo et al. (2007), but see Atkins et al. (2000) for a tentative (post-trial) $\sim 3\sigma$ evidence for GRB 970417A using data from its forerunner — Milagrito.

[f]Alvarez et al. (2005)

[g]Jarvis et al. (2008)

[h]Zhou (2003), but see Amenomori et al. (1996) for a $\sim 6\sigma$ evidence from a stacking analysis derived from the data collected by its forerunner.

[i]Horan et al. (2008)

[j]Connaughton et al. (1997) and Horan et al. (2007)

bursts (which do not have low-energy γ-ray counterpart) are predicted by some models like Hawking radiation. Such searches were performed by Padilla et al. (1998) using the HEGRA AIROBICC array, Connaughton et al. (1998) using the Whipple telescope, and Atkins et al. (2004) using the MILAGRO air shower array. They looked into a large amount of data taken over a certain period of time and search for any spatial and/or temporal clustering of events. None of these searches yielded a significant detection.

As we have seen, there has been no significant detection of any electromagnetic radiation with photon energy above 20 GeV. One may at this point draw a tentative conclusion that there is no strong VHE emission from GRBs, neither during the prompt or the afterglow phases. However, this only applies to the VHE signal as observed *on the Earth*, but not the VHE emission as produced *in the source*. As most GRBs are located at cosmological distances, VHE γ-rays have to travel a long distance to reach us. Therefore, any VHE emission is attenuated by the extragalactic background light before reaching us. This effect is discussed in the next section.

1.4 Extragalactic background light and pair production

Any energetic photon with an energy E_{γ_1} has a certain probability to be attenuated by another photon, E_{γ_2}, creating a pair of positron and electron, if

$$E_{\gamma_1} E_{\gamma_2}(1 - \cos\theta) > m_e^2 c^4 \tag{1.2}$$

where θ is the angle between the arrival directions of the photons and $m_e \approx 511$ keV is the rest mass of an electron. This process is known as *photon-photon pair production*. For example, when surrounded by isotropic diffuse soft-radiation, 1 TeV photon will be most effectively attenuated by a low-energy photon with energy of ~ 0.9 eV (or $\lambda \sim 1.33\,\mu$m). Therefore, if emitted at cosmological distances, VHE γ-ray photons are absorbed by the optical light before they arrive the Earth. For a photon traveling through a cosmological distance z, the opacity of the pair production process is given by

$$\tau_{\gamma\gamma}(E_\gamma, z) = \frac{3}{8}\sigma_T \frac{c}{H_0} \int_0^z \sqrt{1+z}\,\mathrm{d}z \int_{\frac{m_e^2 c^4}{E_\gamma(1+z)^2}}^{\infty} \mathrm{d}E' \frac{\mathrm{d}n(E')}{\mathrm{d}E'} \times F\left[\frac{m_e^2 c^4}{E_\gamma E'(1+z)^2}\right], \tag{1.3}$$

where σ_T denotes Thomson cross section, H_0 the Hubble constant, $\mathrm{d}n(E')/\mathrm{d}E'$ the differential number density of optical photons, and F a function depending on $\cos\theta$, E_γ, and E', the energy of the optical photon. The observed VHE flux, $F_{\mathrm{obs}}(E)$ is then given by

$$F_{\mathrm{obs}}(E) = F_{\mathrm{int}}(E) \times e^{-\tau_{\gamma\gamma}(E)}. \tag{1.4}$$

where $F_{\mathrm{int}}(E)$ is the observed flux of the source in the case where EBL effect is neglected. The extragalactic background light (EBL) in the optical band is mostly contributed by starlight. Several models of the spectral energy distribution of EBL were proposed by, e.g. Kneiske et al. (2004), Primack et al. (2005), and Stecker et al. (2006). While all these models predict comparable level for EBL at low redshifts (e.g. $z < 0.2$) and therefore the opacity, there are discrepancies between the models for higher redshifts.

1.5   An outline of the thesis

During past few years (2004–2008) we have seen two important breakthroughs in high-energy astrophysics. Firstly, VHE astronomy has been a fast-growing branch in astronomy, thanks to the maturity of the IACT technique. Not only has the number of known VHE sources increased to more than 70, the types of known galactic and extragalactic 'cosmic-accelerators' have also become more diverse. The known VHE horizon has reached $z = 0.2$, and possibly $z \approx 0.5$. It is fair to say that the horizon will keep increasing due to the lower energy threshold ($\lesssim 100$ GeV) achieved by the Imaging Cherenkov technique. The recorded most energetic photon from GRBs carried an energy ~ 20 GeV, only a factor of ~ 5 below the energy threshold of an IACT system like H.E.S.S.

Secondly, the *Swift* satellite has helped to reveal the origins of GRBs, especially of short/hard GRBs. It has opened new opportunities to study all phases of GRBs in every waveband, because of its sophisticated on-board trigger of GRBs and its quick distribution of well-localized GRB locations to other observing sites around the globe. The H.E.S.S. GRB observing programm has taken this advantage to study GRBs at time scales of minutes to hours after the GRBs.

It is during these exciting moments that the major work presented in this thesis was carried out.

The structure of this thesis is outlined as follows. First of all, a review of physical mechanisms responsible for generating GRBs and the afterglows, as well as for emitting VHE γ-rays, is presented in Chapter 2. In Chapter 3, the H.E.S.S. experiment and the GRB observing program are described. A study of data quality is also given. Chapter 4 presents the GRB observations taken with H.E.S.S. during the years 2003–2007 and results of these observations. The work represents the largest sample of GRB afterglow observations made by an IACT array and result in the most stringent upper limits obtained in the VHE band. To gain insights from the observational data, a specific, though well-established, model, was applied to several nearby GRBs. Model predictions are compared with VHE data, including those obtained with H.E.S.S. These results are presented in Chapter 5. On June 2, 2006, a GRB position fell serendipitously at the edge of the FoV of the H.E.S.S. cameras when the burst occurred. The analysis and results of these observations are given in Chapter 6. Towards the future, a proposal of a planned instrument CTA on GRB science is given in Chapter 7, which is followed by some concluding remarks in Chapter 8.

The bulk of materials presented in Chapters 4, 5, and 6 are at various stages towards submission or publication in a refereed journal. I am the corresponding author of Chapter 4 and Chapter 6, and one of the two corresponding authors of Chapter 5.

Chapter 2

Radiation mechanisms for γ-ray bursts

In this chapter, radiation mechanisms related to the generation of the prompt γ-ray emission as well as afterglow emission at lower energies are reviewed. Then the predicted VHE γ-ray emission in the prompt and afterglow phases based on different radiation mechanism scenarios is presented.

2.1 Physical conditions

Consider a relativistically moving material from the progenitor (the inner engine) at a cosmological distance. The material has a bulk Lorentz factor Γ_b relative to the inner engine. We can identify three reference frames: the rest frame of the engine, the comoving frame of the emitting material, and the observer's frame. The quantities in the comoving frame (which is denoted by a prime "$'$" hereafter) are shifted by a factor Γ_b as viewed in the rest frame of the engine. Quantities in the observer's frame is related to the engine's frame by the cosmological redshift factor $(1 + z)$. For simplicity, all physical quantities in this chapter (unless otherwise specified) will be shown in the engine's frame or the comoving frame.

We then assume that the particles responsible for the prompt keV emission are electrons. Generally, it takes longer time for protons to be accelerated, which makes them more difficult to accommodate the rapid variability observed in GRBs. The contribution by protons, which may be important in the GeV–TeV regime, will be discussed in Section 2.7.

It is commonly assumed that the energy distribution of the accelerated electrons (i.e. the *injected* population) can be described by a power law:

$$\frac{dN'_e}{d\gamma'_e} \propto \gamma_e'^{-p} \tag{2.1}$$

where $\gamma'_{\min} < \gamma'_e < \gamma'_{\max}$ and $p > 2$ in most acceleration scenarios. Therefore, the bulk of the electrons will have a Lorentz factor close to $\gamma'_{\min}$. The average electron energy is

$$\overline{\gamma'_e} m_e c^2 = \frac{p-1}{p-2} \gamma'_{\min} m_e c^2 \tag{2.2}$$

where m_e is the electron mass and c is the speed of light. The fraction of energy in the emitting material distributed to electrons is

$$\epsilon_e \equiv \frac{U'_e}{U'} = \frac{N'_e \overline{\gamma'_e} m_e c^2}{U'} \qquad (2.3)$$

where U' and U'_e is the total energy density and the electron energy density, respectively. Then $\gamma'_{\min}$ can be written as[1]

$$\gamma'_{\min} = \frac{p-2}{p-1} \frac{\epsilon_e U'}{N'_e m_e c^2}. \qquad (2.4)$$

On the other hand, $\gamma'_{\max}$ is generally very high (see eq. 2.18)and its exact value does not affect the observed spectrum for $p > 2$.

For a uniform magnetic field of strength B' in the emitting region, the magnetic energy density is $U'_B = B'^2/(8\pi)$. The fraction of energy in the magnetic field is

$$\epsilon_B \equiv \frac{U'_B}{U'} = \frac{B'^2}{8\pi U'}. \qquad (2.5)$$

The accelerating time scale of an electron may be written as

$$t'_{\text{acc}} = \gamma'_e m_e c / (\eta_{\text{acc}} q B') \qquad (2.6)$$

where $\eta_{\text{acc}} \leq 1$ is the acceleration efficiency and q the electron charge (Cheng & Wei, 1996).

In the case of negligible radiation loss (i.e. the radiation efficiency, $\eta_{\text{rad}} \ll 1$), the emitting region still cools by adiabatic expansion. The dynamical time scale is related to the distance, R, of the emitting region from the inner engine by $t_{\text{dyn}} \sim R/(c\Gamma_b^2)$. In the comoving frame, it is

$$t'_{\text{dyn}} \sim \frac{R}{c\,\Gamma_b}. \qquad (2.7)$$

2.2 Synchrotron emission

Synchrotron emission is resulted when an electron moves in a magnetic field. The spectrum radiated by a single electron is shown in Figure 2.1, which shows a relatively flat spectrum of $\nu^{1/3}$ below $\nu_{\text{syn}} \equiv \omega_{\text{syn}}/(2\pi)$ and above which an exponential cut-off. The synchrotron power by a single electron is given by (Rybicki & Lightman, 1979)

$$P'_{\text{syn}}(\gamma'_e) = \frac{4}{3}\sigma_T c \gamma'^2_e U'_B \qquad (2.8)$$

where σ_T is the Thomson's cross section. The cooling time of an electron is then

$$t'_{\text{syn}}(\gamma'_e) = \frac{\gamma'_e m_e c^2}{P'_{\text{syn}}} = \frac{3m_e c}{4\sigma_T U'_B \gamma'_e}. \qquad (2.9)$$

---

[1]In the context of the widely considered external shock model, $U' \approx \Gamma_b N'_p m_p c^2$. Hence, $\gamma'_{\min} \approx \Gamma_b (m_p/m_e)(p-2)\epsilon_e/(p-1)$ since $N'_p = N'_e$.
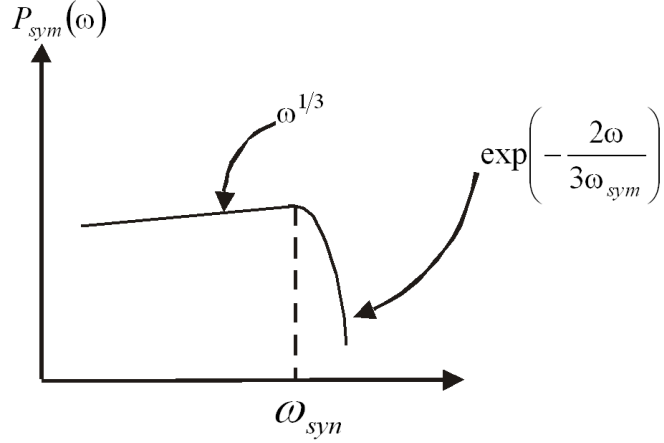
Figure 2.1: Synchrotron spectrum from a single electron (Cheng, 2005)

The characteristic frequency $\nu_{\rm m}$ is related to the synchrotron frequency of the bulk of the electrons at $\gamma'_{\rm min}$:

$$\nu_{\rm m} = \frac{qB'}{2\pi} \frac{\gamma'^2_{\rm min}\Gamma_{\rm b}}{m_e c}. \tag{2.10}$$

The Lorentz factor of the electrons which cool in the dynamical time scale is

$$\gamma'_c = \frac{3m_e c}{4\sigma_{\rm T} U'_B t'_{\rm dyn}} = \frac{3m_e c\Gamma_{\rm b}}{4\sigma_{\rm T} U'_B R} \tag{2.11}$$

whose synchrotron frequency is called the cooling frequency

$$\nu_{\rm c} = \frac{qB'}{2\pi} \frac{\gamma'^2_{\rm c}\Gamma_{\rm b}}{m_e c}. \tag{2.12}$$

That is, electrons with energy above γ'_c radiate a significant fraction of their energy in the dynamical time scale. In the case of no significant continuous acceleration, i.e. no 'new' accelerated electron is injected in the emitting region in $t'_{\rm dyn}$ (e.g. in the afterglow phase with simple power-law temporal decay), the electron distribution as shown in eq. (2.1) will be modified above γ'_c (Sari & Esin, 2001):

$$\frac{dN'_{\rm e}}{d\gamma'_e} \propto \begin{cases} \gamma'^{-p}_e & \text{for} \quad \gamma'_{\rm min} < \gamma'_e < \gamma'_c \\ \gamma'^{-(p+1)}_e & \text{for} \quad \gamma'_e > \gamma'_c \end{cases} \tag{2.13}$$

This is valid only if $\gamma'_{\rm c} > \gamma'_{\rm min}$. This is the case of *slow cooling* as most of the electrons do not cool in $t'_{\rm dyn}$. The observed spectrum is given by

$$F_\nu \propto F_{\nu,\max} \begin{cases} (\nu/\nu_m)^{1/3} & \text{for} \quad \nu_m > \nu \\ (\nu/\nu_m)^{-(p-1)/2} & \text{for} \quad \nu_c > \nu > \nu_m \\ (\nu_c/\nu_m)^{-(p-1)/2}(\nu/\nu_c)^{-p/2} & \text{for} \quad \nu > \nu_c \end{cases} \tag{2.14}$$

Here, the $\nu^{-(p-1)/2}$ part is the standard result for the synchrotron spectrum by an electron distribution of a simple power law (Rybicki & Lightman, 1979). Most energetic
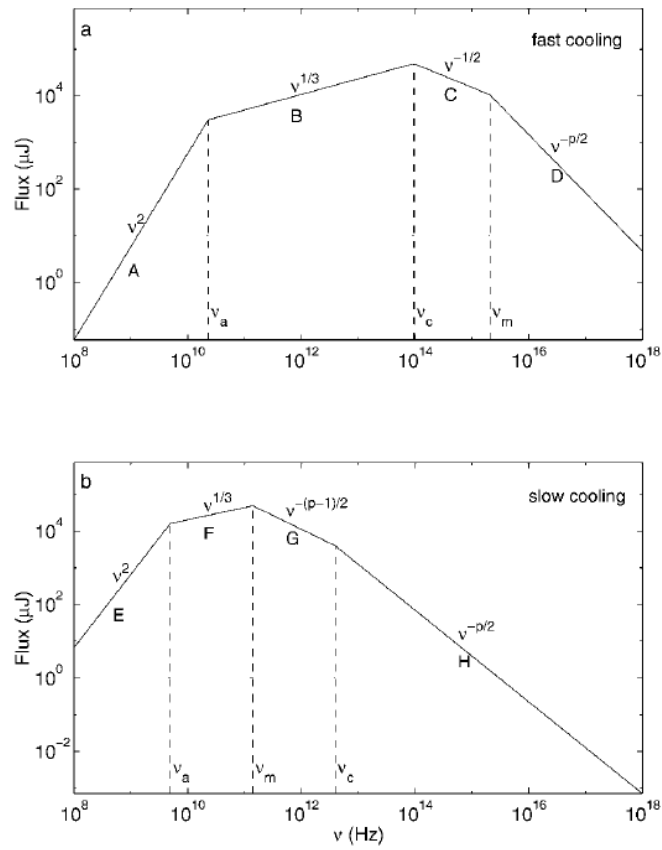
Figure 2.2: Synchrotron spectrum with a power-law electron distribution. Both the *fast cooling* case and the *slow cooling* case are shown. The letters indicate different segments of the spectrum (adapted from Sari et al., 1998).

electrons (i.e. those above γ'_c) cool rapidly, giving rise to $\nu^{-p/2}$. The $\nu^{1/3}$ part (below ν_m) is the spectral form of synchrotron emission of individual electrons with energy γ'_{min} (see Figure 2.1). Below a certain frequency ν_a, the synchrotron self-absorption results in $F_\nu \propto \nu^2$ (Piran, 1999). The maximal specific flux, $F_{\nu,max}$, as observed on Earth can be estimated, in the shock model, as (Fan & Piran, 2008)

$$F_{\nu,max} \approx \frac{(1+z)q^3 N_{e,tot}\Gamma_b B'}{4\pi m_e c^2 d_L^2} \tag{2.15}$$

where $N_{e,tot}$ is the total number of electrons and d_L is the luminosity distance of the GRB.

If $\gamma'_c < \gamma'_{min}$, i.e. the *fast cooling* case, all electrons can cool in t'_{dyn}. In this case, the distribution is described by (Sari & Esin, 2001):

$$\frac{dN'_e}{d\gamma'_e} \propto \begin{cases} \gamma_e'^{-2} & \text{for} \quad \gamma'_{min} > \gamma'_e > \gamma'_c \\ \gamma_e'^{-(p+1)} & \text{for} \quad \gamma'_e > \gamma'_{min}. \end{cases} \tag{2.16}$$

This is probably the case for prompt emission phase (if the prompt emission is indeed due to synchrotron emission; we will address this possibility in Section 2.5.1), since high radiation efficiency and short radiation time scales are needed to explain the observed extremely fast variability. The observed spectrum is given by

$$F_\nu \propto F_{\nu,max} \begin{cases} (\nu/\nu_c)^{1/3} & \text{for} \quad \nu_c > \nu \\ (\nu/\nu_c)^{-1/2} & \text{for} \quad \nu_m > \nu > \nu_c \\ (\nu_m/\nu_c)^{-1/2}(\nu/\nu_m)^{-p/2} & \text{for} \quad \nu > \nu_m. \end{cases} \tag{2.17}$$

Figure 2.2 depicts the synchrotron spectrum for both the *fast cooling* case and the *slow cooling* case. Note that the $\nu^{1/3}$ part (segments B and F in Figure 2.2) is apparent in both cases.

The maximum Lorentz factor of electrons γ'_{max} can be estimated by equating the synchrotron cooling time scale (eq. 2.9) with the acceleration time scale (c.f. eq. 2.6)

$$\gamma'_{max} = \sqrt{\frac{6\pi\eta_{acc}q}{\sigma_T B'}} \approx 3 \times 10^9 \eta_{acc}^{1/2} B'^{1/2} \tag{2.18}$$

where B' is measured in gauss. The maximum achievable synchrotron frequency is therefore

$$\nu_{max} = \frac{qB'}{2\pi}\frac{\gamma_{max}'^2 \Gamma_b}{m_e c} = \frac{3q^2\eta_{acc}\Gamma_b}{m_e \sigma_T c} \tag{2.19}$$

which is independent of B'. Assuming $\Gamma_b \approx 100$ and $\eta_{acc} \approx 1$, one obtains $\nu_{max} \approx 4 \times 10^{24}$ Hz, which is very similar to the most energetic $\sim$20 GeV photon ever detected from GRBs. If photons with higher energy is detected, other radiation mechanisms must be considered.

2.3 Inverse Compton emission

Inverse Compton (IC) emission arises when an energetic electron scattering off a lower energy photon, transferring part of its kinetic energy to the photon, and thereby 'boosting'

the photon to a higher energy. Let us consider that an electron with γ_e is emerged in an isotropic photon field with radiation energy density $U'_{\rm rad}$. The power given out by the electron is (Rybicki & Lightman, 1979)

$$P'_{\rm ic}(\gamma'_e) = \frac{4}{3}\sigma_{\rm T} c \gamma'^2_e U'_{\rm rad}. \tag{2.20}$$

This is valid[2] only in the *Thomson* regime, in which the energy of the photon in the field, $h\nu'_{\rm seed}$, before up-scattering (i.e. the *seed* photon) is much lower than electron's rest mass in the electron's rest frame (i.e. $\gamma'_e h\nu'_{\rm seed} \ll m_e c^2$). The photon after up-scattering will attain an energy

$$h\nu'_{\rm ic} \sim \gamma'^2_e h\nu'_{\rm seed} \tag{2.21}$$

where h is the Planck's constant.

The cooling time of the electron due to IC emission is

$$t'_{\rm ic}(\gamma'_e) = \frac{\gamma'_e m_e c^2}{P'_{\rm ic}} = \frac{3m_e c}{4\sigma_{\rm T} U'_{\rm rad} \gamma'_e}. \tag{2.22}$$

For an *arbitrary* photon field, a power-law electron distribution (c.f. eq. 2.1) will give rise to a spectrum $F_\nu \sim \nu^{-(p-1)/2}$, the same as the synchrotron case (Rybicki & Lightman, 1979).

In the *Klein-Nishina* regime, the energy of the seed photon is comparable to or larger than electron's rest mass in the rest frame of the electron (i.e. $\gamma'_e h\nu'_{\rm seed} \gtrsim m_e c^2$). The cross section of the IC scattering is reduced to (Rybicki & Lightman, 1979)

$$\sigma_{\rm KN} \approx \frac{3}{8}\sigma_{\rm T} \frac{m_e c^2}{h\nu'_{\rm seed}} \left[\ln\left(\frac{2h\nu'_{\rm seed}}{m_e c^2}\right) + \frac{1}{2} \right] \tag{2.23}$$

in the extreme relativistic case, i.e. $\gamma'_e h\nu'_{\rm seed} \gg m_e c^2$. The probability of an electron up-scattering the seed photons is largely reduced. The characteristic energy of the scattered photon becomes (Blumenthal & Gould, 1970)

$$h\nu'_{\rm ic,KN} \sim \gamma'_e m_e c^2. \tag{2.24}$$

Thus, the energy gain of the photon per scattering is suppressed, as compared to eq. (2.21).

2.3.1 Synchrotron self-Compton emission

The synchrotron photons emitted by a population of relativistic electrons can be up-scattered to higher energies by the same electron population. This is called synchrotron self-Compton (SSC) emission, in which the synchrotron photons act as the seed photons for IC scattering. Under certain conditions, the scattered photons can again be up-scattered to even high energies, resulting in higher-order scattering. We consider the situation when only the first-order scattering is important.

---

[2]A factor of $1 - (63/10)\left(\gamma'_e \overline{(h\nu'_{\rm rad})^2}\right) / \left(m_e c^2 \overline{h\nu'_{\rm rad}}\right)$ is to be added when the energy transfer in the electron's rest frame is not neglected, in which $\overline{(h\nu'_{\rm rad})^2}$ and $\overline{h\nu'_{\rm rad}}$ are the mean squared photon energy and the mean photon energy of the photon field (Blumenthal & Gould, 1970).

The importance of IC scattering is described by the Compton parameter, Y, which can be written as

$$Y \equiv \frac{P'_{\text{ic}}}{P'_{\text{syn}}} = \frac{U'_{\text{rad}}}{U'_B} = \frac{U'_{\text{syn}}}{U'_B} \tag{2.25}$$

in which eqs. (2.8) and (2.20) are used. Assuming that the electrons are accelerated in relativistic shock, following Sari & Esin (2001) we have $U'_{\text{syn}} = \eta_{\text{rad}} U'_e/(1+Y)$, therefore

$$Y = \frac{\eta_{\text{rad}} U'_e/(1+Y)}{U'_B} = \frac{\eta_{\text{rad}} \epsilon'_e}{\epsilon'_B(1+Y)} \tag{2.26}$$

The radiation efficiency, $0 \le \eta_{\text{rad}} \le 1$, includes both synchrotron and IC emission. Fast-cooling and slow-slowing corresponds to the case when $\eta_{\text{rad}} \approx 1$ and $\eta_{\text{rad}} \ll 1$, respectively. Solving eq. (2.26) for Y gives

$$Y = \begin{cases} \eta_{\text{rad}}(\epsilon'_e/\epsilon'_B) & \text{for} \quad \eta_{\text{rad}}(\epsilon'_e/\epsilon'_B) \ll 1 \\ [\eta_{\text{rad}}(\epsilon'_e/\epsilon'_B)]^{1/2} & \text{for} \quad \eta_{\text{rad}}(\epsilon'_e/\epsilon'_B) \gg 1. \end{cases} \tag{2.27}$$

Therefore, whether $\eta_{\text{rad}}(\epsilon'_e/\epsilon'_B) > 1$ or $\eta_{\text{rad}}(\epsilon'_e/\epsilon'_B) < 1$ will determine the relative dominance of the synchrotron and the IC emission. This expression is true in the Thomson regime. In the extreme *Klein-Nishina* regime (i.e. $\gamma'_e h\nu'_{\text{seed}} \gg m_e c^2$), the Compton parameter Y is divided by a factor of $(\gamma'_e h\nu'_{\text{seed}}/m_e c^2)^2$ (Fan & Piran, 2008).

Consider the case where $Y \gtrsim 1$, in which the IC component is important. In the Thomson regime, the IC spectrum is qualitatively similar to the synchrotron spectrum in many ways. Using eq. (2.21), it can be seen that

$$\nu'_{\text{ic,a}} \sim \gamma'^2_{\text{min}} \nu'_a, \quad \nu'_{\text{ic,m}} \sim \gamma'^2_{\text{min}} \nu'_m, \quad \text{and} \quad \nu'_{\text{ic,c}} \sim \gamma'^2_c \nu'_c. \tag{2.28}$$

Since both synchrotron and IC cooling are at work, the electrons which cool in t'_{dyn} now have the following Lorentz factor:

$$\gamma'_c = \frac{3m_e c}{4\sigma_T(U'_B + U'_{\text{syn}})t'_{\text{dyn}}} = \frac{3m_e c \Gamma_b}{4\sigma_T(1+Y)U'_B R} \tag{2.29}$$

since $1/t'_{\text{dyn}} = 1/t'_{\text{syn}} + 1/t'_{\text{ic}}$ for these electrons. From eq. (2.12), it follows that the corresponding synchrotron cooling frequency, ν_c, is reduced by a factor of $(1+Y)^2$ with respect to the case where IC emission is negligible. The characteristic synchrotron frequency, ν_m, which depends on the magnetic field B' and the injected minimum Lorentz factor γ'_{min} only, is not affected.

Figure 2.3 depicts the calculated spectrum including both synchrotron and IC components where $Y > 1$. The broken power-law approximated IC spectrum (shown in Figure 2.3 as dashed lines) can be written as (Fan & Piran, 2008)

$$F_{\text{ic},\nu} \propto \begin{cases} \nu^{1/3} & \text{for} \quad \nu < \nu_{\text{ic,m}} \\ \nu^{-(p-1)/2} & \text{for} \quad \nu_{\text{ic,c}} > \nu > \nu_{\text{ic,m}} \\ \nu^{-p/2} & \text{for} \quad \nu > \nu_{\text{ic,c}} \end{cases} \tag{2.30}$$
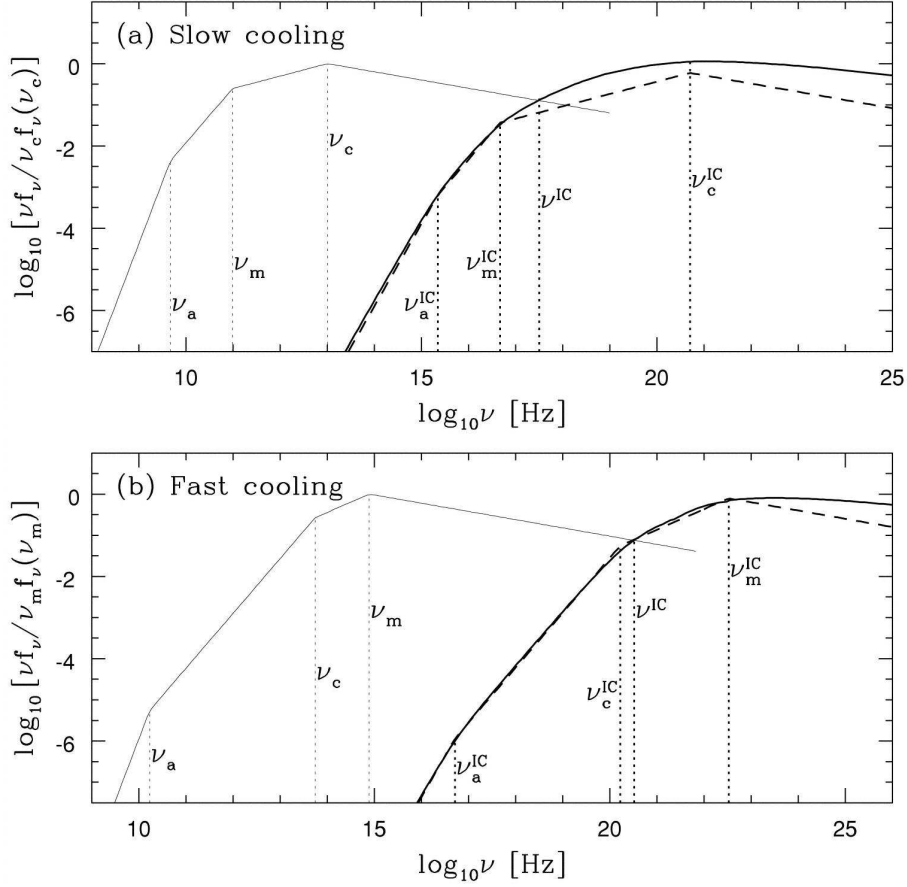
Figure 2.3: The synchrotron (thin solid line) and IC components (thick solid line) in a GRB afterglow spectrum. The broken power-law approximation to the IC spectrum is shown as a dashed line (Sari & Esin, 2001).

in the case of slow-cooling ($\nu_{\mathrm{ic,m}} < \nu_{\mathrm{ic,c}}$), or

$$F_{\mathrm{ic},\nu} \propto \begin{cases} \nu^{1/3} & \text{for} \quad \nu < \nu_{\mathrm{ic,c}} \\ \nu^{-1/2} & \text{for} \quad \nu_{\mathrm{ic,m}} > \nu > \nu_{\mathrm{ic,c}} \\ \nu^{-p/2} & \text{for} \quad \nu > \nu_{\mathrm{ic,m}} \end{cases} \tag{2.31}$$

in the case of fast-cooling ($\nu_{\mathrm{ic,m}} > \nu_{\mathrm{ic,c}}$). Note that the $\nu^{-(p-1)/2}/\nu^{-1/2}$ part (for slow/fast-cooling) of the IC component spans a frequency band double that of the synchrotron component (in logarithmic units), since $\nu_{\mathrm{ic,m}}/\nu_{\mathrm{ic,c}} \sim (\nu_{\mathrm{m}}/\nu_{\mathrm{c}})^2$. When contributions from electrons of different energies are included, logarithmic terms are added on top of this broken power-law approximated IC spectrum, shown as the thick solid line in Figure 2.3.

Not shown in Figure 2.3, the energy, $h\nu_{\mathrm{ic,KN}}$, above which the IC scattering is in the *Klein-Nishina* regime can be estimated by requiring the seed photon frequency of the last up-scattering to be $\max\{\nu_{\mathrm{m}}, \nu_{\mathrm{c}}\}$ (Guetta & Granot, 2003; Fan & Piran, 2008). This results in

$$h\nu_{\mathrm{ic,KN}} \sim \frac{(m_e c^2)^2 \, \Gamma_{\mathrm{b}}}{h \times \max\{\nu_{\mathrm{m}}, \nu_{\mathrm{c}}\}}. \tag{2.32}$$

Above this energy the IC emission is less efficient as a result of the reduced IC cross-section, and a spectral break is expected. For example, in the case of slow cooling, which happened in the afterglow phase in the shock model, we have $\max\{\nu_{\mathrm{m}}, \nu_{\mathrm{c}}\} \approx 10^{13}$Hz, and hence $\nu_{\mathrm{ic,KN}} \sim 10^{26}$Hz (or $h\nu_{\mathrm{ic,KN}} \sim 50$ GeV), assuming $\Gamma_{\mathrm{b}} \sim 10$. In the *Klein-Nishina* regime (i.e. $\nu_{\mathrm{ic,KN}} < \nu < \nu_{\mathrm{ic,KN,max}}$ where $\nu_{\mathrm{ic,KN,max}}$ is given below in eq. 2.34), the spectrum can be approximated by (Guetta & Granot, 2003)

$$F_{\mathrm{ic,KN},\nu} \propto \begin{cases} \nu^{-(p+1)/2} & \text{for} \quad \nu_{\mathrm{ic,m}} < \nu_{\mathrm{ic,c}} \\ \nu^{(1-2p)/2} & \text{for} \quad \nu_{\mathrm{ic,m}} > \nu_{\mathrm{ic,c}} \end{cases} \tag{2.33}$$

If $p = 2$, we get $F_{\mathrm{ic,KN},\nu} \propto \nu^{-3/2}$ in both cases. The maximum achievable SSC frequency, $\nu_{\mathrm{ic,KN,max}} = \nu_{\mathrm{ic,KN}}(\gamma'_{\mathrm{max}})$, is given by (c.f. eq. 2.24)

$$\begin{aligned} \nu_{\mathrm{ic,KN,max}} &\sim \frac{\Gamma_{\mathrm{b}}\gamma'_{\mathrm{max}} m_e c^2}{h} \\ &\sim 3 \times 10^{30}(\Gamma_{\mathrm{b}}/10)\eta_{\mathrm{acc}}^{1/2} B'^{1/2}\,\mathrm{Hz} \end{aligned} \tag{2.34}$$

where γ'_{max} is given by eq. (2.18) and B' is measured in gauss. However, as we shall see in Section 2.4, photons of such high energy cannot escape from the emitting site because of the photon-photon pair attenuation.

2.3.2 Other inverse Compton processes

Two other inverse Compton processes which have been applied to GRBs are briefly mentioned here.

External IC emission is generated when the seed photons for IC scattering are originated outside the region of the respective relativistic electrons. The seed photon field is in many cases not isotropic to the region, and therefore the incident angle of the seed photon in the rest frame of the electrons is *on average* highly beamed. The process has been treated in, e.g. Aharonian & Atoyan (1981). External IC emission from different emitting regions from GRBs is considered, e.g., by Wang et al. (2001) and Galli & Piro (2007) in different contexts.

Bulk IC emission is generated when the whole bulk of the material with Γ_{bulk} up-scatter incoming seed photons. The scattered photons will roughly have a frequency of $\nu \sim \Gamma_{\mathrm{bulk}}^2 \nu_{\mathrm{seed}}$. This process has been considered to explain the prompt GRB emission in the cannonball model by Dar & De Rújula (2004) and the X-ray flare phenomenon observed during the afterglow phase by Panaitescu (2008).

2.4 Pair production

We refer to the internal pair production of electron/positron pairs in the emitting region when two energetic photons attenuate each other. This process is particularly important at GeV–TeV energies. Pair production with the EBL is discussed in Section 1.4.

Following Lithwick & Sari (2001) and Zhang & Mészáros (2001b), we consider the following situation. For sufficiently high photon energies and sufficiently high photon

densities in the comoving frame, a photon with energy $E'_{\mathrm{max},\gamma\gamma}$ interacts with photons with energy at least

$$E'_{\mathrm{an}} \approx \frac{(m_e c^2)^2}{E'_{\mathrm{max},\gamma\gamma}(1 - \cos\theta)} \tag{2.35}$$

where θ is the angle between the arrival directions of the photons and $1 - \cos\theta$ is of the order of one.

The optical depth of internal pair production can be written as[3]

$$\tau_{\gamma\gamma} \approx \frac{1}{15} \frac{\sigma_{\mathrm{T}} N_{>\mathrm{E,an}}}{4\pi R^2} \tag{2.36}$$

where $N_{>\mathrm{E,an}}$ is the total number of photons with energies larger than E'_{an} and R is the distance of inner engine from the emitting region under investigation. R scales as Γ_{b} in many scenarios, e.g. $R \sim \Gamma_{\mathrm{b}} c \, \delta T$ for prompt emission where δT is the burst variability (Piran, 1999), and $R \sim \Gamma_{\mathrm{b}} c \, t_{\mathrm{dyn}}$ for afterglow emission where t_{dyn} is the expansion time scale before severe deceleration of the emitting material (Zhang & Mészáros, 2001b). It can be seen that $\tau_{\gamma\gamma}$ strongly depends on this distance because of its power of two dependency on R.

We can estimate $N_{>\mathrm{E,an}}$ by assuming a spectral form $L(\nu) = L_{\mathrm{o}}(\nu/\nu_{\mathrm{an}})^{-\beta}$ around $\nu_{\mathrm{an}} = \Gamma_{\mathrm{b}}^2 E'_{\mathrm{an}}/h$ (Zhang & Mészáros, 2001b). Therefore,

$$\begin{aligned}
N_{>\mathrm{E,an}} &\simeq \int_{\nu_{\mathrm{an}}}^{\infty} N_\nu \, t_\gamma \, d\nu \\
&= \int_{\nu_{\mathrm{an}}}^{\infty} \frac{L_{\mathrm{o}}}{h\nu} \left(\frac{\nu}{\nu_{\mathrm{an}}}\right)^{-\beta} t_\gamma \, d\nu \\
&= L(\nu_{\mathrm{an}}) \left(\frac{t_\gamma}{h\beta}\right) \\
&= 4\pi F_\nu(\nu_{\mathrm{an}}) d_{\mathrm{L}}^2 \left(\frac{t_\gamma}{h\beta}\right)
\end{aligned} \tag{2.37}$$

where t_γ is the time scale of the emission. Roughly speaking, $t_\gamma \sim \delta T$ during the prompt phase and $t_\gamma \sim t_{\mathrm{dyn}}$ during the afterglow phase. The relation $L(\nu) = 4\pi F_\nu d_{\mathrm{L}}^2$ was used. Note that the cosmological redshift factor $(1 + z)$ is neglected in the expression. Substituting expression (2.37) into (2.36), it follows that

$$\tau_{\gamma\gamma} \approx \frac{1}{15} \frac{\sigma_{\mathrm{T}}}{h\beta} F_\nu(\nu_{\mathrm{an}}) \frac{d_{\mathrm{L}}^2}{\Gamma_{\mathrm{b}}^2 \, c \, R}. \tag{2.38}$$

Using the scaling relation $R \sim \Gamma_{\mathrm{b}}^2 c \, t_\gamma$, we obtain

$$\tau_{\gamma\gamma} \approx \frac{1}{15} \frac{\sigma_{\mathrm{T}}}{h\beta} F_\nu(\nu_{\mathrm{an}}) \frac{d_{\mathrm{L}}^2}{\Gamma_{\mathrm{b}}^4 \, c^2 t_\gamma}. \tag{2.39}$$

---

[3]The factor 1/15 accounts for a slightly larger estimate (by a factor of $\sim$1/10) by, e.g., Coppi & Blandford (1990) and Böttcher & Schlickeiser (1997) than the analytical value of 11/180 derived by Svensson (1987), as noted in Zhang & Mészáros (2001b).
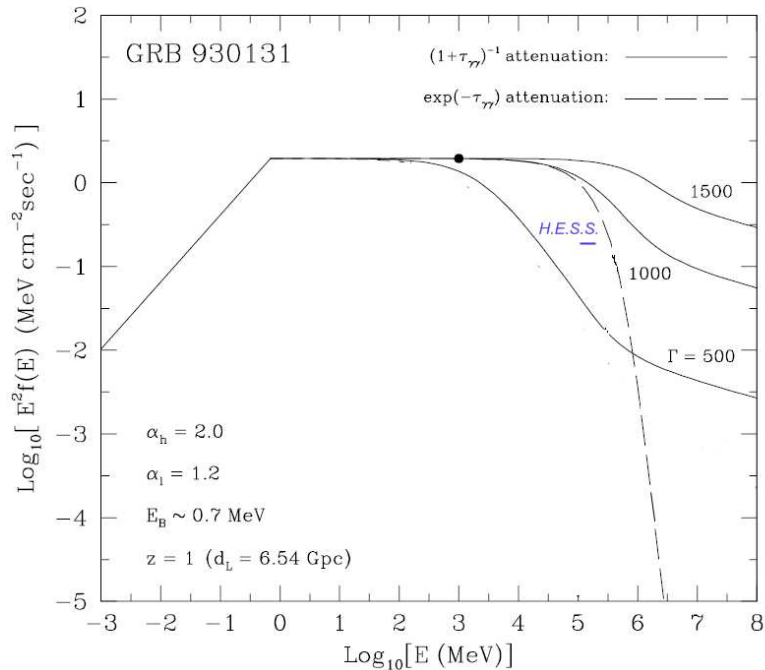
Figure 2.4: Effects of internal pair attenuation in the energy spectrum of GRB 930131 assumed to be located at $z = 1$ (adapted from Baring, 2006). The energy spectrum at energies below 1 GeV is derived from the BATSE and EGRET data, and this is extrapolated to higher energies using an unbroken power law. The filled circle indicates the highest energy EGRET photon at 1 GeV for this burst. The two cases for attenuation are indicated. The H.E.S.S. sensitivity at 200 GeV in 100-second exposure time is shown as a blue line.

It is hence clear that the internal pair attenuation strongly depends on Γ_b. If ν_{an} is above the synchrotron cooling frequency ν_c, from eq. (2.17), we have $\beta = p/2$ and

$$F_\nu(\nu_{an}) = F_{\nu,\max}(\nu_c/\nu_m)^{-(p-1)/2}(\nu_{an}/\nu_c)^{-p/2} \tag{2.40}$$

as happened in the case of slow-cooling during the afterglow phase (e.g. several hours after the burst). In this case, for reasonable parameter values in the external shock model, $\tau_{\gamma\gamma} \approx 1$ for photons at ~ 1 TeV (Dermer et al., 2000; Zhang & Mészáros, 2001b; Pe'er & Waxman, 2005; Galli & Piro, 2007). Therefore, internal pair attenuation is important only for $\gtrsim 1$ TeV photons during the afterglow phase.

During the prompt phase, $\tau_{\gamma\gamma}$ already approaches 1 for photons at ~ 1–10 GeV, for typical values of $\Gamma_b \approx 300 - 500$, as shown in Baring (2006) and Gupta & Zhang (2007). However, for those bursts with a high bulk Lorentz factor ($\Gamma_b > 1000$), internal pair attenuation is important only for photons with energy $\gtrsim 0.1 - 1$ TeV. The extremely optically-bright GRB 080319B may be one of such bursts, based on the assumption that the prompt optical emission comes from a synchrotron component (Racusin et al., 2008).

Neglecting the cascade of the electron/positron pairs, the escaping spectral flux cor-

rected for internal attenuation is given by (Zhang & Mészáros, 2001b; Baring, 2006)

$$F_{\nu,\text{esp}} = \frac{F_{\nu,\text{int}}}{1 + \tau_{\gamma\gamma}} \tag{2.41}$$

instead of the classical formula $F_{\nu,\text{esp}} = F_{\nu,\text{int}} \exp(-\tau_{\gamma\gamma})$, since emission is expected from a skin depth of unit optical depth. The difference between the two attenuation formulae is large, as shown in Figure 2.4 for $\Gamma_\text{b} = 1000$. In Figure 2.4, the H.E.S.S. sensitivity[4] at 200 GeV in 100-second exposure time, comparable to the duration of a long-duration GRB, is shown. EBL absorption according to the 'P0.45' EBL used in Aharonian et al. (2006d) is taken into account, which gives an opacity of $\tau_\gamma\gamma \approx 8.6$ for a 200 GeV photon coming from $z = 1$.

If the redshift of a GRB is known (and thus EBL effects can be accounted for), observations of VHE γ-rays may help to set lower limits of the bulk Lorentz factor of the emitting region of prompt γ-rays and/or afterglow photons, as was done using EGRET data by, e.g., Lithwick & Sari (2001).

2.5 Radiation mechanism for prompt γ-ray emission

The characteristics of prompt γ-ray emission (the GRBs) are summarized below:

- GRB spectra are non-thermal and composed of smoothly joined segments of power laws (Band et al., 1993);

- The peak energies, E_{peak}, of the spectra cluster around $\approx$300 keV, as observed by BATSE (Preece et al., 2000);

- Photons with energies as high as GeV were detected by EGRET and recently also by Fermi/LAT. The fact that these high-energy photons can escape from the production site without being self-attenuated puts a lower limit of the bulk Lorentz factor of the emitting material, Γ_b, at $\sim$100 (Lithwick & Sari, 2001);

- The variability time scale δT, or the duration of individual spikes, is often much smaller than the total duration of the burst (δT can be as small as $1 - 10$ ms; Fishman & Meegan, 1995);

- The energy in the prompt emission is huge ($\sim 10^{51}$ erg; see Frail et al., 2001) and released in individual pulses (c.f. Figure 1.4). Hence, the radiation efficiency must not be small and the radiation must be generated very quickly.

These observations leave two widely-discussed candidates of radiation mechanisms for prompt emission: synchrotron emission or SSC emission. External IC emission model might be viable provided a strong external seed photon field (Zdziarski et al., 1991; Shemi, 1994; Shaviv & Dar, 1995). A quasi-thermal Comptonization model was also proposed (Ghisellini & Celotti, 1999).

---

[4]The sensitivity is the lowest flux detectable at a 5 significance level. Standard cut analysis was used.
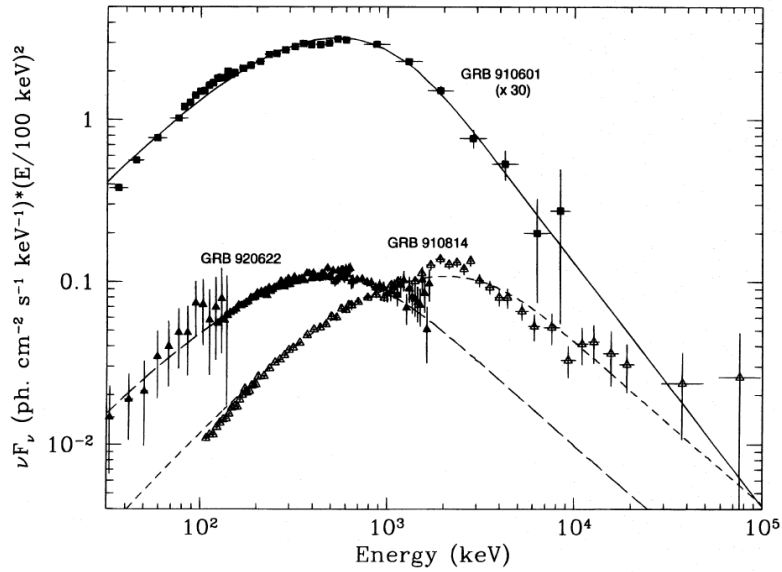
Figure 2.5: A simple optically-thin synchrotron model is consistent with a number of GRB spectra (Tavani, 1996).

2.5.1   Synchrotron emission

Synchrotron emission is the most important radiation mechanism to explain the emission from many astrophysical objects involving relativistic matter, including jets of active galactic nuclei (e.g. Blandford & Königl, 1979) and afterglow emission from GRBs (see later this chapter). Synchrotron emission is believed to generate the observed prompt γ-rays within the widely-discussed fireball-shock model in its external shock version (e.g. Meszaros et al., 1994; Katz, 1994; Dermer et al., 2000) and in its internal shock version (e.g. Pilla & Loeb, 1998; Piran, 1999; Pe'er & Waxman, 2004). Figure 2.5 shows that an optically-thin synchrotron model (the one used in explaining afterglows) is indeed consistent with a number of prompt GRB spectra.

In the optically-thin synchrotron model, the GRB spectrum below E_{peak} is expected to be $F_\nu \propto \nu^{1/3}$, or more probably the softer $F_\nu \propto \nu^{-1/2}$ which is the case for fast-cooling in order that the radiation is emitted with high efficiency. This expectation is independent of the exact shape of the particle distribution (Piran, 2005). However, not only is this "clustering" of the low-energy power-law index not observed in BATSE data, about one-fifth of BATSE bursts exhibit harder spectra than $F_\nu \propto \nu^{1/3}$ which are inconsistent with the model. This is the so-called "line of death" problem of the synchrotron model (Preece et al., 1998). Models invoking an additional thermal-Compton component from the photosphere superimposed on the synchrotron component may solve this problem, as well as explain the seemingly clustering of E_{peak} values seen by BATSE (e.g. Pe'er et al., 2007). The distributions of the spectral indexes α and β in the Band-function (eq. 1.1) fits of BATSE bursts are also argued to contradict the simple synchrotron spectrum (Ghisellini et al., 2000; Preece et al., 2002).

2.5.2   Synchrotron self-Compton emission

An alternative to the synchrotron model for prompt γ-rays is the synchrotron self-Compton model. In this case, the synchrotron component peaks in the IR/optical/UV band (e.g. Mészáros & Rees, 1994; Stern & Poutanen, 2004). Kumar & McMahon (2008) performed a robust analysis on the parameter space in the optically-thin regime. In their analysis, R_γ is found to be too large in the synchrotron model. This is a crucial argument which leads them to conclude that the SSC model for prompt γ-rays serves better than the synchrotron model. The *naked-eye* optical emission accompanying GRB 080319B (with a similar temporal profile) provides a fairly strong support to the SSC interpretation (Racusin et al., 2008; Kumar & Panaitescu, 2008).

In order that SSC is viable to produce the observed high soft γ-ray fluence, the Compton parameter $Y = U'_{\rm rad}/U'_{\rm B}$ (i.e. the ratio of the IC flux to the synchrotron flux) must be high. As we see below, prompt optical observations put very stringent lower limits on Y for many bursts, resulting in $Y \gtrsim 1000$ for the majority of bursts (Piran et al., 2008). Using eq. (2.27), this implies

$$\epsilon_{\rm B} \lesssim 2 \times 10^{-6} \eta_{\rm rad}(\epsilon_{\rm e}/0.5). \tag{2.42}$$

meaning the magnetic field energy density is much lower than the equipartition value. Therefore, the SSC mechanism for prompt γ-rays does not work in Poynting-flux dominated models.

Prompt optical observations provide a very stringent constraint to the SSC interpretation. Yost et al. (2007a,b) presented detections or upper limits from optical observations *before* the end of the prompt γ-ray emission. Figure 2.6 shows optical-to-γ-ray spectral indices ($\beta_{\rm opt-\gamma}$) versus γ-ray spectral indices (β_γ), derived from simultaneous optical and γ-ray observations during the prompt phase of GRBs. Apart from several important exceptions (e.g. GRB 990123 and GRB 061007), most optical-to-γ-ray spectral indices ($\beta_{\rm opt-\gamma}$) are constrained to be > -0.5 where $F_\nu \propto \nu^\beta$. Most observations were taken in R-band ($\nu_{\rm R} \approx 4 \times 10^{14}$ Hz) and in soft γ-ray band ($\nu_\gamma \approx 1.5 \times 10^{19}$ Hz). It follows that the energy flux ratio between these two bands is

$$\frac{\nu_\gamma F_\gamma}{\nu_R F_R} \gtrsim 10^4. \tag{2.43}$$

This is not readily the Compton parameter, since the synchrontron/IC peak may not lie in the corresponding band. However, the lower limit on the Compton parameter is still of the order of 10^3 (Piran et al., 2008).

Within the framework of the SSC model and under the assumption that most of GRB fluence is in the form of soft γ-rays (as verified observationally for most GRBs), Derishev et al. (2001) derived a very low upper limit on the bulk Lorentz factor ($\Gamma_{\rm b} \lesssim 25$), which is in contradiction to the observed MeV–GeV photons (Lithwick & Sari, 2001). Under the same constraint, Piran et al. (2008) pointed out that a huge amount of energy would be emitted as a second-IC component due to the very high Compton parameter, resulting in an *energy crisis*.
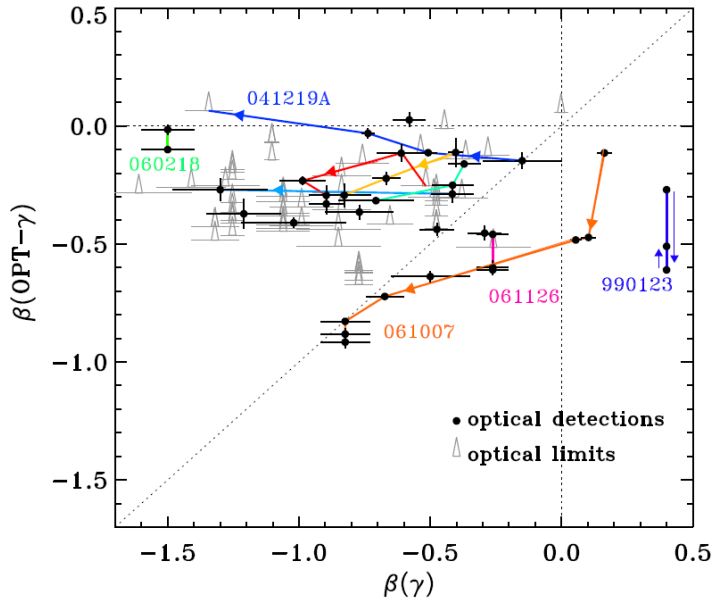
Figure 2.6: Optical-to-spectral indices ($\beta_{\mathrm{opt}-\gamma}$) plotted against γ-ray spectral indices (β_γ), derived from simultaneous optical and γ-ray observations during the prompt phase of GRBs. Black points represent optical detections, whereas grey triangles represent optical limits. The latter indicate the softest possible $\beta_{\mathrm{opt}-\gamma}$ (Yost et al., 2007a,b).

2.5.3 Detection prospects of VHE emission during the prompt phase

IC scattering of the prompt sub-MeV γ-rays, whether originating from synchrotron emission, SSC emission, or other mechanisms, should give rise to an/another IC peak at higher energies. VHE γ-rays ($\gtrsim 100$ GeV) are attenuated by the lower energy photons via pair production ($\gamma + \gamma \to e^+ + e^-$) because of the high photon densities in the source. It seems, however, that such opacity needs time to 'build-up' (Pilla & Loeb, 1998; Granot et al., 2008), indicating that VHE photons may escape from the source near the onset of the burst or individual spikes, before the low-energy *target* photons have time to accumulate. From our discussion in Section 2.4, the opacity depends on the bulk Lorentz factor and the location, R_γ, of the emission region as $\tau \propto 1/(\Gamma_b^2 R_\gamma)$ (c.f. eq. 2.38). From Figure 2.4, $\Gamma_b \geq 1000$ is needed in order that the opacity for a ~ 100 GeV photons to be unity. The dependency of the opacity on Γ_b and R_γ does not rely on the details of the generating mechanisms of high energy photons.

Kumar & McMahon (2008) compare the synchrotron and SSC models for generating the sub-MeV flux in a generic way. In both models, an IC component is expected, albeit in different energy ranges, as demonstrated in Figure 2.7. Klein-Nishina correction for IC scattering and pair production are included in the calculations, but not the EBL absorption. As shown, the synchrotron model produces an IC peak at ~ 1 TeV[5] and a flux of the order of 10^{-9} erg cm^{-2} s^{-1}, with a sharp cutoff above the peak due to

---

[5]This value is relatively high, probably due to the large R_γ obtained in their calculations.
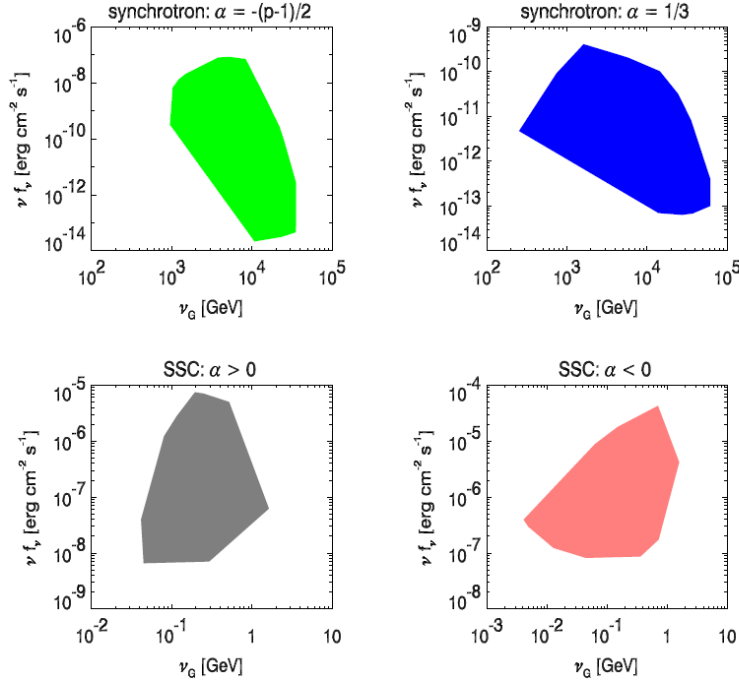
Figure 2.7: Comparison of the expected GeV/TeV emission from numerical calculations of the IC scattering of prompt γ-ray photons. The peak of IC spectrum (v_{G}) and the energy flux (νF_ν) at the peak in the synchrotron model (top two panels) and the SSC model (bottom two panels). The spectral index α of the *seed* soft γ-ray spectrum at $\nu = 100$ keV with flux $F_\nu = 0.1$ mJy is assumed (Kumar & McMahon, 2008).

pair production. In the SSC model the spectrum of the second IC scattered photons peaks at ~ 1 GeV, with a flux of 10^{-6} erg cm^{-2} s^{-1}. While EGRET probably provided some constraints to this GeV component, the expected flux is well within the sensitivity of Fermi/LAT. In the case where no such a component is detected by LAT, the SSC model is not preferred. On the other hand, VHE observations of nearby GRBs would be more suited to probe the synchrotron model, from which the IC peak is located at ~ 1 TeV (Kumar & McMahon, 2008).

If GRBs originated from external shock, pair-production opacity is much lower and the expected VHE flux would readily be detected by high-energy instruments (e.g. Dermer et al., 2000; Galli & Piro, 2007).

If the emitting region of GRBs is Poynting-flux dominated (e.g. Lyutikov & Blandford, 2003), instead of kinetic energy dominated (as in the shock models), no strong VHE emission is expected from IC scattering, because the much higher magnetic field density implies a much smaller Compton parameter.

2.6   Radiation mechanism for Afterglows

The general (segmented) power-law characteristic of the spectra and light curves observed in the lower energy bands (e.g. X-ray, optical, and radio bands) indicates a non-
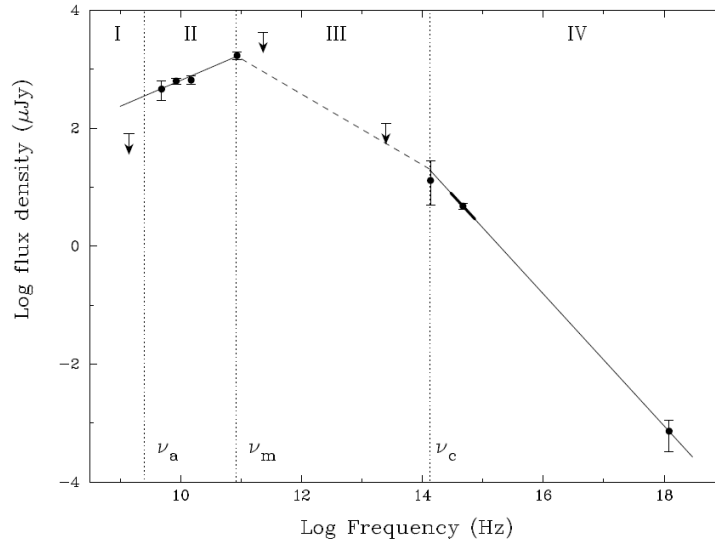
Figure 2.8: The board-band spectrum of GRB 970508 over nine orders of magnitude in frequencies is consistent with a synchrotron spectrum from a blast-wave accelerated electrons in the fireball model (Galama et al., 1998).

thermal origin of the radiation mechanism of GRB afterglows. Synchrotron emission from blast-wave[6] accelerated electrons in the context of the fireball model is a widely accepted model to explain the general behavior of GRB afterglows (see, e.g. Piran, 1999; Zhang & Mészáros, 2004). This model had been proposed (e.g. Paczynski & Rhoads, 1993; Katz, 1994) several years before the discovery of the afterglows (Costa et al., 1997). Figure 2.8 shows nearly all characteristics of a synchrotron spectrum as expected from the simplest version of the blast wave model (Piran, 1999). Compared to the radiation mechanism responsible for the prompt γ-ray emission, that of the afterglow emission is more well understood, although alternative models exist, such as the 'cannonball' model (Dar & De Rújula, 2004), in which afterglows are due to bulk IC emission of the ambient light from canonical core-collapse supernovae.

Since 2004, X-ray Telescope (XRT) on board *Swift* has revealed some peculiar behaviors (in view of the pre-*Swift* era) in many of the light curves of the X-ray afterglows, most notably the fast-decaying phase followed by the slow-decaying (or 'plateau') phase (Nousek et al., 2006), X-ray flares (Chincarini et al., 2007), and chromatic X-ray light curve breaks which are not accompanied by optical breaks (Panaitescu et al., 2006). A 'canonical' X-ray afterglow light curve based on *Swift*/XRT observations is shown in Figure 2.9. These features are *not* predicted nor explained by the simplest version of the blast wave model (Zhang et al., 2006). Modifications of the simple model have been made or re-iterated in order to reproduce the observations. These include, e.g., prolonged inner engine activities in the afterglow phase (Fan et al., 2008) and the highly-radiative blast wave model (Dermer, 2007).

---

[6]A blast-wave is formed whenever the mass of swept-up circumburst material is comparable to the kinetic energy carried by the fireball ejecta.
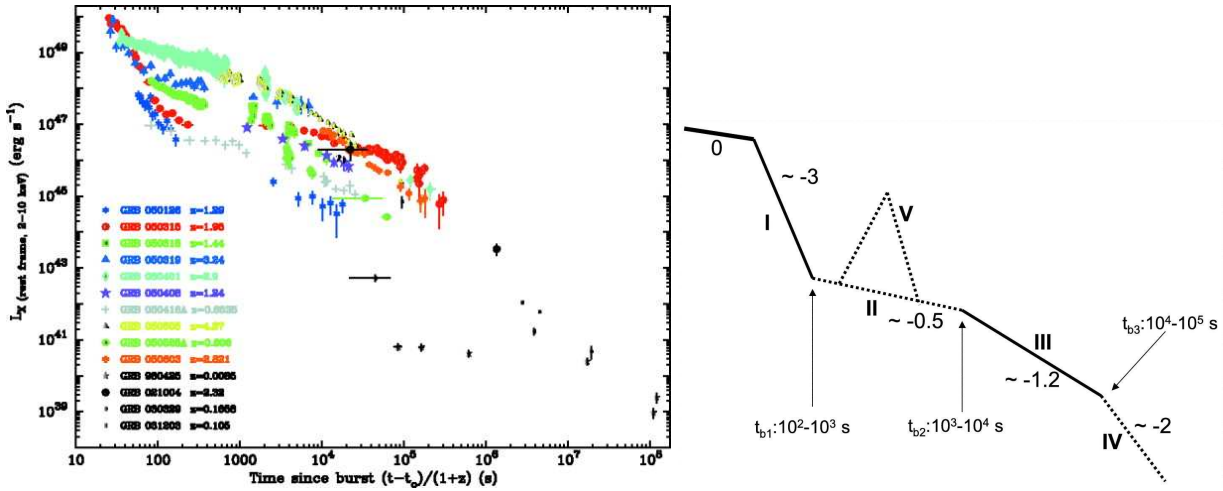
Figure 2.9: *Left panel*: 2-10 keV X-ray luminosity versus time for Swift GRBs with redshifts (colored symbols), plotted with Chandra's late-time data of GRB 980425 (black dots; Nousek et al., 2006). *Right panel*: *Swift*/XRT observations reveal a 'canonical' X-ray afterglow light curve of GRBs. Note that not all X-ray afterglows exhibit every feature shown (Zhang et al., 2006).

2.6.1 Detection prospects of VHE emission during the afterglow phase

Afterglow photons are believed to be generated at larger distances ($\sim 10^{16} - 10^{17}$ cm) from the inner engine, because they are simply observed after the prompt γ-rays and almost all GRB models involve a relativistic ejecta moving towards us. Due to the much lower photon densities at the emitting location of the afterglows, the opacity due to photon-photon pair production is much lower and even TeV photons can escape from the source.

If the lower energy emission seen in X-ray, optical, and radio bands is due to electron synchrotron emission (as supported by the rich information deduced from afterglow observations at lower energies during the *Swift* era), it is natural to expect that IC emission (be it SSC or external-IC) should accompany the contemporary low energy emission. In this context, Dermer et al. (2000), Pe'er & Waxman (2005), and Galli & Piro (2007) predict the high-energy emission during the afterglow phase (c.f. Figures 7.1 and 7.2). Fan et al. (2008) suggest that the temporal evolution of the SSC emission is very similar to the observed X-ray afterglow light curve (Figure 2.9).

To demonstrate that these models predict detectable IC flux, Figure 2.10 depicts the predicted synchrotron and IC spectra in an external shock model[7] calculated for the cases of 'standard' afterglow phase and X-ray flare. As seen in the figure, the modeled IC flux is above the sensitivity level of both high-energy instruments (LAT and H.E.S.S.) at different photon energies ($\sim$100 MeV for LAT and $\sim$200 GeV for H.E.S.S.). The integration/exposure times of observation are chosen to match the time elapsed after the GRB or the X-ray flare, except that a 2-hour exposure time for H.E.S.S. in the former

---

[7]in which no internal shocks are needed to explain the prompt γ-ray emission
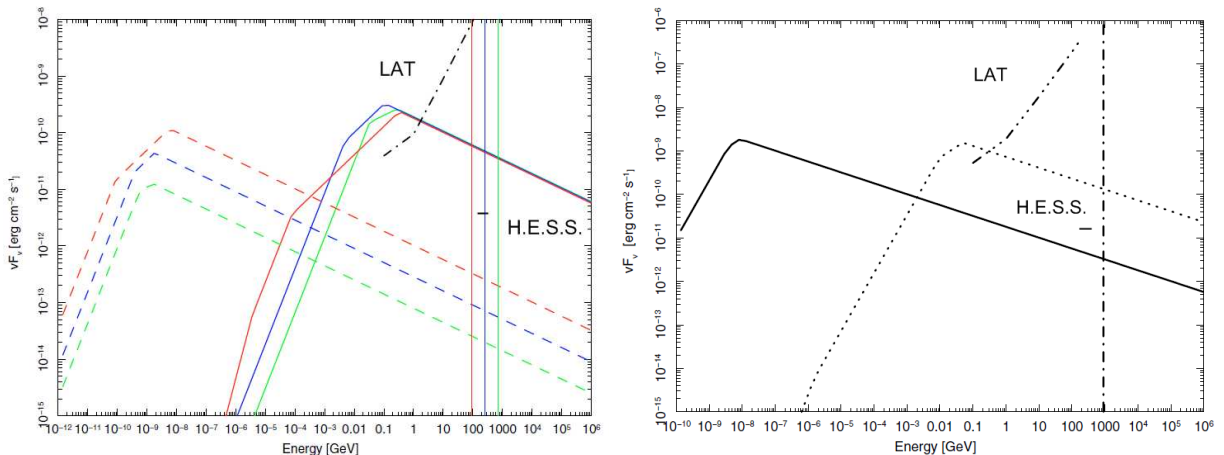
Figure 2.10: Predicted synchrotron (dashed lines) and IC (solid lines) spectra for a thin shell fireball 10^5 s after the burst (*left panel*) and for a thick shell fireball 500 s after an X-ray flare (*right panel*). A redshift of one is chosen in both cases. Green, blue, and red spectra are calculated using $\epsilon_B = 10^{-4}$, 10^{-3}, and 10^{-2}, respectively. The vertical lines (in both panels) indicate the energy in the observer's frame at which $\tau_{\gamma\gamma} = 1$ (c.f. eq. 2.39). The H.E.S.S. differential sensitivity at 200 GeV for a 5 significance level detection in 3600-/600-s (left/right panel) exposure time, for a Crab-like spectrum are shown as short horizontal lines. The LAT sensitivity for a 5 significance level in an integration time of $10^5/500$ s (left/right panel) are also shown (Galli & Piro, 2007).

case is chosen to match the nominal observing strategy deployed for the H.E.S.S. GRB program (c.f. Section 3.2). Therefore, the two instruments are complementary to each other to test this or similar models. The GRB is assumed to locate at $z = 1$ in plotting this figure. The absorption of VHE photons by the EBL is not included in the figure, the opacity of this process is of the order of unity for a GRB at $z \sim 0.5$.

Observations of nearby GRBs (e.g. $z \lesssim 0.5$) at high energies can therefore provide an independent probe of the afterglow models[8]. These observations may validate or challenge the current understanding, as well as test schemes proposed to explain the X-ray behaviors (Fan et al., 2008).

2.7   Contributions from accelerated protons

If protons are accelerated efficiently by similar mechanisms that accelerate electrons responsible for prompt γ-ray emission and lower energy afterglow emission, several radiation mechanisms due to these energetic protons are important for high energy γ-ray observations. The acceleration time scale for a proton to attain the same Lorentz factor as an electron $\gamma_p = \gamma_e$ is a factor of m_p/m_e larger (c.f. eq. 2.6), assuming the same $\eta_{\rm acc}$ for both kinds of particles. The emission initiated by protons is generally expected to decay more slowly than the electron sub-MeV radiation (Böttcher & Dermer, 1998).

---

[8]For a detailed discussion on detection prospects of VHE emission from an SSC afterglow model including EBL absorption and comparisons with observational data of nearby GRBs, see chapter 5

2.7.1   Synchrotron emission

Similar to electrons, protons can also produce synchrotron emission. The synchrotron power of a proton is smaller by a factor of $(m_e/m_p)^2$ than an electron with the same Lorentz factor (c.f. eq. 2.8). If most of the energy in the emitting regions of GRBs resides in protons, one may expect a large proportion of bolometric fluence to be emitted in the TeV band in a time scale of up to days after the prompt γ-ray emission (Totani, 1998a).

Zhang & Mészáros (2001b) studied the relative importance of proton synchrotron emission and electron IC emission at high energies in the afterglow phase. They found that for proton synchrotron emission to dominate over the electron IC emission at high energies, a strong magnetic field and a very small fraction of total energy transferred to electrons, or $\epsilon_e/\epsilon_B \leq 10^{-2}$, are needed, which is incompatible with the findings of afterglow modeling (e.g. Panaitescu & Kumar, 2002). Moreover, even if bursts with such 'fine-tuned' parameters exist, they are at least 3–4 orders of magnitude less luminous than those bursts with IC dominance, and the frequency range where the proton synchrotron emission finds itself dominant is uncomfortably narrow (compare Figure 2a and Figure 2b in Zhang & Mészáros, 2001b). For the prompt phase, the parameter space where proton synchrotron emission is important is also limited to a small region where $\epsilon_B/\epsilon_e > 10$ (Asano & Inoue, 2007).

2.7.2   Pion decay

Because of the high radiation energy density in GRB emitting region, the most important hadronic processes are the interaction of energetic protons with soft γ-rays:

$$p + \gamma \rightarrow \Delta^+ \rightarrow \pi^0 + p$$
$$p + \gamma \rightarrow \Delta^+ \rightarrow \pi^+ + n$$
(2.44)

with a threshold photon energy $E_{\rm th} = m_\pi + m_\pi^2/(2m_p) \approx 150$ MeV. Apart from these *single-pion* resonance channel, *multi-pion* channel can produce secondary π^0, π^+, and π^- particles. Pions thus produced then decay:

$$\pi^0 \;\; \rightarrow \;\; \gamma + \gamma$$
$$\pi^+ \rightarrow \mu^+ + \nu_\mu \;\; \rightarrow \;\; e^+ + \nu_e + \bar{\nu}_\mu + \nu_\mu$$
$$\pi^- \rightarrow \mu^- + \bar{\nu}_\mu \;\; \rightarrow \;\; e^- + \bar{\nu}_e + \nu_\mu + \bar{\nu}_\mu.$$
(2.45)
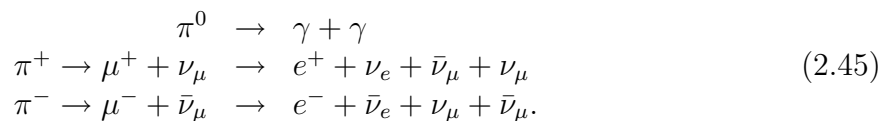
The minimum photo energy resulted from π^0-decay is $\sim 75 \, \Gamma_{\rm b}$ MeV in the *engine's frame*. These charged particles may in turn produce synchrotron emission. Together with Compton processes and pair production, electromagnetic cascades follow. The effects of pion decay in GRB emitting region have been considered in, e.g. Böttcher & Dermer (1998) for the afterglow phase and in, e.g. Asano & Inoue (2007) for the prompt emission phase. Figure 2.11 shows modeled broad-band afterglow spectra including contribution from energetic hadrons. This model predicts a large contribution to $\gtrsim 10$ MeV spectrum from hadronic emission.

In general, the importance of these hadronic processes on GRB spectra relies on the energy of protons compared to electrons. It remains to be probed that whether the predicted photon flux resulted from such processes is comparable to leptonic IC component, and therefore detectable by high-energy detectors.
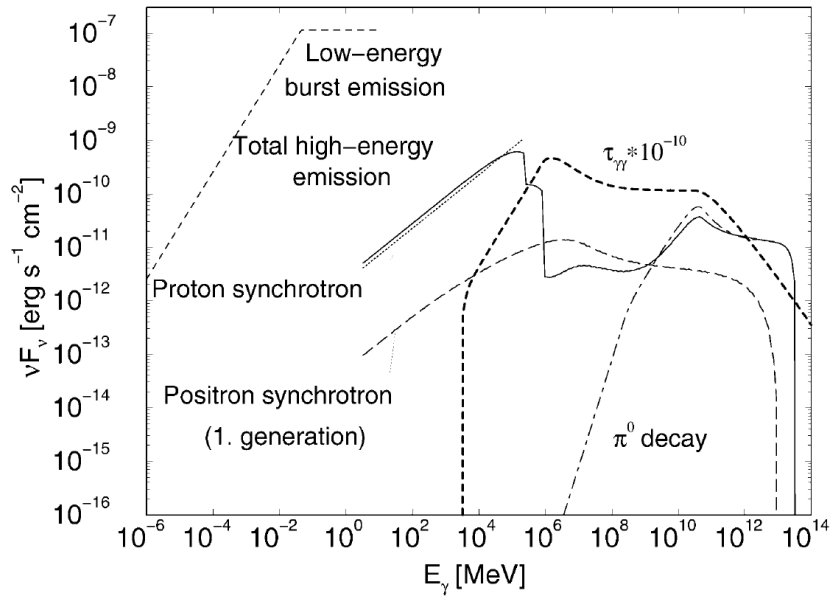
Figure 2.11: Modeled high-energy (>1 MeV) spectrum of a GRB blast wave at the deceleration radius for GRB 970508 (Böttcher & Dermer, 1998). Proton synchrotron emission and emission from cascade products of hadronic processes are indicated. Optical depth of pair attenuation (scaled by a factor 10^{-10}) is also shown, which is larger than unity at >200 GeV. EBL absorption is not considered in this figure, which is expected to take effects for this burst at z=0.835 above ~100 GeV (Primack et al., 2005; Franceschini et al., 2008).

Chapter 3

The H.E.S.S. experiment and the γ-ray burst observing program

3.1 The H.E.S.S. System

The H.E.S.S. array[1] is a system of four 13m-diameter IACTs located at $1\,800$ m above sea level in the Khomas Highland of Namibia ($23°16'18''$ S, $16°30'00''$ E). Each of the four telescopes (see Figure 3.1) is placed at a corner of a square with a side length of 120 m. This configuration was optimized for maximum sensitivity to $\sim$100 GeV photons. The effective collection area increases from $\sim 10^3 \mathrm{m}^2$ at 100 GeV to more than $10^5 \mathrm{m}^2$ at 1 TeV for observations at a zenith angle (Z.A.) of $20°$. The system has a point source sensitivity above 100 GeV of $\sim 1.4 \times 10^{-11} \mathrm{erg\,cm^{-2}\,s^{-1}}$ (3.5% of the flux from the Crab nebula) for a 5σ detection in a two-hour observation.

Each H.E.S.S. camera consists of 960 photomultiplier tubes (PMTs). Since each of the PMTs has a field of view (FoV) of $0°\!.16$, in total they provide a camera FoV of $\sim 5°$, i.e. the area where Cherenkov light can be recorded. Because of the detection principle of IACTs, γ-rays with arrival directions slightly outside this camera FoV can also be detected[2]. This relatively large FoV has at least the following three advantages:

1. It allows for the study of extended objects including RX J1713.7$-$3946;

2. It enhances the ability to detect serendipitous sources, as demonstrated in the Galactic plane survey (Aharonian et al., 2005c) and the simultaneous VHE γ-ray observations of transient objects detected in other wavebands. The analysis and results of the observations of such an event (GRB 060602B) will be discussed in Section 6.

3. It allows for the simultaneous determination of the background events from off-source positions, so that no dedicated off run is needed (Aharonian et al., 2006b). This technique of background determination is used in the analysis presented in chapters 4 and 6;

---

[1] http://www.mpi-hd.mpg.de/hfm/HESS/HESS.html
[2] For details, the reader is referred to Section 6.8

Figure 3.1: One of the four H.E.S.S. telescopes located in Namibia

The slew rate of the array is ∼100° per minute, enabling it to point to any sky position within 2 minutes.

The trigger system of the H.E.S.S. array is described in Funk et al. (2004). The stereoscopic technique is used, i.e. a coincidence of at least two telescopes triggering within a window of (normally) 80 nanoseconds is required. This largely rejects background events caused by local muons which trigger only a single telescope.

Observations of GRBs reported in this thesis were obtained over a long period, starting from the year 2003. Therefore, the number of telescopes and the observation mode have changed between 2003 and 2004. The observations of two GRBs in 2003 were made using two telescopes while the system was under construction. Before July 2003, each of the two telescopes took data separately. Stereo analysis was then performed on the data which requires coincidence of events to be determined offline using GPS time stamps. After the installation of the central trigger system in 2003 July, the stereo multiplicity requirement was capable of being determined simultaneously with observations. All observations since 2004 made use of the completed four-telescope array and the stereo technique as described in (Aharonian et al., 2006b).

Most of the data were taken in 28 minute runs using *wobble* mode, by placing the targeted object at an ±0.5° offset in declination/right ascension from the center of the camera FoV, in order to reduce possible systematics due to inhomogeneous response in the camera FoV All data products presented in this thesis were derived from data taken in good weather conditions at times with good hardware status.

3.1.1   Analysis cuts

Analysis cuts are used to differentiate photons from cosmic rays which form the vast majority of events. Among different kinds of cuts used in H.E.S.S. data analysis, standard cuts and soft cuts are the two used most frequently in this thesis. They are suitable to search for point sources of *gamma*-rays, as would be expected for GRBs. The cuts on mean reduced scaled width (MRSW) and length (MRSL) parameters (Aharonian et al. 2005a), θ_{cut} (the angular distance between the reconstructed shower direction and the

Table 3.1: The standard, standard (off, i.e. large offset), and soft analysis cuts applied to the GRB data. Only images passing the distance and size cuts are used in the analysis, and at least images obtained by two cameras are required.

Cut	MRSL min (σ)	MRSL max (σ)	MRSE min (σ)	MRSW max (σ)	θ_{cut} max (°)	Size min (#PE)	Dist. max (°)	applicable offsets (°)
standard	-2.0	2.0	-2.0	0.9	0.11	80	2.0	0–2.5
standard (off)	-2.0	2.0	-2.0	0.9	0.32	80	2.0	2.5–3.0
soft	-2.0	1.3	-2.0	0.9	0.14	40	2.0	0–2.5

GRB position), individual image size (number of photoelectrons, PE), and the distance of the image center of gravity from the center of the FoV, are shown in Table 3.1. The standard cuts are optimized *a priori* using Monte Carlo γ-ray simulations and unrelated off-source data to yield the maximum expected significance per hour of observation for a source with 10% Crab flux and power-law photon index $\Gamma = 2.6$. The soft cuts are optimized for a source with 1% Crab flux and power-law photon index $\Gamma = 5.0$. The special standard (large offset) cuts are used in the analysis of the large offset data of GRB 060602B (c.f. section 6.4).

3.1.2   Effective collecting area

The effective area is equal to the geometrical area of the Cherenkov light pool multiplied by the photon acceptance, as determined by MC simulations. The photon acceptance is the ratio of photons passing analysis cuts divided by the total number of photons emitted by the simulated source. It follows that the effective area depends on the analysis cuts used.

3.1.3   Energy threshold

The energy threshold, E_{th}, is conventionally defined as the peak in the differential γ-ray rate versus energy curve (Konopelko et al., 1999). This curve is a convolution of the effective area with the expected energy spectrum of the source as seen on the Earth. The energy threshold defined as such is sometimes called the peak-rate energy threshold. It is noted that γ-ray photons with energy below E_{th} (and above the *trigger threshold*) can indeed be detected by the telescopes. The energy threshold depends on the Z.A. of the observations, the assumed spectral index Γ, and the analysis used. Assuming a $\Gamma = 2.0$ spectrum, this curve is shown in Figure 3.2 for standard-cut analysis and soft-cut analysis. For standard-cut analysis, the energy thresholds are 280 GeV, 660 GeV, and 1.9 TeV for a Z.A. of 20°, 45°, and 60°, respectively. For soft-cut analysis, the energy thresholds are 230 GeV, 540 GeV, and 1.9 TeV for a Z.A. of 20°, 45°, and 60°, respectively. Therefore, the larger the Z.A., the higher is the energy threshold. For a softer spectrum (e.g. $\Gamma = 2.6$, as used in Section 4.4), the threshold is lower since the peak is shifted to lower energies as a result of a large number of low-energy photons.
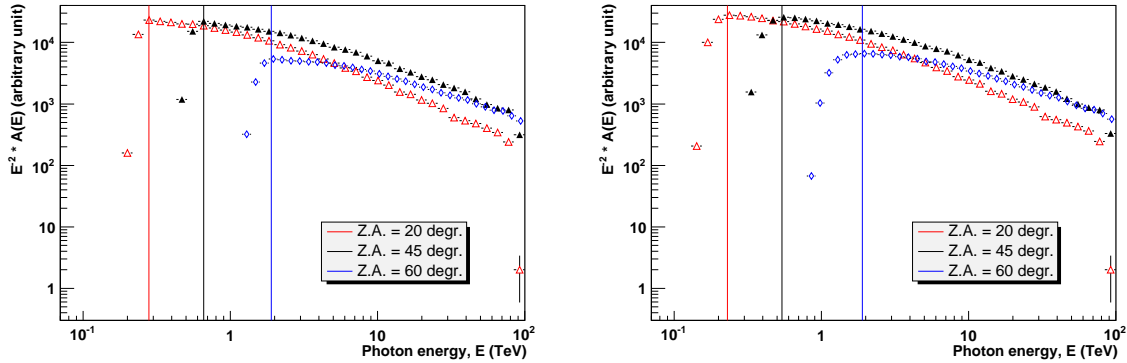
Figure 3.2: Differential γ-ray rate versus energy curve for standard-cut analysis (left) and soft-cut analysis (right). This curve is a convolution of the effective area (which differs for different cuts used) with the expected energy spectrum of the source as seen on the Earth. A spectral index of 2.0 is assumed for both cases. The vertical lines indicate the peak of this curve (i.e., the energy threshold) for each Z.A. For standard-cut analysis, the energy threshold is 280 GeV, 660 GeV, and 1.9 TeV for a Z.A. of 20°, 45°, and 60°, respectively. For standard-cut analysis, the energy threshold is 230 GeV, 540 GeV, and 1.9 TeV for a Z.A. of 20°, 45°, and 60°, respectively.

3.2   The Gamma-ray burst observing program

GRBs arrive from any (non-predictable) directions from the sky without precedent in astronomy. This poses a big challenge to study their *prompt* and *afterglow* phase simultaneously in any other wavelength[3], including the VHE γ-ray regime. Therefore, observations of GRBs or not, unlike most other sources, require a timely decision (from seconds to hours) and for H.E.S.S., these are done using alerts of GRBs through the Gamma-ray Burst Coordination Network (GCN[4]) in real-time.

3.2.1   Receiving signal from the cosmos

The GCN grew out from the BATSE COordinates DIstribution NEtwork (BACODINE), which, as its name suggests, distributed the RA and Dec locations of the GRBs detected by the BATSE experiment on board CGRO satellite to various observational sites around the globe (Barthelmy et al., 1994).

Back in the 1990s, the distance scale of GRBs was still not clear. While the isotropic spatial distribution of GRBs were established, there were theories putting them as near as 10^4 AU (e.g., from the Oort Cloud surrounding the solar system; Dermer, 1996), or of the order of Giga-parsecs (e.g., from mergers of compact objects; Narayan et al., 1992). It was argued that the detection of counterparts in other wavelengths may put some constraints on the distance scale of GRBs. Therefore the BACODINE network was set up to distribute

---

[3]This was the main reason why GRBs remained a mystery for a long time before the first identification of lower energy counterparts, as mentioned in Section 1.2.

[4]http://gcn.gsfc.nasa.gov/

GRB locations within a few seconds after the trigger, so that any possible counterpart might be captured quickly enough before they faded below the detection limits of the available instruments. Subsequently, GRB triggers from other spacecrafts have also been incorporated (and thus renamed "GCN") and information not only on burst locations but also on images and/or light curves of prompt emission/afterglows are also distributed to the registered sites (who can select which products they want). This proved to be a great success. Nowadays several hundred observation sites are receiving information of satellite-triggered GRBs continuously by means of internet sockets, pagers, and E-mails, in order to make timely observations of GRBs during the prompt and afterglow phases.

In the H.E.S.S. collaboration, the Multi-wavelength Working Group[5] has been responsible for candidate GRB observations. Until the end of 2004, whether or not to observe a GRB position was discussed and decided only after the burst trigger, i.e. decisions were made at best hours after the burst. In this mode the observations of GRB 030329, GRB 030821, GRB 040425, GRB 041006, and GRB 041211B were carried out. At the beginning of 2005, a GRB coordination team[6] formed and an automatic alerting program was implemented on site (this program written in C++ programming language is called the "Alerter" hereafter) to keep the shift crew alerted of any observable, candidate GRBs as soon as possible. This improvement largely shortens the delayed time of the observations with respect to the burst time.

A group mailing list as well as a wiki page (Figure 3.3) has been set up to facilitate discussion between GRB team members about individual GRB observations and the general strategy of the GRB observation program.

Once every month one member from the GRB coordination team becomes the *contact person*, who supports the shift crew by giving professional advices on GRB observations and keeps track of possible GRB observations (and detection or not) and related information available such as the (or lack thereof) redshift of a GRB. She/he is also responsible to make sure that information flow of possible GRB observations (via E-mails, phone calls, and the wiki page) is sufficient.

We have received on-board GCN notices (or alerts) distributed by the *Swift* satellite (via machine-readable socket packages using an automated programm running on site and E-mails), as well as alerts from INTEGRAL and HETE-II (mission ended March 2006) confirmed by ground-based analysis (via E-mails only). A large majority of all triggers have been *Swift* triggers during the years 2005–2008. Once available, alerts distributed by the Fermi/LAT instrument will also be implemented.

The Alerter has been running on site since the beginning of 2005. I have been responsible for its maintenance since the beginning of 2006. In the following section, I briefly describe how the Alerter handles the incoming GCN notices through internet socket connection.

---

[5]http://www.lsw.uni-heidelberg.de/projects/hess/HESS/hessmultnu.phtml

[6]comprising of $\sim$10 people in the collaboration from various countries including Australia, France, Germany, and the United Kingdom. Since the beginning of 2006, I have been responsible for maintaining this shift rota.
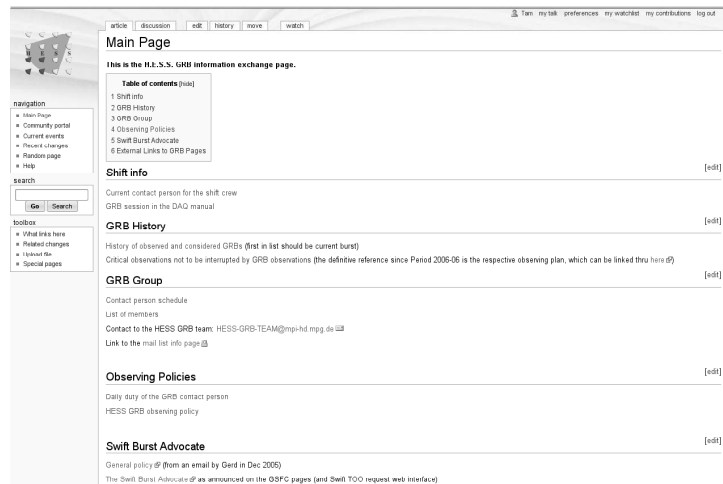
Figure 3.3: The wiki page used to facilitate discussion between GRB team members about individual GRB observations. It also contains the general strategy of the GRB observation program.

3.2.2   Maintenance of the Alerter

After a GCN notice is sent out, it takes only 1–2 seconds to arrive to the H.E.S.S. site through socket connection. When the Alerter receives a GCN notice, it determines whether it carries information of a genuine GRB, based on some pre-defined criteria. These criteria may be different from one observing site to another, depending on, e.g. the scientific purposes of the site. For example, an optical telescope built primely for GRB observations may be following every notice (be it from a genuine GRB or not), while other sites are more selective due to their relatively limited available time for GRB observations. as to H.E.S.S., it is more desirable that the GCN notices being followed are from genuine GRBs, than that most observation time for GRBs is spent on fake alarms.

The pre-defined criteria of one type of GCN notices, the *Swift*-BAT GRB Position notices which is particularly important in the H.E.S.S. GRB observation program, has been fine-tuned several times during the past years. I have been responsible for the implementation of these changes to the "Alerter" from April 2006 on. This involves changing the "Alerter" code according to the criteria, testing the modified code using test-bed machines, and upgrading the "Alerter" on site with the verified code.

3.2.3   Observation Strategy

After retrieving the coordinates given in a GCN position notice, the "Alerter" determines the observation time window during which the candidate GRB position is smaller than a Z.A. of 45° during H.E.S.S. dark time[7]. The $0° - 45°$ requirement on Z.A. ensures a

---

[7]described in Section 3.3

```
Jun ├─ 2007 ├─────────────────────────────────────────────────────┤ Jun
              18h            0h            6h          UTC
RA: 21:35:36     Dec: -24:47:02     (GRB 070621)
Gal.long.:   24:26   Gal.lat.: -46:06
Altitude: ■ 0      ■ 30    ■ 45    ■ 60
Geo.long.:   16:30.0  lat.: -23:16.3
```
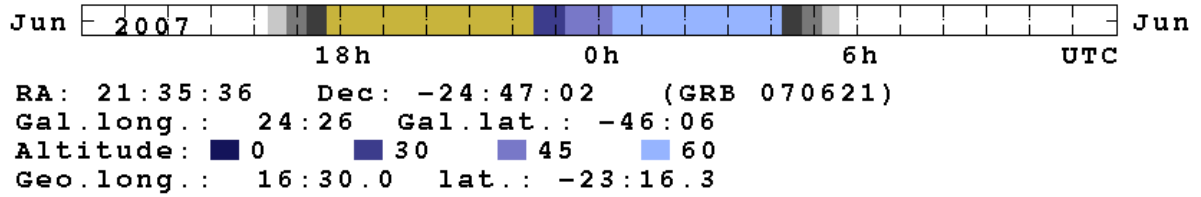
Figure 3.4: the altitude of the GRB 070621 sky position (RA= $21^\mathrm{h}35^\mathrm{m}36^\mathrm{s}$, Dec.=$-24°47'2''$) in the night of June 21–22, 2007. The period when the position is above given altitudes are indicated by the blue colors. The white and grey areas indicate the times of daylight and twilight. The yellow region indicates that the moon is up. The burst triggered *Swift*/BAT (#282808) at June 21, 2007, 23:17:57 UT, when the sky position is at a zenith angle smaller than 45°. This burst was observed until the end of the night.

relatively low energy threshold (as discussed in Section 3.1.3). If such an observation time window exists and is longer than ∼30 minutes within the next 24 hours, the GRB position is then *observable*. As an example, the altitude of the GRB 070621 position in the night of June 21–22, 2007 is shown in Figure 3.4. The observation time window started when the burst occurred (23:17:57 UT at June 21) and ended 4:14 UT on June 22. This fulfilled the requirement of a *prompt* observation (see below) and was long enough to allow for observations from 6.5 minutes to ∼5 hours after the burst. The results of these observations are presented in §4.5.3.

Depending on whether the burst position is *observable* (in other words, whether the observational constraints are met) and the redshifts[8] of the GRBs reported through GCN circulars, we start observing the burst positions up to ∼24 hours after the burst time. A typical GRB observation consists of 120 minutes' observations (four observation *runs*) in *wobble* mode.

Operationally, GRB observations with H.E.S.S. fall into two categories:

- If a burst alert arrives up to one hour before or during dark time at the H.E.S.S. site and the distributed burst position can be observed immediately at Z.A.s smaller than $\lesssim 45°$ for at least ∼30 minutes, this alert is called a *prompt GRB alert*. In this case, an alerting voice is played in the control room on site and a pop-up window appears on the screen of the main terminal used by the shift crew. Weather permitting, a prompt GRB alert is followed by a *prompt GRB observation* carried out by the shift crew. The shift crew is authorized and recommend to immediately commence *prompt GRB observations* to reduce time delay. They then inform the GRB *contact person* that prompt observations have been commenced. The GRB contact person can authorize a halt to the prompt observation if desired, e.g. in the case where a high redshift of the GRB is reported. Prompt GRB observations prevail other observations, i.e. they have the highest priority over all other observational targets

---

[8]the redshift criteria are set such that a long delayed observation time with respect to the burst time is more tolerable for a GRB with a lower redshift than one with a higher redshift or one without reported redshift

except for specific observations defined *in advance* by the Observation Committee. The position is observed until the end of darkness or Z.A.> 45° whichever is met first. The delayed time of these observations is *on average* about 5 minutes after the burst.

- If a burst alert meets the observation criteria but is not a *prompt GRB alert*, it is called an *afterglow GRB alert*. In other words, the burst position can only be observed at later times. *Afterglow GRB observations* have the second priority after multi-wavelength observation campaigns which are communicated by the Observation Committee secretary at the beginning of every month. Normally, the alert case is to be discussed in the GRB team in the day and a decision as to observe the burst position or not is then made before darkness[9]. If an observation is desired, the shift crew is asked to carry out an *afterglow GRB observation* in the available observational time window. The delayed time of these observations is *on average* about 10 hours after the burst.

Occasionally, an alert might turn out to be a false GRB alert, i.e. it is known after a ground-based analysis that the satellite trigger was not caused by a GRB but had been mistakenly classified as a GRB trigger. This alert is then *retracted*. For *Swift* alerts, the ratio of the number of genuine GRB alerts to that of false alerts is around 10%.

From the beginning of 2005 until the end of 2007, the observation strategy is such that a GRB position is observed as soon as its Z.A. is smaller than ∼45° for at least half an hour over the period of 24 hours after the burst, unless there are indications that the redshift of the GRB is larger than two[10]. In that case, no observation is taken. On the other hand, if the redshift of the GRB is believed to be less than 0.5, a >2-hour exposure is obtained.

A quick analysis is running on site during observations to inform the shift crew about any strong signal in realtime. This has been proved to be crucial in the observations of the giant flares of PKS2155-204 during July 2006. If this analysis indicates that a signal is detected at a $\geq +3$ statistical significance level within the error box of the GRB position, further observations on the same and/or following nights are carried out. No such follow-up observation has been taken by the end of 2008.

An unexpected occasion

The observations of GRB 060602B was by itself an interesting story. It also demonstrates how the observation strategy described is handled in real life. I was fortunate enough to be able to participate in the process. This burst happened at the instant when the GRB 060602B position was only 5° from the local zenith of the H.E.S.S. telescopes. At the same time, H.E.S.S. was used to observe a region near to the Galactic Center. While the first GCN notice associated with this burst did not suggest observations (thus no

---

[9]Occasionally, no clear decision can be made before darkness. In this case, the GRB *contact person* has the sole authority at night

[10]This strategy was revised in 2008, such that the available (or the lack of) redshift information of the GRB is used to set an upper limit on the time delay of the start observation time: 24,12,6,4 hours for a redshift (z) of $\leq 0.1, \leq 0.3, \leq 1.0$, unknown, respectively. A GRB with $z \geq 1$ is not observed.

scheduled *prompt* observations were carried out), and the first observation targeted on the burst position was only taken around 1.5 hours later, it turned out that the burst position (which is only $\sim 1.5°$ from the Galactic Center) had already been in the FoV of the H.E.S.S. when it occurred! This was not recognized until about a month later. A full description of the observations, analysis techniques, and results is given in Section 6. Here I show the observations of the burst from an operational point of view. What happened in the night of June 2–3, 2006 is described in the following time line (all times give in UT unless otherwise specified):

June 2, 23:54:33.9 *Swift*/BAT was triggered by GRB 060602B;

June 3, 00:08:57 GCN notice of this burst arrived in Namibia after some delay, however it did not pass the criteria. As a result, no action, i.e. *prompt* observation, was taken;

June 3, 00:53:33 An official announcement/confirmation of the GRB from *Swift* team (Schady et al., 2006) was sent out. Around ten minutes later, I noticed the announcement, and being a deputy of the GRB *contact person*, I decided to call the shift crew at 3 a.m. (European time) from my bedroom in Heidelberg, Germany!

June 3, 01:22 The first *scheduled* observation run on the burst position was started;

June 3, 01:22 – 03:33 Five observation runs in *wobble* mode were taken, of which one had a hardware failure (Tracking Error);

June 3, 02:04 An email about the GRB observations being taken was drafted to the GRB team mailing list;

June 3, daytime The shift crew found a 5-σ signal at the position of the Galactic Center, but no signal at the GRB position. Therefore, no follow-up observation was scheduled.

3.3   An estimate of expected number of observed GRBs

During the years 2005–2007, the total number of GRBs triggering *Swift*/BAT is 299 — thus about a hundred per year[11], which forms the majority of all GRBs detected during these years. The expected number of observed GRBs per year is estimated as follows.

expected number of GRB prompt observations

Among all *Swift* GRBs, only a fraction of bursts could immediately be pointed at a Z.A. of $\leq 45°$. By simple geometry, this fraction is

$$F_{\text{Z.A.}} = \frac{\int_0^{\pi/4} \sin\phi \, d\phi \ \int_0^{2\pi} d\theta}{4\pi} = \frac{2\pi \left(1 - \frac{1}{\sqrt{2}}\right)}{4\pi} \approx 0.146$$

---

[11]http://swift.gsfc.nasa.gov/docs/swift/archive/grb_table/grb_stats.php

where ϕ is the Z.A. and θ the azimuth angle. For simplicity, the requirement that the burst position is within Z.A. of $<45°$ for at least about half an hour — the duration of a normal H.E.S.S. observation run — is neglected. This requirement is introduced to make sure that the data quality of the observations can be addressed satisfactorily (described in more details in Section 3.5). At times, it may be desirable that an half-an-hour observation run would be taken even if part of the run is carried out at Z.A. of $\gtrsim 45°$.

Even if the burst position is at a Z.A. of $<45°$ when the burst occurs, it is obvious that it has to happen during H.E.S.S. dark time, in order that the position can be observed immediately. In this regard, another fraction — H.E.S.S. dark time fraction, F_{darkness} — enters. H.E.S.S. dark time is the union of the astronomical darkness time (i.e. without twilight) *and* the time when the moon is below the horizon. For simplicity, a geographical location at the equator is used. This gives $F_{\mathrm{darkness}} = 0.198$. For any location not on the equator (e.g. a latitude of $23°16'18''$ S for H.E.S.S.), this fraction is smaller because the twilight time span is the shortest at the equator.

Based on the above estimate, the expected number of GRBs per year which can be followed immediately is $100 \times 0.146 \times 0.198 \approx 2.9$.

expected number of GRB afterglow observations

To observe a burst position within the 24 hours for at least half an hour after the burst, the position must be of a declination, δ, between (approximately) $17°$ N and $62°$ S. The fraction of bursts within this declination band is

$$F_{\mathrm{dec}} = \frac{1}{4\pi} \left(\int_{73°}^{90°} \sin\theta_{\mathrm{N}}\, d\theta_{\mathrm{N}} \int_{0}^{360°} d\alpha + \int_{28°}^{90°} \sin\theta_{\mathrm{S}}\, d\theta_{\mathrm{S}} \int_{0}^{360°} d\alpha \right) \approx 0.59$$

where θ_{N} (θ_{S}) represents the angle between the burst position and the north (south) pole and α the right ascension.

Among those bursts with $\delta \leq +17°$ and $\delta \geq -62°$, the fraction of bursts with a position observable during H.E.S.S. darkness time in the following 24 hours can be estimated to be about 0.58, again taking the assumption that the instrument is located at the equator[12]. Based on the above estimate, the expected number of GRBs per year which can be followed for at least half an hour in 24 hours after the burst is approximately $100 \times 0.59 \times 0.58 \approx 34$.

3.4 Observed sample of GRBs

The sample of GRBs *observed* with H.E.S.S. during the period between March 2003 and August 2008 is shown in Table 3.2. In total 34 GRBs were observed, with a total of ~ 47 observation hours. A split-up of the observation hours is shown in Figure 3.5. As a result of the observing strategy described in Section 3.2.3, most of the GRB observations are taken during the *afterglow* phase.

---

[12] Given the relative positions of Sun and moon at any moment, one can calculate the fraction of the whole sky where the sky position could be observed in *H.E.S.S. darktime* for at least half an hour
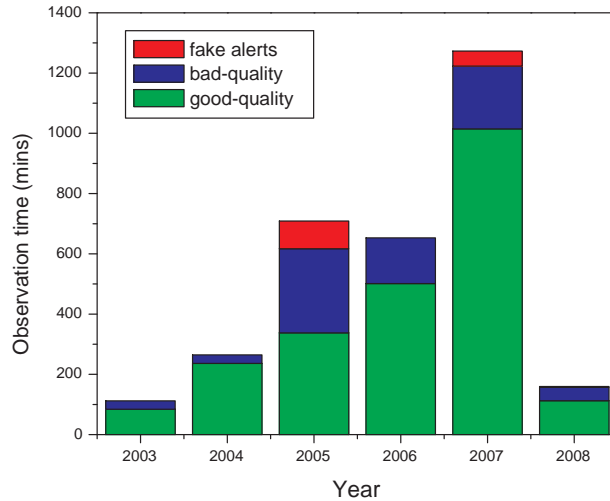
Figure 3.5: Observation time spent on the GRB observation program. Data passing quality cuts (good-quality) are denoted in green, those not passing quality cuts (bad-quality) are in blue, and those data spent on fake alerts (i.e. non-GRBs) are in red.

Among the GRBs with good-quality[13] data, there are nine GRBs with reported redshifts. While the mean redshift is 1.30, the median is located at $z = 0.716$. The redshift distribution is shown in Figure 3.6. If the two GRBs with a pseudo-redshift, pz, GRB 041211B (pz= 3.29 ± 0.9) and GRB 050209 (pz= 2.93 ± 1.6; Pélangeon & Atteia, 2008), are also included, the mean redshift becomes 1.63 and the median is at $z = 1.56$.

To estimate the redshifts of those H.E.S.S.-observed GRBs without reported redshift is scientifically very interesting because it would help to disentangle the EBL absorption effect and would probe the intrinsic limits on VHE luminosity of the GRB sample. It is, however, a difficult task. One may assume that these unknown redshifts are similar to those known redshifts. In this case, one would expect $\sim$40% of them to have $z < 0.5$. However, it is probably not the case, since redshift determination biases do exist (e.g. Fiore et al., 2007). According to the analysis of Coward et al. (2008) who assume the intrinsic GRB populations follow the star formation history, GRBs without reported redshift is more likely to locate at $1.5 \lesssim z \lesssim 2$. The main reason is that there exists a 'redshift desert' centered at $z \sim 1.6$ where redshift determination is extremely difficult as a result of no strong emission/absorption line feature in the optical band. On the other hand, one would expect a large number of GRBs to occur at this range because of the high star formation rate (if GRBs trace star formation) and a large geometrical volume.

---

[13]The data-quality criteria are discussed in Section 3.5.
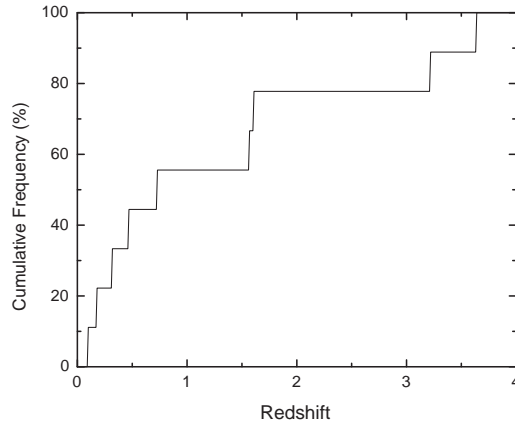
Figure 3.6: Cumulative frequency distribution of redshifts for the observed 9 GRBs with a reported redshift.

Table 3.2: List of observed GRBs from 2003–2008. The bursts up to 2007 with (*) are those with good data and thus are analyzed and presented in Section 4. The results of GRB 060602B (#) are presented in §6.

2003	2004	2005	2006	2007	2008
GRB 030821*	GRB 041211B*	GRB 050922C	GRB 061121	GRB 071003*	GRB 080804
GRB 030329*	GRB 041006*	GRB 050801*	GRB 061110A	GRB 070920B	GRB 080413A
	GRB 040425	GRB 050726*	GRB 060927	GRB 070808*	
		GRB 050607	GRB 060728	GRB 070805	
		GRB 050509C*	GRB 060602B#	GRB 070724A*	
		GRB 050209*	GRB 060526*	GRB 070721B*	
			GRB 060505*	GRB 070721A*	
			GRB 060403*	GRB 070621*	
				GRB 070612B*	
				GRB 070429B	
				GRB 070429A*	
				GRB 070419B*	
				GRB 070209*	

Table 3.3: List of GRBs with *prompt observations* using H.E.S.S.

Name	T_{start} (s)	exposure time (min)	live time (min)	redshift
GRB 050801	899	28.2	28.2	1.56
GRB 070429B	545	28.2	0	0.904
GRB 070621	391	234.6	234.6	. . .
GRB 070805	350	53.6	0	. . .
GRB 080413A	481	44.3	0	2.43
GRB 080804	305	112.4	112.4	2.20

Table 3.4: List of GRBs whose positions fell serendipitously into the H.E.S.S. field of view within 10 days after the burst

GRB	Satellite	Trigger number	Energy Band (keV)	Fluence[a] (10^{-8} erg cm^{-2})	T_{90}^{a} (s)	T_{delay}^{b}	exposure (h)
060602B	*Swift*	213190	15–150	18	9	0	$>10^{c}$
050701	*Swift*	143708	15–350	190	40	4.3 d	0.4
040812	INTEGRAL	1901	20–200	5^{d}	20	6.6 d	0^{e}
030725[f]	HETE-II	2779	30–400	2000	180	12.1 h	1.0

[a]Fluence and T_{90} data are taken from GCN Circulars.

[b]Time delay of the instant when the burst position fell into the H.E.S.S. FoV since the burst

[c]This burst was observed for 10 hours during the same night of the burst (some observations were taken before and during the burst) and the following three nights. See Chapter 6 for details.

[d]peak flux in 10^{-8} erg cm^{-2}s^{-1}

[e]bad weather, large offset

[f]pseudo-z of 0.89 ± 0.2 is obtained (Pélangeon & Atteia, 2008).

GRBs with prompt observations

There are six GRBs with *prompt observations*. They were followed up within ∼10 minutes after the trigger. The time T_{start} between the trigger and start time of the first observation, exposure time, live time of observations (after rejection of observation runs with non-optimal data quality, c.f. Section 3.5), as well as the redshift (if known) are listed in Table 3.3. The data of GRB 050801 and GRB 070621 pass data-quality cuts, and are presented in Chapter 4.

GRBs with afterglow observations

There are 34 GRBs with *afterglow observations*, the delayed starting time of them is ≳10 minutes with respect to the GRB trigger. A majority of the data pass data-quality cuts and are presented in Chapter 4. On the other hand, there are several GRB positions which fell serendipitously into the H.E.S.S. FoV after the burst (Table 3.4). They are included here since the temporal profile of any VHE emission of GRBs is not well understood. No signal of VHE emission was found.

3.5   A study of the data quality

The expected number of observable GRBs during the period 2005–2007 is $\sim$100. This is larger than the actual number of GRBs with prompt and afterglow observations made during the same period, as given in Table 3.2. Possible reasons for the discrepancy are: high reported redshifts of some observable GRBs, bad weather, occasional hardware problems of the system, and internet downtime at the H.E.S.S. site. While bad weather and hardware problems prohibit actual observations or affect the data taking, internet downtime prevents the arrival of GCN notices.

As seen in Table 3.3, there are observing data from *prompt GRB observations* which do not pass the data quality selection criteria. The same applies for *afterglow GRB observations*. Since these data are potentially useful, it is worth looking into some details of what these criteria are and whether these data can be used with correction. LeBohec & Holder (2003) discuss an example of such corrections, utilizing the throughput factor, which describes the *relative* efficiency of an IACT to record air shower events for one observation time compared to others.

3.5.1   System trigger rate as a tool in data quality selection criteria

Data quality selection criteria are applied to observation runs to reject those under non-optimal observing conditions. They are meant to ensure that the data used are suitable for spectral and temporal studies.

A good hardware status is one such criterium. It is composed of the requirements of a good tracking system (i.e. a high precision of the pointing positions of the telescopes) and that the number of turned-off PMTs is reasonably small (Section 3.2 in Aharonian et al., 2006b).

The atmosphere, which is essentially part of the detecting system, is another source of non-optimal observing conditions. The presence of stationary or moving clouds, a large amount of dust in the atmosphere, or hazy atmosphere, can lead to the absorption of Cherenkov light and/or fluctuations in the system trigger efficiency. A quantitative relation between these various atmospheric conditions and their combined effect in the air showers (and thus the resulting Cherenkov images) is not yet fully understood.

Three measures are used to estimate the quality of H.E.S.S. data: the mean system trigger rate of the run (of which a vast majority is caused by cosmic ray events), the relative change of the trigger rate over the run (δ_1)[14], and the r.m.s. variation (δ_2) of the trigger rate over the best-fit straight line of the rate[15]. Runs of which (i) the mean trigger rate is less than 70% of the predicted *optimal* value (as discussed below), (ii) $|\delta_1| > \tan(30°)$, or (iii) $\delta_2 > 10\%$, are rejected. These three quality cuts are routinely used to differentiate a non-optimal run from a good run.

---

[14]For an observation at a Z.A. $\gtrsim 20°$, the absolute trigger rate may increase (or decrease) substantially over the run duration due to the change in Z.A. A cut is introduced to reject runs with a too large absolute value of δ_1.

[15]In this sense, δ_2 provides an estimate of real fluctuations over the general trend of change in system rate.
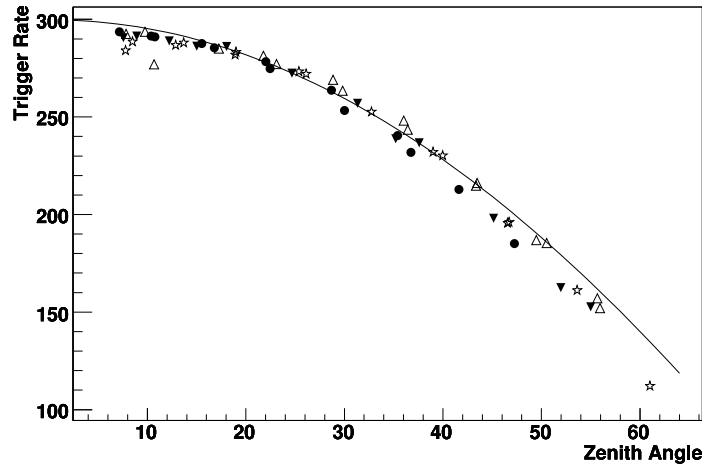
Figure 3.7: System trigger rate versus Z.A. for observations taken during a campaign of PKS 2155-304 in 2004. Each data point represents an observation run. Runs taken within the same night are denoted as the same symbols. A functional form derived from another set of data (solid line) is used to correct for zenith angle dependency.

The mean system trigger rate of an observation run depends on the Z.A., which is nominally confined to Z.A.$\lesssim 45°$ for observations of GRBs. Due to the unpredictable and fast-fading nature of GRBs, observations at Z.A. as large as 60°–70° is expedient for those extremely bright and/or nearby GRBs (e.g. GRB 030329). Therefore, understanding observations at a wide range of Z.A. is desirable. Figure 3.7 shows the Z.A. dependence of system trigger rate. The atmospheric column depth of the air-showers at large Z.A. are substantially greater, resulting in more absorption and scattering of the Cherenkov photons created in the air showers, and therefore a lower system trigger rate. Derived from a certain set of data taken in clear nights, a correcting factor, $f(\theta_{za})$, of the trigger rate was obtained:

$$f(\theta_{za}) = \left(-0.2566 + 1.564 \cos(\theta_{za}) - 0.307 \cos(\theta_{za})^2 \right)^{-1} \qquad (3.1)$$

which is shown as a solid curve in Figure 3.7 (normalized for this particular set of data points shown). This factor is then multiplied by the trigger rate to obtain a Z.A.-corrected trigger rate of each run, despite some discrepancies at smallest and largest Z.A. for these data.

Furthermore, the Z.A.-corrected system trigger rate shows substantial changes over the H.E.S.S. operational years. It is demonstrated in Figure 3.8, which shows the system trigger rate during the years from 2004 to 2007. The periodic behavior composes of two parts:

1. gentle decrease of the rate over periods of months, e.g., due to a decrease of mirror efficiency, quantum efficiency of the PM tubes, and reflectivity of the Winston cones;

2. abrupt rise of the rate due to re-adjustments of the high voltage of the PMTs.

The solid line shows the data-quality cut on the system rate, which takes this periodic behavior into account.
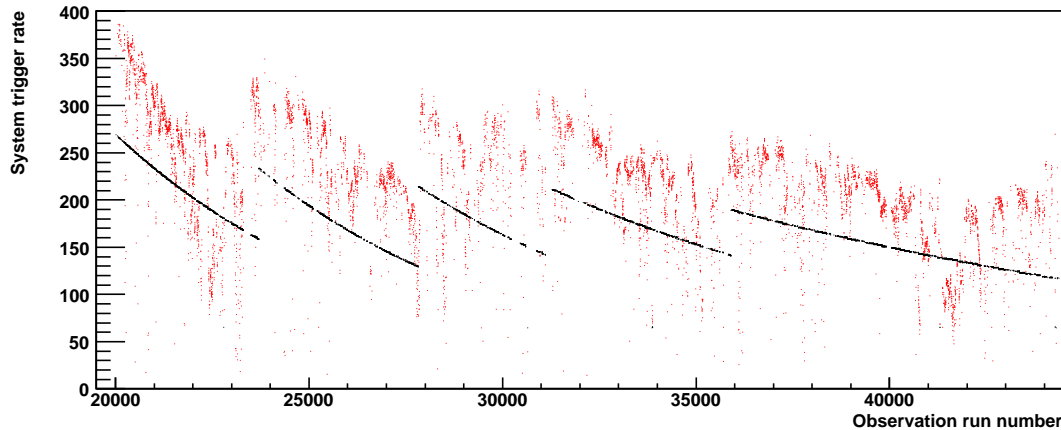
Figure 3.8: The system trigger rate (Z.A.-corrected) over the years 2004–2007. The black lines represent the data-quality cut on the observation run based on the its system trigger rate.

After correcting for the long-term change of the system rate by introducing a normalized factor for each run, the system rate is compared with another data quality cut parameter, δ_2. This is shown in Figure 3.9 for data taken around May 2004 and in August/September 2004. The data points for May data is predominantly clustered in the region of high rate and small δ_2 (therefore passing these cuts), consistent with the good weather conditions during this period. In contrast, there is a larger scatter in the system rate in the August/September data. Therefore many runs do not pass the data quality cuts of the system rate. The scatter of δ_2 is very similar in both cases, which may indicate that the runs with lower system rate may not be so bad at all. However, a further study is needed in order that these low-rate runs can be used in analysis. This may be a characteristic effect of a hazy atmosphere which often occurs during the season around August and September.

3.5.2 Sub-run data quality

The above discussion shows that there is a possibility to recover those *whole* runs with non-optimal data quality to be used in flux or upper limit calculations. However, an observation run with a reasonably stable system rate may contain a sudden change in the system rate for a short period of time. This may be caused by, e.g., a cloud coming in and out of the camera FoV. Because of this sudden change, this run is likely rejected by the data quality criteria, because of a large δ. Figure 3.10 shows the system trigger rate as a function of time for two 28-minute runs: one with a stable system trigger rate close to the predicted level for this Z.A., and the other exhibiting variability due to the presence of clouds. It is therefore possible to recover the unaffected period of the run based on the knowledge of the time evolution of the system rate (c.f. Figure 3.10).
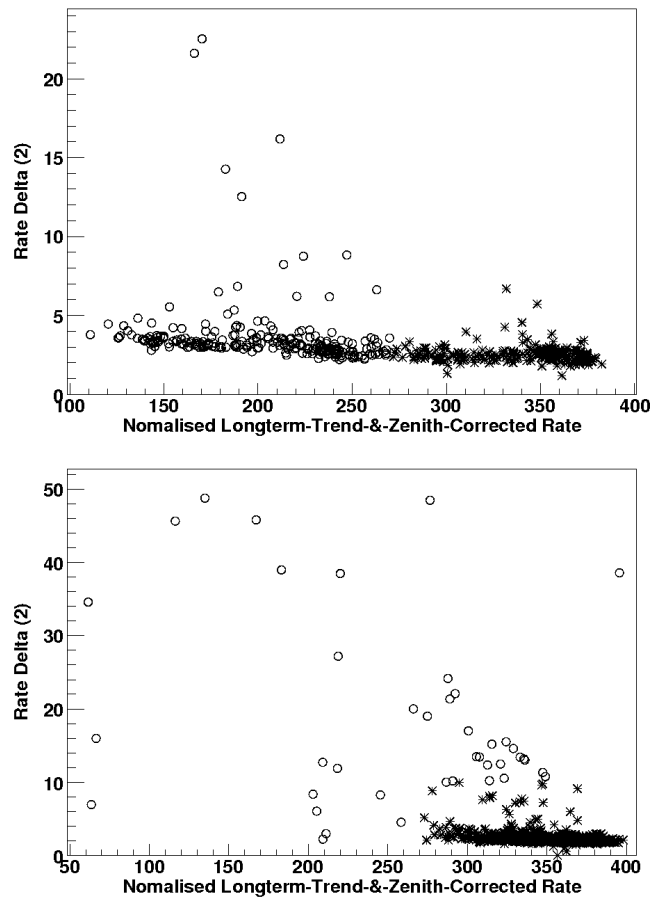
Figure 3.9: Plots of δ_2 against system trigger rate (Z.A. and long-term trigger-rate change effects corrected) for data taken around May 2004 (*left panel*) and during the period August to September 2004 (*right panel*). Data passing the run quality cuts (i) and (iii) are shown in stars, while those do not are shown in circles.
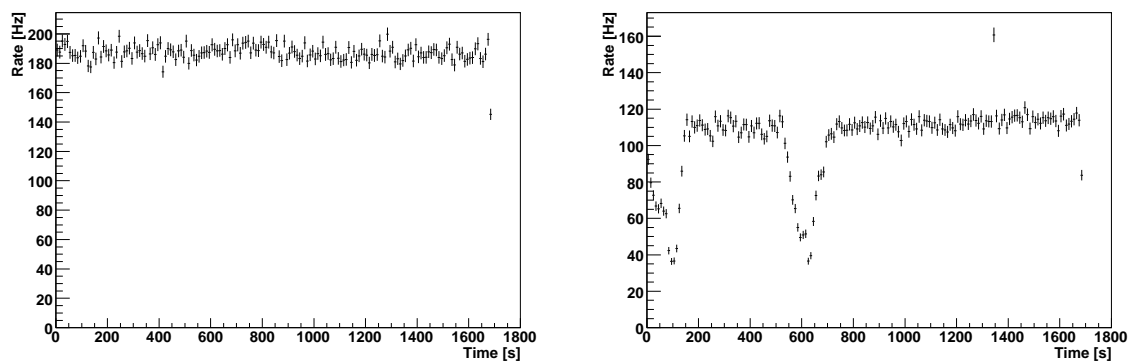
Figure 3.10: System trigger rate as a function of time for two 28-minute runs. *Left panel*: Run #39874 with a stable system trigger rate. *Right panel*: Run #42644 exhibiting variability in its system rate, due to the presence of clouds.

Chapter 4

H.E.S.S. observations of γ-ray bursts in 2003–2007

Observations of GRBs have remained high in priority since the start of the H.E.S.S. experiment in 2003. The first observation (of GRB 030329) was taken before the completeness of the whole array composed of four telescopes. The observing program of GRBs as described in Chapter 3 led to H.E.S.S. observations of a total of 32 GRBs. When I joined the H.E.S.S. collaboration in August 2005, 10 GRB observations had been performed. I have analyzed all GRB data and results are presented in this chapter, which was submitted to *Astronomy and Astrophysics* by the H.E.S.S. collaboration as a paper, of which I am the corresponding author.

Abstract Very-high-energy (VHE; $\gtrsim$100 GeV) γ-rays are expected from γ-ray bursts (GRBs) in some scenarios. Exploring this photon energy regime is necessary to understand the energetics and properties of GRBs. GRBs have been one of the prime targets for the H.E.S.S. experiment, which makes use of four Imaging Atmospheric Cherenkov Telescopes (IACTs) to detect VHE γ-rays. Dedicated observations of $\sim$30 GRB positions were made in the years 2003–2007 and a search for VHE γ-ray counterparts of these GRBs was made. Depending on the visibility and observing conditions, the observations mostly start minutes to hours after the burst and last typically two hours. No evidence of a VHE signal was found in observations of any individual GRB, nor from stacking data from subsets of GRBs with higher expected VHE flux according to a model-independent ranking scheme. Upper limits for the VHE γ-ray flux from the GRB positions were derived. For those GRBs with measured redshifts, differential upper limits at the energy threshold after correcting for absorption due to extra-galactic background light are also presented.

4.1 Introduction

Gamma-ray bursts (GRBs) are the most energetic events in the γ-ray regime. First detected in late 1960s (Klebesadel et al., 1973), GRBs remained mysterious for three decades. Breakthroughs in understanding GRBs came only after the discovery of longer-wavelength afterglows with the launch of *BeppoSAX* in 1997 (van Paradijs et al., 2000). Multi-wavelength (MWL) observations have proved to be crucial in our understanding of GRBs, and provide valuable information about their physical properties. These MWL afterglow observations are generally explained by synchrotron emission from shocked electrons in the relativistic *fireball* model (Piran, 1999; Zhang & Mészáros, 2004).

In the framework of the relativistic *fireball* model, photons with energies up to $\sim$10 TeV or higher are expected from the GRB afterglow phase (Zhang & Mészáros, 2004; Fan & Piran, 2008). Possible leptonic radiation mechanisms include forward-shocked electrons up-scattering self-emitted synchrotron photons (SSC processes; Dermer et al., 2000; Zhang & Mészáros, 2001b; Fan et al., 2008) or photons from other shocked regions (Wang et al., 2001). Physical parameters, such as the ambient density of the surrounding material (n), magnetic field equipartition fraction (ϵ_B), and bulk Lorentz factor (Γ_{bulk}) of the outflow, may be constrained by observations at these energies (Wang et al., 2001; Pe'er & Waxman, 2005). The origin of the plateau phase in many of the *Swift*/XRT light curves is still not clear (Zhang et al., 2006). Observations of GRBs at energies >10 GeV may test some of the ideas which have been suggested to explain the X-ray observations (Fan et al., 2008).

A possible additional contribution to VHE emission relates to the X-ray flare phenomenon. X-ray flares are found in more than 50% of the *Swift* GRBs during the afterglow phase (Chincarini et al., 2007). The energy fluence of some of them (e.g. GRB 050502B) is comparable to that of the prompt emission. Most of them are clustered at $\sim10^2$–10^3s after the GRB (see Figure 2 in Chincarini et al., 2007), while late X-ray flares (>10^4s) are also observed; when these happen they can cause an increase in the X-ray flux of an order of magnitude or more over the power-law temporal decay (Curran et al., 2008). The cause of X-ray flares is still a subject of debate, but corresponding VHE γ-ray flares from inverse-Compton (IC) processes are predicted (Wang et al., 2006; Galli & Piro, 2007; Fan et al., 2008). The accompanying external-Compton flare may be weak if the flare originated behind the external shock, e.g. from prolonged central engine activity (Fan et al., 2008). However, in the external shock model, the expected SSC flare at GeV energies is very strong and can be readily detected using a VHE instrument with an energy threshold of $\sim$100 GeV (Galli & Piro, 2008), such as the H.E.S.S. array, for a typical GRB at z$\sim$1. Therefore, VHE γ-ray data taken during an X-ray flare may help to discriminate the internal/external shock origin of the X-ray flares, and may be used as a diagnostic tool for the late central engine activity.

Waxman & Bahcall (2000) and Murase et al. (2008) suggest that GRBs may be sources of Ultra-high-energy cosmic rays (UHECRs). In this case, π-decays from proton-γ interaction may generate VHE emission. The VHE γ-ray emission produced from such a hadronic component is generally expected to decay more slowly than the leptonic sub-MeV radiation (Böttcher & Dermer, 1998). Dermer (2007) suggested a combined leptonic/hadronic scenario to explain the rapidly-decaying phase and plateau phase seen in many of the *Swift*/XRT light curves. This model can be tested with VHE observations taken minutes

to hours after the burst.

Most searches for VHE γ-rays from GRBs have obtained negative results (Connaughton et al., 1997; Atkins et al., 2005). There may be indications of excess photon events from some observations, but these results are not conclusive (Amenomori et al., 1996; Padilla et al., 1998; Atkins et al., 2000; Poirier et al., 2003). Currently, the most sensitive detectors in the VHE γ-ray regime are IACTs. Horan et al. (2007) presented upper limits from 7 GRBs observed with the Whipple Telescope during the pre-*Swift* era. Upper limits for 9 GRBs with redshifts that were either unknown or >3.5 were also reported by the MAGIC collaboration (Albert et al., 2007b). In general, these limits do not violate a power-law extrapolation of the keV spectra obtained with satellite-based instruments. However, most GRBs are now believed to originate at cosmological distances, therefore absorption of VHE γ-rays by the EBL (Nikishov, 1962) must be considered when interpreting these limits.

In this paper, observations of 21 γ-ray bursts made with H.E.S.S. during the years 2003–2007 are reported. They represent the largest sample of GRB afterglow observations made by an IACT array and result in the most stringent upper limits obtained in the VHE band. The prompt phase of GRB 060602B was observed serendipitously with H.E.S.S. The results of observations before, during, and after this burst are presented elsewhere (Aharonian et al., 2009).

4.2   The H.E.S.S. Experiment and GRB Observation Strategy

The H.E.S.S. array[1] is a system of four 13m-diameter IACTs located at 1 800 m above sea level in the Khomas Highland of Namibia ($23°16'18''$ S, $16°30'00''$ E). Each of the four telescopes is placed at a corner of a square with a side length of 120 m. This configuration was optimized for maximum sensitivity to $\sim$100 GeV photons. The effective collection area increases from $\sim 10^3 \mathrm{m}^2$ at 100 GeV to more than $10^5 \mathrm{m}^2$ at 1 TeV for observations at a zenith angle (Z.A.) of 20°. The system has a point source sensitivity above 100 GeV of $\sim 1.4 \times 10^{-11} \mathrm{erg\, cm}^{-2}\,\mathrm{s}^{-1}$ (3.5% of the flux from the Crab nebula) for a 5σ detection in a 2 h observation. Each H.E.S.S. camera consists of 960 photomultiplier tubes (PMTs), which in total provide a field of view (FoV) of $\sim$5°. This relatively large FoV allows for the simultaneous determination of the background events from off-source positions, so that no dedicated off run is needed (Aharonian et al., 2006b). The slew rate of the array is $\sim$100° per minute, enabling it to point to any sky position within $\sim$2 minutes. The H.E.S.S. array is currently the only IACT array in the Southern Hemisphere used for an active GRB observing programme[2].

The trigger system of the H.E.S.S. array is described in Funk et al. (2004). The stereoscopic technique is used, i.e. a coincidence of at least two telescopes triggering within a window of (normally) 80 nanoseconds is required. This largely rejects background events caused by local muons which trigger only a single telescope.

---

[1] http://www.mpi-hd.mpg.de/hfm/HESS/HESS.html
[2] http://www.lsw.uni-heidelberg.de/projects/hess/HESS/grbs.phtml

The observations reported here were obtained over the period March 2003 to October 2007. The observations of two GRBs in 2003 were made using two telescopes while the system was under construction. Before July 2003, each of the two telescopes took data separately. Stereo analysis was then performed on the data which requires coincidence of events to be determined offline using GPS time stamps. After the installation of the central trigger system in 2003 July, the stereo multiplicity requirement was determined on-line. All observations since 2004 have made use of the completed four-telescope array and the stereo technique (Aharonian et al., 2006b).

Most of the data were taken in 28 minute runs using *wobble* mode, i.e. the GRB position is placed at an offset, θ_{offset}, of $\pm 0°\!.5$ or $0°\!.7$ (in R.A. and Decl.) relative to the centre of the camera FoV during observations.

On-board GRB triggers distributed by the *Swift* satellite, as well as triggers from *INTEGRAL* and *HETE-II* confirmed by ground-based analysis, are followed by H.E.S.S. observations. Upon the reception of a GCN[3] notice from one of these satellites (with appropriate indications that the source is a genuine GRB), the burst position is observed if Z.A.$\lesssim 45°$ (to ensure a reasonably low energy threshold) during H.E.S.S. dark time[4]. An automated program is running on site to keep the shift crew alerted of any new detected GRBs in real-time. Depending on the observational constraints and the measured redshifts of the GRBs reported through GCN circulars[5], observations of the burst positions are started up to ∼24 hours after the burst time, typically with an exposure time of ≈120 minutes in *wobble* mode. The remarkably nearby, bright GRB 030329 was an exceptional case. It was not observed until 11.5 days after the burst because of poor weather, which prohibited observation any earlier.

4.3   The GRB Observations

More than 30 GRBs were observed with H.E.S.S. during the period from March 2003 to October 2007. After applying a set of data-quality criteria which rejects observation runs with non-optimal weather conditions and hardware status, 21 GRB observations were selected for analysis and are described in this section.

4.3.1   Properties of the GRBs

For each burst, the observational properties as obtained from the triggering satellite are shown in Table 4.1. These include trigger number, energy band, fluence in that energy band and the duration of the burst (T_{90}). Whenever there were follow-up observations in the X-ray, optical or radio bands, whether a detection has occurred (denoted by a tick $\checkmark$) or not (denoted by a cross $\times$) is also shown. If no observation at a given wavelength was reported, a dot (.) is shown. The reported redshifts (z) of 9 GRBs are also presented, of which five are smaller than one. Two observed bursts, GRB 070209 and GRB 070724A,

---

[3]The Gamma ray bursts Coordinates Network, http://gcn.gsfc.nasa.gov/

[4]H.E.S.S. observations are taken in darkness and when the moon is below the horizon. The fraction of H.E.S.S. dark time is about 0.2

[5]http://gcn.gsfc.nasa.gov/gcn3_archive.html

are categorized as short GRBs (i.e. $T_{90} < 2$s) while the rest are long GRBs (i.e. $T_{90} > 2$s). The population of short GRBs has a redshift distribution (Berger et al., 2007) significantly smaller than that of the long GRBs (Jakobsson et al., 2006). Therefore, on average they are likely to suffer from a smaller level of EBL absorption.

X-ray flares were detected from three of the GRBs in the H.E.S.S. sample. They occurred at 273s after the burst for GRB 050726, 284s for GRB 050801, and 2.6×10^5s for GRB 070429A (Curran et al., 2008). Unfortunately, the flares occurred outside the time windows of the H.E.S.S. observations.

Table 4.1: Properties of GRBs observed with H.E.S.S. from March 2003 to October 2007.

GRB	Satellite	Trigger number	R.A.[a]	Decl.[a]	Error[a] ('')	Energy band (keV)	Fluence[b] ($10^{-8}\,\mathrm{erg\,cm^{-2}}$)	T_{90}[b] (s)	X[c]O[c]R[c]	z[d]	rank[e]
071003	*Swift*	292934	$20^h07^m24^s.25$	$+10°56'48''.8$	5.7	15–150	830	~150	√√√	1.604	5
070808	*Swift*	287260	$00^h27^m03^s.36$	$+01°10'34''.8$	1.9	15–150	120	~32	√√.		8
070724A	*Swift*	285948	$01^h51^m13^s.96$	$-18°35'40''.1$	2.2	15–150	3	~0.4	√××	0.457	20
070721B	*Swift*	285654	$02^h12^m32^s.95$	$-02°11'40''.6$	0.9	15–150	270	~340	√√×	3.626	13
070721A	*Swift*	285653	$00^h12^m39^s.24$	$-28°22'00''.6$	2.3	15–150	7.1	3.868	√√.		19
070621	*Swift*	282808	$21^h35^m10^s.14$	$-24°49'03''.1$	2	15–150	430	33	√×.		1
070612B	*Swift*	282073	$17^h26^m54^s.4$	$-08°45'08''.7$	4.7	15–150	168	13.5	√×.		15
070429A	*Swift*	277571	$19^h50^m48^s.8$	$-32°24'17''.9$	2.4	15–150	91	163.3	√√.		3
070419B	*Swift*	276212	$21^h02^m49^s.57$	$-31°15'49''.7$	3.5	15–150	736	236.4	√√.		7
070209	*Swift*	259803	$03^h04^m50^s$	$-47°22'30''$	168	15–150	2.2	0.09	××.	0.314?	21
060526	*Swift*	211957	$15^h31^m18^s.4$	$+00°17'11''.0$	6.8	15–150	126	298.2	√√.	3.21	10
060505	*Swift*	208654	$22^h07^m04^s.50$	$-27°49'57''.8$	4.7	15–150	94.4	~4	√√.	0.0889	17
060403	*Swift*	203755	$18^h49^m21^s.80$	$+08°19'45''.3$	5.5	15–150	135	30.1	√×.		16
050801	*Swift*	148522	$13^h36^m35^s$	$-21°55'41''$	1	15–150	31	19.4	√√×	1.56	2
050726	*Swift*	147788	$13^h20^m12^s.30$	$-32°03'50''.8$	6	15–150	194	49.9	√√.		14
050509C	*HETE-II*	H3751	$12^h52^m53^s.94$	$-44°50'04''.1$	1	2–30	60	25	√√√		18
050209	*HETE-II*	U11568	08^h26^m	$+19°41'$	420	30–400	200	46	.×.		12
041211B[f]	*HETE-II*	H3622	$06^h43^m12^s$	$+20°23'42''$	80	30–400	1000	>100	.×.		4
041006	*HETE-II*	H3570	$00^h54^m50^s.23$	$+01°14'04''.9$	0.1	30–400	713	~20	√√√	0.716	6
030821	*HETE-II*	H2814	21^h42^m	$-44°52$	[g]	30–400	280	23	...		9
030329	*HETE-II*	H2652	$10^h44^m49^s.96$	$+21°31'17''.44$	10^{-3}	30–400	10760	33	√√√	0.1687	11

[a]R.A., Decl., and the positional errors (90% containment) were taken from GCN Reports (http://gcn.gsfc.nasa.gov/report_archive.html) for GRB 070209 – GRB 071003 and GCN Circulars otherwise.

[b]Fluence and T_{90} data for GRB 050726 – GRB 070612B were taken from Sakamoto et al. (2008a) except that T_{90} of GRB 060505 was taken from Palmer et al. (2006a). Fluence and T_{90} data of GRB 030329 and GRB 030821 were taken from Sakamoto et al. (2005), and those of GRB 041006 from Shirasaki et al. (2008). Other data were taken from GCN Circulars and *HETE* pages (http://space.mit.edu/HETE/Bursts).

[c]X: X-ray, O: optical, R: radio; "√" indicates the detection of a counterpart, "×" a null detection, and "." that no measurement was reported in the corresponding energy range, from http://grad40.as.utexas.edu/grblog.php

[d]References for redshifts: GRB 071003 (Perley et al., 2008), GRB 070724A (Cucchiara et al., 2007), GRB 070721B (Malesani et al., 2007), GRB 070209 (Redshift of a candidate host galaxy, Berger & Fox, 2007), GRB 060526 (Berger & Gladders, 2006), GRB 060505 (Ofek et al., 2006), GRB 050801 (Redshift according to de Pasquale et al., 2007, based on afterglow modelling.), GRB 041006 (Soderberg et al., 2006a), GRB 030329 (Stanek et al., 2003)

[e]The relative expected VHE flux for each GRB is ranked according to the empirical scheme described in Sect. 4.3.3

[f]Although this burst was referred to as GRB 041211 in various GCN Circulars, the proper name GRB 041211B (e.g., in Pélangeon et al., 2006) should be used to distinguish it from another burst, GRB 041211A (=H3621) which occurred earlier on the same day (Pélangeon, A., private communication).

[g]The position error of this burst is large, see Figure 4.3

4.3.2   H.E.S.S. observations

For each burst, the start time, T_{start}, of the H.E.S.S. observations after the burst is shown in Table 4.2. Since an observing strategy to start observing the burst position up to $\sim$24 hours after the burst time is applied, the mean T_{start} is of the order of 10 hours. The (good-quality) exposure time of the observations using N_{tel} telescopes for each burst is included. The mean Z.A. of the observations is also presented.

4.3.3   The ranking scheme

As mentioned in the introduction, there is no lack of models predicting VHE emission from GRBs. However, the evolution of the possible VHE γ-ray emission with time is model-dependent. To give an empirical, model-independent estimate of the relative expected VHE flux of each GRB (which also depends on T_{start}), it is assumed that: (1) the relative VHE signal scales as the energy released in the prompt emission, taken as a typical energy measure of a GRB. Hence $F_{\text{VHE}} \propto F_{15-150\,\text{keV}}$ where $F_{15-150\,\text{keV}}$ is the fluence in the *Swift*/BAT band. For bursts not triggered by BAT, the measured fluence is extrapolated into this energy band; (2) the possible VHE signal fades as time goes on, as observed in longer wavelength (e.g. X-ray) data. In particular, the VHE flux follows the average decay of the X-ray flux and therefore $F_{\text{VHE}} \propto F_{15-150\,\text{keV}} \times t^{-1.3}$ where t denotes the time after the burst and 1.3 is the average X-ray afterglow late-time power-law decay index (Nousek et al., 2006). Since in most cases the exposure time of the observations is much shorter than T_{start} (the start time of the corresponding H.E.S.S. observations after the trigger), the expected flux at T_{start} can be used as a measure of the strength of the VHE signal, and therefore of the relative possibility of detecting a VHE signal from that GRB. By setting t to T_{start}, we have

$$F_{\text{VHE}} \propto F_{15-150\,\text{keV}} \times T_{\text{start}}^{-1.3}. \tag{4.1}$$

The rank of each GRB according to equation (4.1) is shown in the last column in Table 4.1. Note that redshift information (available for only a few GRBs), and thus the corresponding EBL absorption, is not taken into account in the ranking scheme.

4.4   Data Analysis

Calibration of data, event reconstruction and rejection of the cosmic-ray background (i.e. γ-ray event selection criteria) were performed as described in Aharonian et al. (2006b), which employs the techniques described by Hillas (1996).

Gamma-like events were then taken from a circular region (on-source) of radius θ_{cut} centered at the burst position given in Table 4.1. The background was estimated using the reflected-region background model as described in Berge et al. (2007), in which the number of background events in the on-source region (N_{off}) is estimated from N_{region} off-source regions located at the same θ_{offset} as the on-source region during the same observation. The number of γ-like events is given by $N_{\text{on}} - \alpha N_{\text{off}}$ where N_{on} is the total number of events detected in the on-source region and $\alpha = 1/N_{\text{region}}$ the normalization factor.

Independent analyses of various GRBs using different methods and background estimates (Berge et al., 2007) yielded consistent results.

4.4.1 Analysis technique

Two sets of analysis cuts were applied to search for a VHE γ-ray signal from observational data taken with three or four telescopes. These are 'standard' cuts (Aharonian et al., 2006b) and 'soft' cuts[6] (the latter have lower energy thresholds, as described in Aharonian et al., 2006a). For standard (soft) cuts, $\theta_{\mathrm{cut}} = 0.11°$ ($\theta_{\mathrm{cut}} = 0.14°$). While standard cuts are optimized for a source with a power-law spectrum of photon index $\Gamma = 2.6$, soft cuts are optimized for a source with a steep spectrum ($\Gamma = 5.0$), and have better sensitivity at lower energies. Since EBL absorption is less severe for lower energy photons, the soft-cut analysis is useful in searching for VHE γ-rays from GRBs which are at cosmological distances. For example, the photon indices of two blazars PKS 2005-489 (Aharonian et al., 2005) and PG 1553+113 (Aharonian et al., 2008a) were measured to be $\Gamma \gtrsim 4$.

An exception to this analysis scheme is GRB 030329. As the central trigger system had yet to be installed when this observation was made, a slightly different analysis technique was used. The description of the image and analysis cuts used for the data from GRB 030329 can be found in Aharonian et al. (2005). For GRB 030821, only the standard-cut analysis (for two-telescope data) was performed (see Sect. 4.5.4).

The positional error circle of most GRBs, with the exceptions of GRB 030821, GRB 050209, and GRB 070209, is small compared to the H.E.S.S. point spread function (PSF). The 68% γ-ray containment radius, θ_{68}, of the H.E.S.S. PSF can be as small as $\sim 3'$, depending on the Z.A. and θ_{offset} of the observations, and the analysis cuts applied. θ_{68} of the observations of GRB 050209 and GRB 070209 is about $9'$ using standard-cut analysis[7], slightly larger than the corresponding error circles. Therefore, point-source analyses were performed for all GRBs except GRB 030821, the error box of which is much larger than the H.E.S.S. PSF (see Sect. 4.5.4 for its treatment).

4.4.2 Energy threshold

The energy threshold, E_{th}, is conventionally defined as the peak in the differential γ-ray rate versus energy curve of a fictitious source with photon index Γ (Konopelko et al., 1999). This curve is a convolution of the effective area with the expected energy spectrum of the source as seen on Earth. Such energy thresholds, obtained by the standard-cut analysis and the soft-cut analysis for each GRB observation, are shown in Table 4.2, assuming $\Gamma = 2.6$. The energy threshold depends on the Z.A. of the observations and the analysis used. The larger the Z.A., the higher is the energy threshold. Moreover, soft-cut analysis gives a lower value of E_{th} than that of standard-cut analysis. Note that γ-ray photons with energies below E_{th} can be detected by the telescopes.

---

[6]'Soft' cuts were called 'spectrum' cuts in Aharonian et al. (2006a).

[7]θ_{68} is larger using soft-cut analysis

4.4.3   Optical efficiency of the instrument

The data presented were also corrected for the long-term changes in the optical efficiency of the instrument. The optical efficiency has decreased over a period of a few years. This has changed the effective area and energy threshold of the instrument. Specifically, the energy threshold has increased with time. Using images of local muons in the FoV, this effect in the calculation of flux upper limits is corrected (c.f. Aharonian et al., 2006b).

4.5   Results

No evidence of a significant excess of VHE γ-ray events from any of the GRB positions given in Table 4.1 during the period covered by the H.E.S.S. observations was found. The number of on-source (N_{on}) and off-source events (N_{off}), normalization factor (α), excess, and statistical significance[8] of the excess in standard deviations (σ) are given for each of the 20 GRBs in Table 4.2. The results for GRB 030821 are given in Sect. 4.5.4. Figure 4.1 shows the distribution of the significance obtained from the soft-cut analysis of the observations of each of the 20 GRBs. A Gaussian distribution with mean zero and standard deviation one, which is expected in the case of no detection, is shown for comparison. The distribution of the statistical significance is consistent with this Gaussian distribution. Thus no significant signal was found from any of the individual GRBs. A search for serendipitous source discoveries in the H.E.S.S. FoV during observations of the GRBs also resulted in no significant detection. The 99.9% confidence level (c.l.) flux upper limits (above E_{th}) have been calculated using the method of Feldman & Cousins (1998) for both standard cuts (assuming $\Gamma = 2.6$) and soft cuts (assuming $\Gamma = 5$), and are included in Table 4.2. The limits are as observed on Earth, i.e. the EBL absorption factor was not taken into account. The systematic error on a H.E.S.S. integral flux measurement is estimated to be $\sim$20%, and it was not included in the calculation of the upper limits.

For those GRBs with reported redshifts, the effect of the EBL on the H.E.S.S. limits can be estimated. Using the EBL model P0.45 described in Aharonian et al. (2006d), differential upper limits (again assuming $\Gamma = 5$) at the energy threshold were calculated from the integral upper limits obtained using soft-cut analysis. These upper limits, as well as those calculated without taking the EBL into account, are shown in Table 4.3.

---

[8]calculated by eq. (17) in Li & Ma (1983)

Table 4.2: H.E.S.S. observations of GRBs from March 2003 to October 2007. Analysis results using both standard cuts and soft cuts are presented. The GRBs are ranked according to the scheme described in Sect. 4.3.3. The nomenclature is described in the text.

GRB	T_{start} (min)	exposure (min)	N_{tel}	Z.A. (°)	Standard-cut analysis N_{ON}	N_{OFF}	α	excess	signi-ficance	E_{th} (GeV)	Flux ULs (cm^{-2} s^{-1})	Soft-cut analysis N_{ON}	N_{OFF}	α	excess	signi-ficance	E_{th} (GeV)	Flux ULs (cm^{-2} s^{-1})	Temporal analysis χ^2/d.o.f.	P(χ^2)
070621	6.5	234.6	4	16	204	2273	0.091	-2.6	-0.18	250	2.8×10^{-12}	731	5903	0.13	-6.9	-0.24	190	5.6×10^{-12}	19.2/28	0.89
050801	15.0	28.2	4	43	13	173	0.091	-2.7	-0.68	400	3.2×10^{-12}	46	442	0.13	-9.3	-1.2	310	1.6×10^{-11}	0.168/3	0.98
070429A	64	28.2	4	23	4	78	0.091	-3.1	-1.2	290	2.4×10^{-12}	20	203	0.13	-5.4	-1.0	220	1.0×10^{-11}	6.39/3	0.094
041211B[a]	567.1	14.2	3	64	9	87	0.11	-0.67	-0.21	1850	6.8×10^{-12}	27	236	0.17	-12	-1.9	1360	2.6×10^{-11}	14.6/14	0.40
	742.3	112.3	4	44	76	1247	0.063	-1.9	-0.21	380	3.7×10^{-12}	317	4353	0.083	-46	-2.4	280	1.8×10^{-11}		
071003[a]	623.3	56.2	4	35	16	272	0.10	-11	-2.2	390	1.0×10^{-12}	97	785	0.14	-15	-1.4	280	1.4×10^{-11}	32.3/12	0.0012
	691.1	56.2	4	41	25	204	0.10	4.6	0.93	480	5.6×10^{-12}	79	547	0.14	0.86	0.091	340	1.5×10^{-11}		
041006	626.1	81.9	4	27	80	770	0.10	3	0.32	200	1.1×10^{-11}	302	1974	0.14	20	1.1	150	6.8×10^{-11}	8.89/9	0.45
070419B	907	56.4	4	47	28	391	0.091	-7.5	-1.3	700	2.4×10^{-12}	121	1069	0.13	-13	-1.0	520	7.5×10^{-12}	11.9/6	0.064
070808	306.2	112.8	4	34	49	659	0.091	-11	-1.4	310	3.2×10^{-12}	209	1733	0.13	-7.6	-0.49	260	7.5×10^{-12}	15.8/12	0.20
060526	284.2	112.8	4	25	93	1068	0.10	-13.8	-1.3	280	2.9×10^{-12}	492	3711	0.14	-38	-1.6	220	9.2×10^{-12}	19.8/12	0.072
030329[b]	16493.5	28.0	2	60	4	26	0.14	0.27	0.13	1360	2.6×10^{-12}					[c]			5.93/3	0.12
050209	1208.5	168.6	4	48	104	1096	0.11	-18	-1.6	480	4.4×10^{-12}	528	4204	0.14	-73	-2.8	340	1.5×10^{-11}	36.3/18	0.0065
070721B	925.7	103.8	4	40	59	984	0.063	-2.5	-0.31	440	1.4×10^{-12}	237	2676	0.083	14	0.89	320	8.8×10^{-12}	15.5/11	0.16
050726	772.7	112.8	4	40	107	1031	0.083	21	2.1	320	7.1×10^{-12}	333	2619	0.11	42	2.3	260	3.4×10^{-11}	14.7/12	0.26
070612B	901.7	112.8	4	18	104	1190	0.091	-4.2	-0.39	240	4.1×10^{-12}	415	3233	0.13	11	0.51	180	1.5×10^{-11}	4.87/12	0.96
060403	820.4	52.8	4	39	33	252	0.091	10	1.9	440	4.8×10^{-12}	128	875	0.13	19	1.6	320	1.3×10^{-11}	10.4/6	0.11
060505	1163	111	4	42	99	837	0.091	23	2.4	520	5.6×10^{-12}	339	2740	0.13	-3.5	-0.18	400	3.9×10^{-12}	22.1/12	0.036
050509C	1289	28.2	4	22	31	344	0.083	2.3	0.41	200	1.7×10^{-11}	112	965	0.11	4.8	0.43	150	1.5×10^{-10}	0.301/3	0.96
070721A	893.5	112.8	4	30	90	1436	0.059	5.5	0.58	320	6.5×10^{-12}	280	3837	0.077	-15	-0.86	260	1.3×10^{-11}	6.78/12	0.87
070724A	927.5	84.6	4	23	73	720	0.091	7.5	0.88	260	7.3×10^{-12}	246	2042	0.13	-9.3	-0.55	200	1.0×10^{-11}	14.3/9	0.11
070209	926.7	56.4	4	41	37	444	0.091	-3.4	-0.51	480	2.3×10^{-12}	185	1442	0.13	4.8	0.33	370	1.1×10^{-11}	5.35/6	0.50

[a]Three- and four-telescope data are presented.

[b]As the central trigger system had yet to be installed when this observation was made, a slightly different analysis technique was used (see Aharonian et al., 2005).

[c]Soft-cut analysis is not available for this observation.
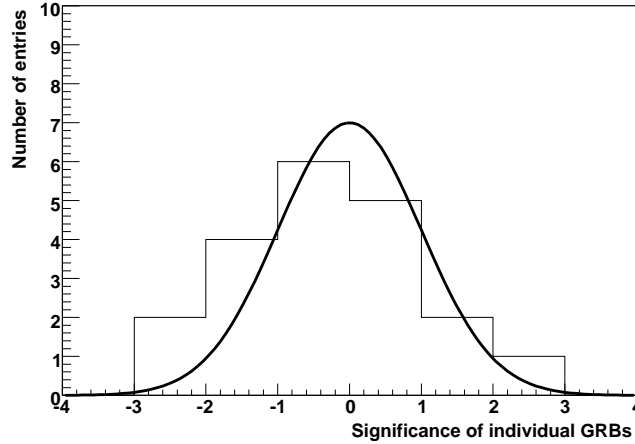
Figure 4.1: Distribution of the statistical significance (*histogram*) as derived from the observations of 20 GRBs using soft-cut analysis. The mean is -0.4 and the standard deviation is 1.4. Each entry corresponds to one GRB. The *solid line* is a Gaussian function with mean zero and standard deviation unity.

4.5.1 Stacking analysis

Although no significant excess was found from any individual GRB, co-adding the excess events from the observations of a number of GRBs may reveal a signal which is too weak to be seen in the data from one GRB, provided that the PSFs of the H.E.S.S. observations are larger than the error box of the GRB positions (which is the case, see Sect. 4.4.1). Firstly, stacking of all GRBs (except GRB 030821) in the sample was performed. This yielded a total of -138 excess events and a statistical significance of -1.78 using the soft-cut analysis. Use of standard cuts produced a similar result (see Table 4.4). Secondly, combining the significance of the results from three selected subsets extracted from the whole sample was performed. The *a priori* selection criteria were to choose those GRBs with a higher expected VHE flux or a lower level of EBL absorption. The following requirements were used to select three subsets:

Sample A: the first 10 in the ranking described in Sect. 4.3.3, excluding GRB 030821 which has a large positional uncertainty;

Sample B: all GRBs with a measured redshift $z < 1$;

Sample C: all GRBs with a soft-cut energy threshold lower than 300 GeV and with either a measured redshift $z < 1$ or with an unknown redshift.

The result is shown in Table 4.4. As can be seen, there is no significant evidence of emission in any of these subsets.

Table 4.3: Differential flux upper limits at the energy thresholds from the H.E.S.S. observations of GRBs with reported redshifts. The limits are given in units of $\mathrm{cm^{-2}\,s^{-1}\,GeV^{-1}}$.

GRB	redshift	E_{th} (GeV)	F_{UL}	$F_{\mathrm{corrected}}$
060505	0.0889	400	3.9×10^{-14}	5.8×10^{-14}
030329	0.1687	1360	7.6×10^{-15}	9.7×10^{-14}
070209	0.314	370	1.2×10^{-13}	8.7×10^{-13}
070724A	0.457	200	2.1×10^{-13}	1.0×10^{-12}
041006	0.716	150	1.8×10^{-12}	2.7×10^{-11}
050801	1.56	310	2.1×10^{-13}	[a]
071003[b]	1.604	280	2.0×10^{-13}	[a]
060526	3.21	220	1.7×10^{-13}	[a]
070721B	3.626	320	1.1×10^{-13}	[a]

[a]Limits corrected for EBL absorption are >10 orders of magnitude larger than that observed.
[b]Only 4-telescope data were used.

Table 4.4: Combined significance of 3 subsets of GRBs selected based on the requirements listed in Sect. 4.5.1

	Number of GRBs	soft-cut analysis	standard-cut analysis
Sample A	9	-2.48	-1.80
Sample B	5	0.35	1.76
Sample C	10	-0.22	0.57
all GRBs	20	-1.78	-0.13

4.5.2 Temporal analysis

As possible VHE radiation from GRBs is expected to vary with time, a temporal analysis to search for deviation from zero excess in the observed data was performed. Soft-cut analysis was used for all GRBs (except GRB 030329) since this analysis has a lower energy threshold and a larger acceptance of γ-rays and cosmic rays and therefore increases the statistics. The γ-like excess events were binned in 10-minute time intervals for each GRB data set and were compared to the assumption of no excess throughout the observed period. The χ^2/d.o.f. value and the corresponding probability are shown in Table 4.2 for each GRB. Within the whole sample, the lowest probability that the hypothesis that the excess was zero throughout the observation period is correct is 1.2×10^{-3} (for GRB 071003) and no significant deviation from zero within any of the GRB temporal data was found. Standard-cut analysis produced consistent results.

4.5.3 GRB 070621: Observations of a GRB with the fastest reaction and the longest exposure time

GRB 070621 is the highest-ranked GRB in the sample (Sect. 4.3.3), i.e. it has the highest relative expected VHE flux at the start time of the observations. The duration of the *Swift* burst was $T_{90} \sim 33$s, thus clearly classifying the burst as a long GRB. The fluence in the 15–150 keV band was $\sim 4.3 \times 10^{-6}$ erg cm^{-2}. The XRT light curve is represented by an initial rapidly-decaying phase and a shallow phase, with the transition happening around $t_0 + 380$s where t_0 denotes the trigger time (Sbarufatti et al., 2007). Despite extensive optical monitoring, no fading optical counterpart was found. The H.E.S.S. observations started at $t_0 + 420$s and lasted for ~ 5 hours, largely coincident with the X-ray shallow phase. These observations were both the most prompt and the longest among those presented. Figure 4.2 shows the 99.9% H.E.S.S. energy flux upper limits above 200 GeV (using soft-cut analysis), together with the XRT results (Evans et al., 2007). As seen, the limits for this period are at levels comparable to the X-ray energy flux during the same period. Unfortunately the lack of redshift information for this burst prevents further interpretation of the limits.

4.5.4 GRB 030821: Observations of a GRB with a large positional uncertainty

Some GRBs, such as GRB 030821, have a large uncertainty in position; with a relatively large camera FoV ($\sim 5°$), the H.E.S.S. telescopes are able to cover the whole positional error box of such GRBs.

Observations of GRB 030821 started 18 hours after the burst and lasted for a live-time of 55.5 minutes, with a mean Z.A. of 28°. The observations were taken when the array was under construction and only two telescopes were operating, resulting in an energy threshold of 260 GeV. The GRB has a relatively large uncertainty in position as determined from *IPN* (the third Interplanetary Network) triangulation (Hurley et al., 2003), and its error box is larger than the PSF of H.E.S.S. However, because of the relatively large FoV of the camera, the whole error box, and thus the possible GRB
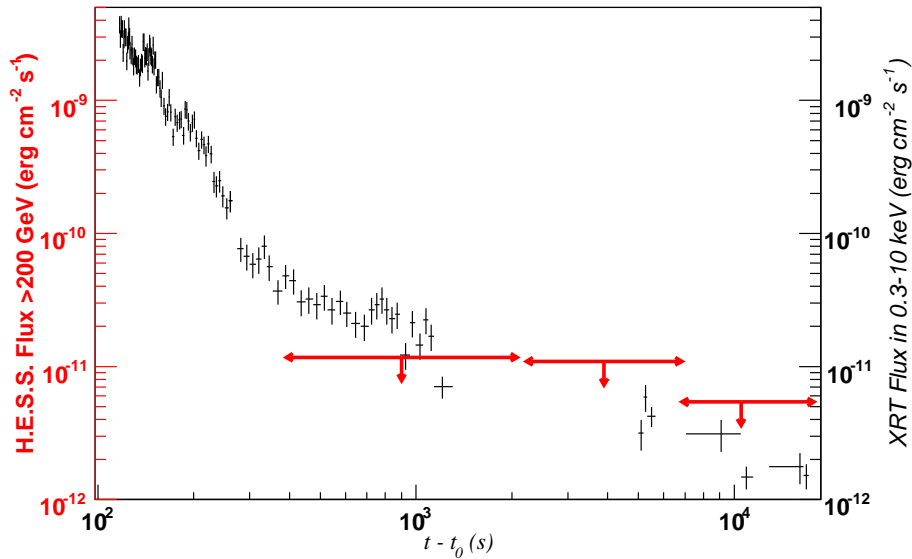
Figure 4.2: The 99.9% confidence level energy flux upper limits (in red) at energies >200 GeV derived from H.E.S.S. observations at the position of GRB 070621. The ends of the horizontal lines indicate the start and end times of the observations from which the upper limits were derived. The XRT energy flux in the 0.3–10 keV band is shown in black for comparison (Evans et al., 2007).

position, is within the H.E.S.S. FoV. The sky excess map overlaid with the error box is shown in Figure 4.3. As can be seen, there is no significant excess at any position within the error box. The sky region with the largest number of peak excess events is located in the south-eastern part of the error box. Using a point-source analysis centred at this peak, a flux upper limit (above 260 GeV) of $\sim 1.7 \times 10^{-11}$ cm^{-2} s^{-1} was derived. Since an upper limit derived for any location in the error box with fewer excess events is *lower* than this value[9], it may be regarded as a *conservative* upper limit of the VHE flux associated with GRB 030821 during the period of the H.E.S.S. observations.

4.6   Discussion

The upper limits presented in this paper are among the most stringent ever derived from VHE γ-ray observations of GRBs during the afterglow period. In fact, the 99.9% confidence level limits (in energy flux) are at levels comparable to the X-ray energy flux as observed by *Swift*/XRT during the same period (see, e.g. Figure 4.2). Unless most of the GRBs are located at high redshifts and thus their VHE flux is severely absorbed by the EBL (this possibility is discussed below), one expects detection of the predicted VHE component with energy flux levels comparable to those in X-rays in some scenarios (Der-

---

[9]A larger excess implies a higher value of the upper limit, since the integrated exposure, which depends on Z.A. and θ_{offset} of the observations, is largely the same over the whole error box.
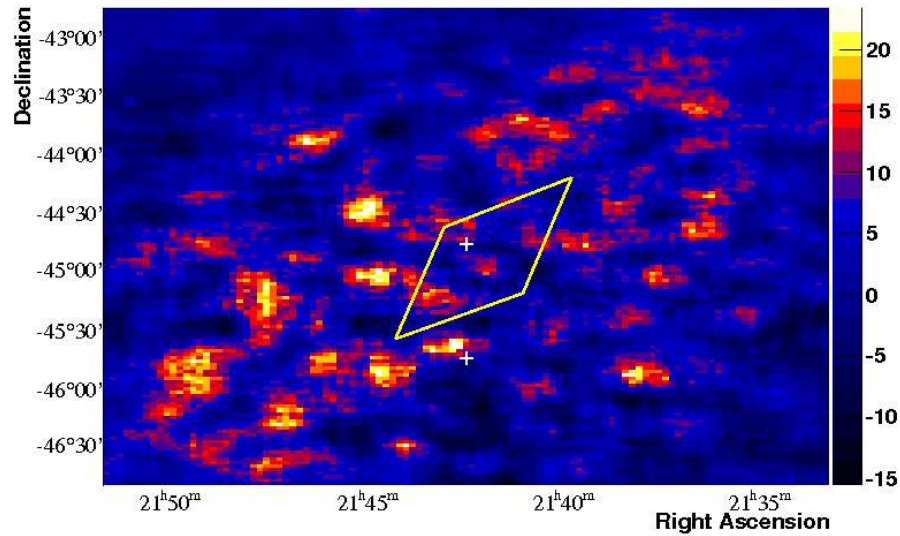
Figure 4.3: The γ-like excess events in the region of the GRB 030821. The error box shows the position of the burst localized by IPN triangulation (Hurley et al., 2003). The colour (grey) scale is set such that the blue/red (black/grey) transition occurs at the $\sim 1.5\sigma$ significance level. The sky map was derived using two observations pointing at two different positions (marked by crosses), resulting in a non-uniform distribution of events in the map.

mer et al., 2000; Wang et al., 2001; Zhang & Mészáros, 2001b; Pe'er & Waxman, 2005; Fan et al., 2008).

On the other hand, the unknown redshifts of many of the GRBs in the sample (including GRB 070621, the highest-ranking, which is discussed in Sect. 4.3.3) complicate the physical interpretation of the data, because EBL absorption at VHE energies is severe for a GRB with $z > 1$. The mean and median redshift of the 9 GRBs with reported redshifts is 1.3 and 0.7, respectively. If the 12 GRBs without redshift have the same redshift distribution, one would expect $\sim 40\%$ of them (~ 5 GRBs) to have $z < 0.5$. In this case, the EBL absorption may not preclude the detection of the predicted VHE γ-rays for the GRB sample presented here[10].

4.7 Outlook

The data from our sample of 21 GRBs do not provide any evidence for a strong VHE γ-ray component from GRBs during the afterglow phase. EBL absorption can explain the lack of detection in our sample. However, this does not exclude a population of GRBs which exhibit a strong VHE component. While the EGRET experiment did not detect MeV–GeV photons from most BATSE GRBs in its FoV, some strong bursts (e.g. GRB 940217)

---

[10]The optical depth of EBL absorption for a ~ 100 GeV photon is ~ 3 at $z = 1$, according to the P0.45 model demonstrated in Aharonian et al. (2006d).

have proved to emit delayed emission, $\sim$1.5 hours after the burst, at energies as high as $\sim$20 GeV (Hurley et al., 1994). With *Fermi*'s observations of GRBs having started in mid-2008, it is likely that our knowledge of the high-energy emission of GRBs will be improved in the near future.

The future prospects for detection at VHE energies rely on the likelihood of observing a GRB with low redshift (e.g. $z < 0.5$) early enough. In the cases where there is no detection, sensitive and early upper limits on the intrinsic VHE luminosity of these nearby GRBs will still improve our understanding of the radiation mechanisms of GRBs.

Franceschini et al. (2008) claimed a very small opacity due to EBL absorption. The optical depth is a factor of three smaller than the one we used (Aharonian et al., 2006d). Therefore, on-going GRB observations with H.E.S.S., as well as other ground-based VHE detectors, are crucial to test this model.

4.8   Conclusions

During 4 years of operation (2003–2007), 32 GRBs have been observed during the afterglow phase using the H.E.S.S. experiment. Those 21 GRBs with high-quality data were analysed and the results presented in this paper. Depending on the visibility and observing conditions, the start time of the observations varied from minutes to hours after the burst.

There is no evidence of VHE emission from any individual GRB during the period covered by the H.E.S.S. observations, nor from stacking analysis using the whole sample and *a priori* selected sub-sets of GRBs. Fine-binned temporal data revealed no short-term variability from any observation and no indication of VHE signal from any of these time bins was found. Upper limits of VHE γ-ray flux during the observations from the GRBs were derived. These 99.9% confidence level energy flux upper limits are at levels comparable to the contemporary X-ray energy flux. For those GRBs with reported redshifts, differential upper limits at the energy threshold after correcting for EBL absorption are presented.

H.E.S.S. phase II will have an energy threshold of about 30 GeV. With much less absorption by the EBL at such low energies, it is hoped that the H.E.S.S. experiment will enable the detection of VHE γ-ray counterparts of GRBs.

Chapter 5

Very high energy γ-ray afterglow emission of nearby γ-ray bursts

The materials presented in this chapter are to be submitted to the *Astrophysical Journal* as a paper.

This research was done together with Rong-Rong Xue, Stefan Wagner, Bagmeet Behera, Yi-Zhong Fan, and Da-Ming Wei. The first idea of this collaboration came from me. The idea has been to combine observational and theoretical efforts to improve our understanding of GRBs in the VHE regime. As one of the two corresponding authors, my major role (apart from writing) in this research has been providing the necessary VHE γ-ray data, including those derived from H.E.S.S. observations of GRB 030329 and GRB 060505. In order to compare the model predictions with these data, I also performed a correction to the modeled fluxes due to EBL, using the opacity data provided by Bagmeet Behera.

Abstract   The synchrotron self-Compton emission from Gamma-ray Burst (GRB) forward shock can extend to the very-high-energy (VHE; $E_\gamma >$100 GeV) range. Such high energy photons are rare and are attenuated by the cosmic infrared background (CIB) before reaching us. In this work, we discuss the prospect to detect these VHE photons using the current ground-based Cherenkov detectors. Our calculated results are consistent with the upper limits obtained with several Cherenkov detectors for GRB 030329, GRB 050509B, and GRB 060505 during the afterglow phase. For 5 bursts in our nearby GRB sample (except for GRB 030329), current ground-based Cherenkov detectors would not be expected to detect the modeled VHE signal assuming observations taken 10 hours after the burst. Only for those very bright and nearby bursts like GRB 030329, detection of VHE photons is possible under favorable observing conditions and a delayed observation time of $\lesssim$10 hours.

5.1 Introduction

Gamma ray bursts (GRBs) are potential extra-galactic sources of GeV and higher energy photons. Evidences of distinct high-energy (HE) component from the low-energy γ-ray component has been accumulated by EGRET on board the Compton Gamma-Ray Observatory: (1) Hurley et al. (1994) reported the detection of long-duration MeV–GeV emission of GRB 940217, lasting up to 1.5 hour after the keV burst including an ∼18 GeV photon. This burst is the longest and the most energetic among those GRBs with detected HE emission so far; (2) González et al. (2003) revealed a HE component of GRB 941017 temporally and spectrally different from the low-energy component.

In the fireball model, synchrotron emission of shock-accelerated electrons is commonly thought to produce prompt γ-ray emission as well as afterglow emission at lower energies (e.g., Sari et al., 1998). It is natural to expect that these photons are inverse-Compton up-scattered by electrons, giving rise to a higher energy component peaking at GeV to TeV energies (Wei & Lu, 1998; Sari & Esin, 2001). When electrons scatter off the self-emitting synchrotron photons, synchrotron self-Compton (SSC) emission is resulted. In the external shock scenario, the temporal profile of the SSC emission from forward shock electrons is similar to that of the low energy afterglow emission and no significant time lag is expected.

The Fermi Gamma-ray Space Telescope (FGST) was launched on June 11, 2008. The Large Area Telescope (LAT) on board covers the energy range from 20 MeV to 300 GeV and its effective area is about 5 times larger than that of EGRET at GeV energies. Dermer et al. (2000), Zhang & Mészáros (2001b), and Wang et al. (2001) predicted promising and detectable SSC emission from the forward shock with FGST out to z∼1.

The *Swift* satellite, thanks to its rapid response time and accurate localization, has started a new era of research on GRBs. Different modifications to the standard afterglow model are put forward to explain the peculiar behaviors exhibited in the X-ray light curves, in particular the shallow declining phase (Zhang et al., 2006; Nousek et al., 2006). Recently, the SSC emission of the modified forward shock has been extensively discussed in the literature (Wei & Fan, 2007; Gou & Mészáros, 2007; Fan et al., 2008; Galli & Piro, 2007; Yu et al., 2007) and has been applied to the case of GRB 940217 (Wei & Fan, 2007).

Most of the discussions in the literature have focused on the afterglow emission from tens of MeV to GeV. LAT can also detect very-high-energy (VHE; >100 GeV) afterglow emission. However, with a small effective area $\sim 10^4$ cm^2, it is very hard to have a significant detection at such a high energy. Imaging atmospheric Cherenkov telescopes (IACTs) such as MAGIC[1], H.E.S.S.[2], and VERITAS[3] may serve better at energies above ∼100 GeV because of their much larger effective area ($\sim 10^8 - 10^9$ cm^2) and a high rejection rate of hadronic background. Some of these large area Cherenkov detectors have been used to set constraints on the possible VHE afterglow component of GRBs (Albert et al., 2007b; Horan et al., 2007; Aharonian et al., 2009). It is thus desirable to see whether these results are consistent with the predictions of the fireball shock model. Our aim of this paper is also to investigate the prospect of significant detections in the future. To

---

[1]http://wwwmagic.mppmu.mpg.de/
[2]http://www.mpi-hd.mpg.de/hfm/H.E.S.S./H.E.S.S..html
[3]http://veritas.sao.arizona.edu/

have a reliable estimate of the afterglow emission at energies above 100 GeV, one need to calculate the forward shock emission (both synchrotron and SSC emission of the shocked electrons) carefully. The attenuation of VHE photons by the cosmic infrared background (CIB) is also taken into account. Since the attenuation effect by the CIB for photons with an energy >100 GeV is more severe for high-redshift GRBs, we limit our GRB sample to nearby events.

This paper is organized as follows: in Section 5.2, we describe the GRB afterglow model, introduce the code that is used in the afterglow modeling, and calculate the SSC emission from GRB forward shock. In Section 5.3, we present the expected results of the SSC model using reasonable parameter values for GRBs. In Section 5.4, we describe the GRB sample which includes six nearby GRBs with sufficient multi-wavelength afterglow data and predict their CIB-corrected energy flux during the afterglow phase, which is then compared with the available observational data. We summarize our results and discuss their implications in Section 5.5. We conclude in Section 5.6.

5.2 Afterglow modeling

5.2.1 GRB Afterglow Model

On February 28, 1997, the first X-ray afterglow of a GRB was detected, leading to the identification of its progenitor at cosmological distances (Costa et al., 1997). In a few days, the afterglow faded away with time as a power law. This behavior is satisfactorily explained in the spherical (isotropic) fireball model involving relativistic ejecta decelerated by circumburst medium (Mészáros & Rees, 1997). The introduction of collimated jets relaxes the energy requirement on some of the more energetic GRBs by a factor of several hundred, as well as explains the steeper temporal decay of afterglows (Rhoads, 1999; Sari et al., 1999).

While synchrotron emission is widely considered to be responsible for the radio, optical, and X-ray afterglows (e.g. Sari et al., 1998), inverse Compton scattering (ICS) of forward shock photons, which may considerably change the temporal and spectral behavior of GRB afterglows, is considered in details by Wei & Lu (1998, 2000) and Sari & Esin (2001). On the other hand, this cooling mechanism of electrons accelerated in external shocks will contribute to the photon spectra at sub-GeV to TeV energies (Mészáros & Rees, 1994; Dermer et al., 2000; Zhang & Mészáros, 2001b; Wang et al., 2001).

In the afterglow model, both synchrotron emission and inverse Compton emission are taken into account. It is assumed that: (1) the external medium is homogenous with a density n or a wind profile $n \propto R^{-2}$; (2) the relativistic jet is uniform, i.e. energy per solid angle is independent of direction within the jet; (3) the shock parameters (ϵ_e and ϵ_B, fractions of the shock energy given to the electrons and the magnetic field, respectively) are constant; (4) the energy distribution of electrons accelerated in shocks follows $dN_e/dE \propto E^{-p}$; (5) the possible achromatic flattening in the afterglow lightcurve is due to energy injection in the form $E_k \propto t^{1-q}$ (Cohen & Piran, 1999; Zhang & Mészáros, 2001a) or $E_k \propto [1 + (t/T)^2]^{-1}$ with T being the initial spin-down time scale (Dai & Lu, 1998).

The parameters involved in this afterglow model include: E_0 (the initial isotropic

outflow energy), θ_0 (the initial half-angle of the jet), n (the density of the homogeneous external medium), p (the power law index of shock-accelerated electron distribution), ϵ_e, and ϵ_B (shock parameters). In the case where energy injection is necessary, three additional parameters: L_{eje} (the injected luminosity in the rest frame), the timescale of energy injection and q, are included.

5.2.2   A brief description of the SSC model

The code used in our afterglow modeling and the prediction of the SSC emission is that developed by Fan et al. (2008). The key treatments (see Section 3 of Fan et al., 2008, for details) are as follows: (i) The dynamical evolution of the outflow is followed using the formulae in Huang et al. (2000), which describe the hydrodynamics in both relativistic and non-relativistic phases. (ii) The arbitrary assumption that the referred system is always in a stable state is considered to be unsatisfactory and the energy distribution of electrons is calculated by solving the continuity equation with the power-law source function $Q = K\gamma_e^{-p}$, normalized by a local injection rate (Moderski et al., 2000). (iii) The observed flux is integrated over the "equal-arrival surface". (iv) The *Klein-Nishina* correction is taken into account in our calculations. Since VHE photons are considered, the ICS emission is significantly suppressed in the *Klein-Nishina* regime. (v) Energy injection into the outflow is considered, if needed, which may change the dynamics dramatically, as mentioned in Section 5.2.1.

5.3   Model prediction

To calculate the corresponding SSC afterglow emission, parameters involved in the afterglow model are needed. In this section, we adopt reasonable parameters involved in the afterglow model for nearby GRBs and predict the spectra in HE to VHE range. After corrected for the attenuation by CIB we compare them with the sensitivity levels of γ-ray detectors.

Parameters are assumed as follows: $E_0 = 10^{51}$erg, $\theta_0 = 0.4$, $n = 1.0$ cm^{-3}, $p = 2.2$, $\epsilon_e = 0.3$, $\epsilon_B = 0.01$, and z=0.16. The time-averaged spectra, including both synchrotron and SSC components from forward shocks are shown in Figure 5.1. Starting times of 0.5 hour, 2 hours, and 10 hours after the burst triggers are assumed. The integrated time interval is fixed at 0.5 hour. For this fictitious burst, current IACTs such as H.E.S.S. would be more likely than *FGST*/LAT to probe the modeled emission, as seen in Figure 5.1.

5.4   Very high energy afterglow emission from nearby GRBs

For photons with energy higher than ~ 100 GeV, the attenuation due to intergalactic infrared background would be significant if the source has a high redshift. Therefore nearby bursts (those with z<0.25) are chosen in this study.
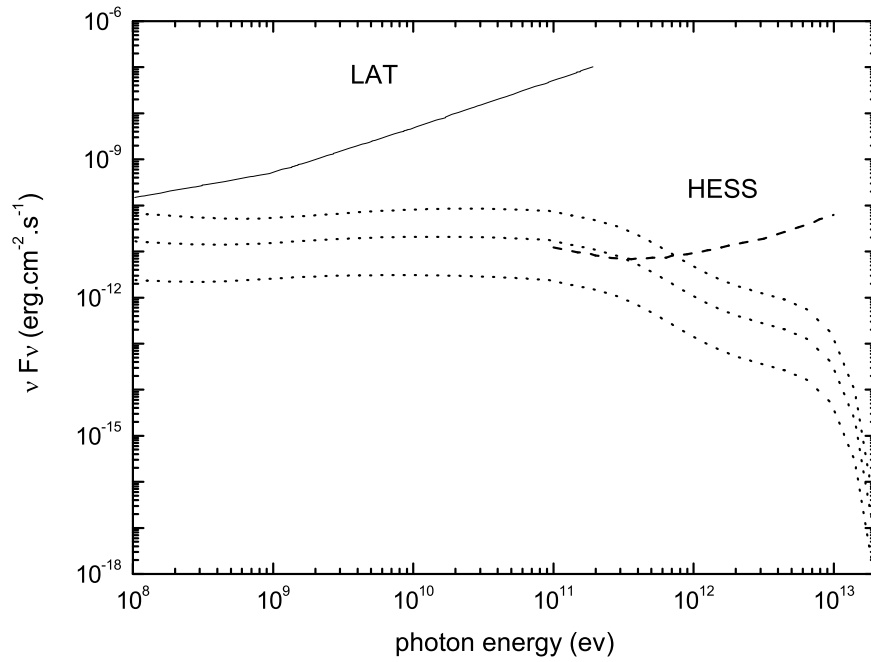
Figure 5.1: Temporal evolution of the HE-VHE spectrum of SSC afterglows. The dotted lines are the spectra for various observer times with the same time exposure of 0.5 hour, starting from (top) 0.5 hour, 2 hours, and (bottom) 10 hours, respectively. All spectra are calculated with the following parameter values: $E_0 = 10^{51}$erg, $\theta_0 = 0.4$, $n = 1.0$cm^{-3}, $p = 2.2$, $\epsilon_e = 0.3$, $\epsilon_B = 0.01$ and $z = 0.16$. The solid line and dashed line represents FGST/LAT (Galli & Piro, 2008) and H.E.S.S. sensitivity (assuming $\Gamma = 2.6$) for an integration time of 0.5 hour, respectively.

5.4.1   The GRB sample

The number of GRBs with low redshifts are quite small. In a study by Amati et al. (2008), less than 10% of the 70 GRBs have a redshift <0.5. On the other hand, the number of GRBs with good enough afterglow data for meaningful afterglow modeling is also rather small.

In this work, we selected 6 nearby GRBs ($z < 0.25$ except GRB 051221A) with relatively high luminosity, and with multi-wavelength afterglow data sufficient to meaningfully constrain the properties of the GRBs (i.e. the model parameter values as described in §5.2.1). They are GRB 030329, GRB 050509B, GRB 050709, GRB 051221A, GRB 060505, and GRB 060614. Though having a relatively large redshift of z∼0.55, GRB 051221A is also considered in this work because it is one of the brightest short GRBs detected so far.

GRB 030329 triggered the High Energy Transient Explorer, HETE-2 (Vanderspek et al., 2004). Based on the emission and absorption lines in the optical afterglow, a redshift of z=0.1685 has been identified (Greiner et al., 2003). Very detailed BVRI afterglow lightcurves, spanning from ∼0.05 to ∼ 80 days, were compiled by Lipkin et al. (2004). Tiengo et al. (2004) reported XMM-Newton and Rossi-XTE late-time observations of this burst. X-ray observations have the advantage, compared to optical observations, of not being affected by possible contributions from supernova and the host galaxy. Due to the brightness and proximity of the event, 3-years radio afterglow data were obtained, and the ejecta has entered into the deep non-relativistic phase (van der Horst et al., 2008).

The X-Ray Telescope (XRT) on board *Swift* began observations of GRB 050509B 62s after the trigger of the Burst Alert telescope (BAT) (Gehrels et al., 2005). Optical and infrared data were reported in Bloom et al. (2006). Prochaska et al. (2005) and Bloom et al. (2005) reported a redshift of z∼0.22 based on numerous absorption features and a putative host galaxy, respectively.

GRB 050709 was discovered by HETE-2 (Villasenor et al., 2005). Its prompt emission lasted 70 ms in the 3-400 keV energy band, followed by a weaker, soft bump of ∼100-s duration. Follow-up observations with the Chandra X-ray observatory revealed a faint, uncatalogued X-ray source inside the HETE-2 error circle (Fox et al., 2005), which was coincident with a pointlike object embedded in a bright galaxy (Jensen et al., 2005) at z = 0.16 (Price et al., 2005). The optical counterpart of this burst was observed with the Danish 1.5-m telescope at the La Silla Observatory. The observations started 33 hours after the burst and spanned over the following 18 days (Hjorth et al., 2005).

GRB 051221A was localized by BAT (Cummings et al., 2005) and also promptly observed by the Konus-Wind instrument. The X-ray ($\sim 10^2 - 2 \times 10^6$s; Burrows et al., 2006) and the optical ($\sim 10^4 - 4 \times 10^5$s; Soderberg et al., 2006b) afterglow light curves of GRB 051221A were well detected, while in the radio band only one detection followed by several upper limits are available (Soderberg et al., 2006b). Soderberg et al. (2006b) detected several bright emission lines, indicating a redshift of $z = 0.5464$.

GRB 060505 was detected by BAT in the 15-150 keV band (Palmer et al., 2006a; Hullinger et al., 2006). XRT detected a source which was located about 4″ from a galaxy with z=0.0894 (Conciatore et al., 2006). Ofek et al. (2006) reported the detection of the optical transient, later confirmed by VLT FORS2 observations (Thoene et al., 2006).

GRB 060614 triggered both *Swift*-BAT (Parsons et al., 2006) and Konus-Wind (Golenet-
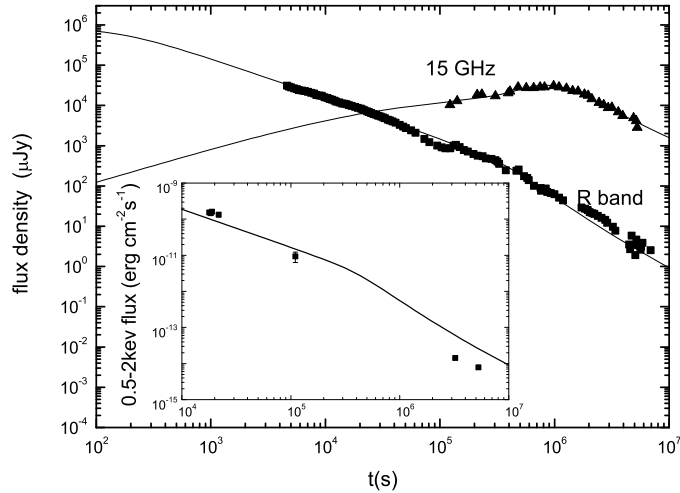
Figure 5.2: *Main figure*: GRB 030329 afterglow data in the 15 GHz (Berger et al., 2003) and *R*-band (Lipkin et al., 2004), Symbols indicate data points as labelled. *Inset*: X-ray afterglow data in the 0.5–2keV band (Tiengo et al., 2004). In both cases, solid lines exhibit the modeled light curves.

skii et al., 2006). XRT found a very bright ($\sim$1300 counts s^{-1}) uncatalogued source inside the BAT error circle. Ground-based optical and infrared follow-up observations were performed using several instruments (e.g., Cobb et al., 2006; Schmidt et al., 2006). Based on the detection of the host galaxy emission lines, a redshift of z = 0.125 was proposed by Price et al. (2006) and confirmed by Fugazza et al. (2006).

5.4.2 Constraining the model parameters

The available multi-frequency afterglow data are then used to obtain the model parameters. Data from at least two different wavebands are required. In this work, we have reproduced the multi-frequency afterglow data of GRB 030329 and GRB 060614.

The well-sampled distinguishing afterglow behavior of GRB 030329 has aroused much attention. Some authors concentrated on the rebrightening occurring at 1.6 days after the trigger and considered different mechanisms to explain the rebrightening features seen in the optical light curves (Huang et al., 2006). We concentrate on the multi-band emission, from radio (Berger et al., 2003), optical (Lipkin et al., 2004) to X-ray band (Tiengo et al., 2004) for the purpose here. We show in Figure 5.2 that, with a set of proper parameters, the numerical result can describe the observed data in all three wavebands. It should be noted that we neglect the late re-brightening features in R band afterglows around 10^5s in the modeling. No energy injection is included in our model, i.e. the total energy of the relativistic ejecta is kept constant. The corresponding HE-VHE emission does not depend on the small fluctuations seen in the radio-to-optical afterglow lightcurves.

Table 5.1: Model parameters for six nearby GRBs

GRB	z	E_0 (erg)	θ_0	n (cm^{-3})	p	ϵ_e	ϵ_B	L_{eje}	q	$T_{\rm inj}$[a] (s)	ref.
030329	0.1685	1.4×10^{53}	0.31	100	2.01	0.1	0.001	...	...	...	[b]
050509B	0.2248	2.75×10^{48}	0.5	1	2.2	0.15	0.046	...	...	...	[c]
050709	0.16	3.77×10^{50}	0.5	6×10^{-3}	2.6	0.4	0.25	...	...	...	[d]
051221A	0.5465	10^{52}	0.1	0.01	2.4	0.3	2×10^{-4}	2×10^{48} [e]		$< 1.5 \times 10^4$	[f]
060505	0.089	2.6×10^{50}	0.4	1	2.1	0.1	0.008	...	...	...	[g]
060614	0.125	5×10^{50}	0.08	0.05	2.5	0.12	2×10^{-4}	10^{48}	0	$10^3 - 2 \times 10^4$	[b]

[a]injection timescale
[b]this work
[c]Bloom et al. (2006)
[d]Panaitescu (2006)
[e]magnetar wind
[f]Fan & Xu (2006)
[g]Xu et al. (2009)

The modeled and observed afterglow lightcurves of GRB 060614 are shown in Figure 5.3. Unlike GRB 030329, energy injection, starting around 30 minutes after the GRB onset, is needed in the afterglow modeling to reproduce the increase in flux (instead of simple power-law decay seen for other GRBs). The early X-ray flux before 500s after the GRB onset, which is much brighter than the modeled flux, results from the dominating contribution from the prompt emission.

Table 5.1 lists the physical parameters derived from the afterglow modeling for these six bursts. Parameters of GRB 050509B, GRB 050709, GRB 051221A, and GRB 060505 are taken from Bloom et al. (2006), Panaitescu (2006), Fan & Xu (2006), and Xu et al. (2009), respectively. Bloom et al. (2006) fit the afterglow data of GRB 050509B with four sets of physical parameters. The last two include a high redshift of $z \sim 3$, which is not consistent with the one ($z\sim0.22$) identified by Prochaska et al. (2005) and Bloom et al. (2005). In the second set of parameters, the GRB efficiency is below 0.001, which is rather unusual. In this work, we adopt their first set of physical parameters. For GRB 050709 the low-energy/high-density solution in Panaitescu (2006) is more favored since this short burst was localized in a star-forming galaxy (Covino et al., 2006).

5.4.3   VHE gamma-ray observational data

We are interested in VHE observations during the afterglow phase when the SSC is likely to dominate (see Section 5.5). VHE γ-ray afterglow data of three of the GRBs in the sample (i.e. GRB 030329, GRB 050509B, and GRB 060505) are available. We describe them in the following.

GRB 030329

Horan et al. (2007) reported a total of 4 hours of observations, which spanned five nights, using the Whipple 10-m telescope. No evidence for VHE γ-ray signal was found during any of the observation periods. When combining all data, a flux upper limit of $1.4 \times$
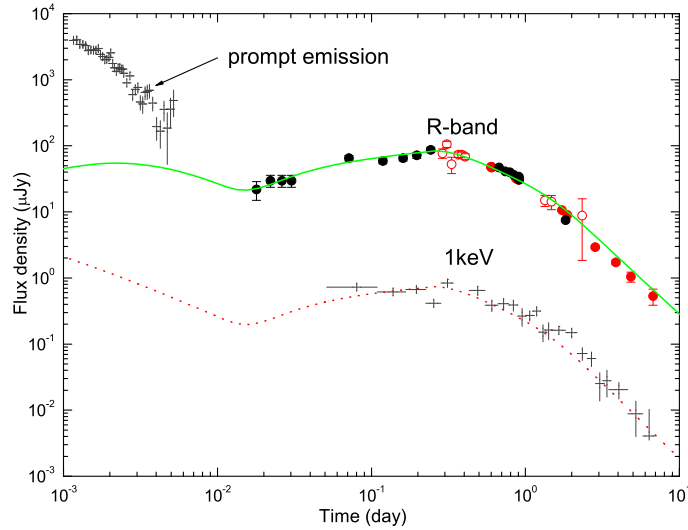
Figure 5.3: GRB 060614 afterglow data in the R-band and X-ray (1 keV) band (see also Xu et al., 2009). Solid and dashed lines represent the modeled R-band and 1 keV emission, respectively.

$10^{-11}\mathrm{erg\,cm^{-2}s^{-1}}$ was derived. The first observation, lasting for about an hour, was started 64.6 hours after the burst. The 99.7% c.l. flux upper limit above an energy of ~ 400 GeV derived from this observation is shown in Table 5.2, as well as in Figure 5.5.

The 28-minute H.E.S.S. observation of began 11.5 days after the burst (Tam et al., 2008). Since the burst position was located above the northern hemisphere, the zenith angle of the GRB observation was relatively large, i.e. 60°, thus having an energy threshold of 1.36 TeV. No evidence for VHE γ-ray signal was found. The 99% c.l. flux upper limit (> 1.36 TeV) is $3.4 \times 10^{-11}\mathrm{erg\,cm^{-2}s^{-1}}$, assuming a photon index of $\Gamma = 3$.

GRB 050509B

The STACEE observations of this burst using the STACEE detector employ an *on-off observation mode* and contain two 28-minute on/off pairs. The first on-source observation started 20 minutes after the burst and the second 80 minutes after the burst. After data quality cuts, about 18 minutes of useful on-source data remain in each observation. No evidence for VHE γ-ray signal above the energy threshold of 150 GeV was reported by Jarvis et al. (2008). The 95% c.l flux upper limits (above 150 GeV, assuming a photon spectrum of $dN/dE \sim E^{-2.5}$) were $3.8 \times 10^{-10}\mathrm{erg\,cm^{-2}s^{-1}}$ and $4.5 \times 10^{-10}\mathrm{erg\,cm^{-2}s^{-1}}$ for the first and second on-source observation respectively (A. Jarvis private communication).

Table 5.2: VHE GRB observations and model predictions

GRB	telescope	$T_{OBS} - T_{GRB}$[a]	exposure	E_{th}[b] (GeV)	$F_{UL,obs}$[c] $(\mathrm{erg\,cm^{-2}\,s^{-1}})$	$F_{UL,pre}$[d] $(\mathrm{erg\,cm^{-2}\,s^{-1}})$	ref.
030329	H.E.S.S.	11.5 days	28 min	1360	3.4×10^{-11}	8.5×10^{-15}	e
030329	Whipple	64.55 hours	65.2 min	400	5.8×10^{-11}	6.7×10^{-13}	f
050509B	STACEE {	20 min	28 min	150	3.8×10^{-10}	2.2×10^{-16}	} g
		80 min	28 min	150	4.5×10^{-10}	5.4×10^{-17}	
060505	H.E.S.S.	19.4 hours	2 hours	450	8.8×10^{-12}	2.5×10^{-15}	e

[a]The time between the start of the GRB and the beginning of observations for different telescopes.
[b]Energy threshold
[c]Energy flux upper limit set by observations
[d]Predicted energy flux
[e]Tam et al. (2008)
[f]Horan et al. (2007)
[g]Jarvis et al. (2008)

GRB 060505

The H.E.S.S. observations began 19.4 hours after the burst and lasted for 2 hours (Tam et al., 2008). No evidence for VHE γ-ray signal was found. The 99% c.l. flux upper limit (> 0.45 TeV) is $8.8 \times 10^{-12}\mathrm{erg\,cm^{-2}s^{-1}}$, assuming a photon index of $\Gamma = 3$.

5.4.4   Comparison to observations

Based on the parameters obtained in Section 4.2, the GeV-TeV emission is obtained using the code described in Section 2.2.

We depict the calculated HE-VHE afterglow spectrum in Figure 5.5, which shows the time-integrated high energy afterglow spectrum of these six events. The solid and dashed lines represent the intrinsic SSC spectra and CIB-absorbed spectra for each GRB, respectively. The absorption is based on the CIB model "P0.45" (Aharonian et al., 2006d)[4], which is constrained by the upper limits provided by two unexpectedly hard spectra of blazars at optical/NIR wavelengths and is close to the lower limit from integrated light of resolved galaxies.

In order to compare with the VHE observational data which are usually given in integrated photon fluxes, we integrate the spectra over frequencies. We consider first the GRBs with VHE data. These include GRB 030329, GRB 050509B, and GRB 060505. In Table 5.2 we list the modeled integrated energy fluxes after CIB-absorption, as well as the VHE γ-ray observations and the derived upper limits. All predicted fluxes are below the upper limits derived from the VHE observations.

The H.E.S.S. detector can detect a point source with an energy flux (>200GeV) as low as $6 \times 10^{-12}\mathrm{erg\,cm^{-2}\,s^{-1}}$ for 2 hours, assuming a $\Gamma=2.6$ spectrum (Aharonian et al., 2006b). This sensitivity level is shown in Figure 5.4. For softer spectra, the level is slightly higher (c.f. Aharonian et al., 2005a).

---

[4]This implies a gamma ray horizon at a redshift of about 0.2 (0.05) for 500 GeV (10 TeV) gamma rays.
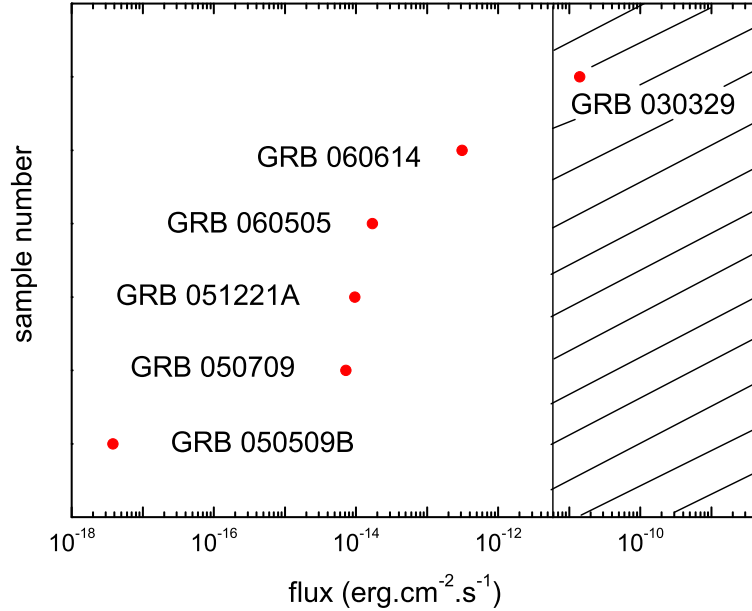
Figure 5.4: *Dots*: Modeled VHE integral energy fluxes above 200 GeV for six nearby GRBs in our sample, assuming that observations begin 10 hours after the burst at zenith angle <20° (thus an energy threshold of ∼200 GeV). *Vertical line*: H.E.S.S. sensitivity (>200GeV) for a 5-σ detection in 2 hours, assuming a Γ=2.6 spectrum source. A source with flux in the *shaded region* (above the H.E.S.S. sensitivity) can be detected.

We then investigate whether a VHE instrument like H.E.S.S. is expected to detect the predicted VHE signal from nearby GRBs during the late afterglow phase. We choose a delayed observation time of 10 hours after the burst. The CIB-absorbed energy fluxes (above 200 GeV) are found to be 3.8×10^{-18}erg cm^{-2} s^{-1} (GRB 050509B), 7.2×10^{-15}erg cm^{-2} s^{-1} (GRB 050709), 9.6×10^{-15}erg cm^{-2} s^{-1} (GRB 051221A), 1.7×10^{-14}erg cm^{-2} s^{-1} (GRB 060505) and 3.1×10^{-13}erg cm^{-2} s^{-1} (GRB 060614). For GRB 030329 which is a bright burst with low redshift, the expected energy flux would be as high as 1.4×10^{-11}erg cm^{-2} s^{-1} if the observation began 10 hours after the burst onset and the GRB position was favorable, i.e. with zenith angle < 20° (and thus an energy threshold of ∼ 200 GeV is attained).

5.5   Discussion

In this paper, we have calculated the SSC emission from the forward shock electrons following Fan et al. (2008). We shall discuss here the importance of other radiation processes in the late afterglow phase.

Possible VHE γ-ray emission initiated from protons has been suggested (Totani, 1998a; Böttcher & Dermer, 1998). However, the proton-synchrotron component, as well as the

hadron-related photo-meson electromagnetic components, is in most cases overshadowed by the SSC component of electrons in the afterglow phase. This is especially the case when the observation is carried out hours after the burst, and for the parameter values of ϵ_e and ϵ_B used here in the modeling of these six GRBs (Zhang & Mészáros, 2001b).

Another possible contribution to VHE emission is related to the X-ray flare phenomenon. X-ray flares have been detected during the afterglow phase in a significant fraction of *Swift* GRBs (Falcone et al., 2007; Chincarini et al., 2007). Corresponding VHE γ-ray flares, as a result of IC-scattering of X-ray flare photons, are predicted (Galli & Piro, 2007; Fan et al., 2008). Since no X-ray flare was detected for the six GRBs in our sample, we do not consider this component.

The effective collecting area of Cherenkov telescopes increases with energy (Aharonian et al., 2006b). On the other hand, high energy photons, especially those in the TeV range, will be severely attenuated by the CIB, the level of which is not well understood. Various models of the CIB's spectral energy distribution are proposed (Primack et al., 2001; Totani & Takeuchi, 2002; Kneiske et al., 2002; Stecker et al., 2006), but all these models give comparable opacities for low redshifts. In this work, a reasonable CIB level consistent with a study of two distant blazars and galaxy counts is used (Aharonian et al., 2006d).

As shown in Figure 5.4 we only expect detectable signal using a ground-based γ-ray detector like H.E.S.S. for a bright, nearby GRB similar to GRB 030329. The rate of nearby GRBs as energetic as GRB 030329 is very uncertain. GRB 940217 might be such an event (Wei & Fan, 2007). If this is true, the event rate would be ~ 1 in a few years. So one can hope for one detection in the VHE band during the late afterglow phase per a couple of years.

Several factors which reduce the chance of detecting VHE photons may be summarized as follows: Firstly, as a result of large zenith angles (e.g., 60° for GRB 030329), the energy thresholds of some observations are relatively high ($\sim$1.4 TeV). Any VHE photons are severely attenuated by CIB light, unless the CIB level is very low. Secondly, the observations were taken at late epochs, e.g. 11.5 days after the burst for H.E.S.S. observations of GRB 030329, when expected VHE flux had largely decayed. Thirdly, the fraction of low-redshift GRBs is small, e.g. <10% for GRBs with z<0.5 (Amati et al., 2008). For GRB 051221A (at $z = 0.55$) studied here, the attenuation is severe at energies $\gtrsim$200 GeV.

Detection of VHE afterglow emission of GRBs is still probable. Those GRBs close enough (z<0.5) and with an intrinsic high luminosity (like GRB 030329), can be detected above $\sim$200 GeV when the observation is taken within $\sim$10 hours after the burst. A rough estimate of the energy-integrated VHE afterglow flux (without correction of the CIB absorption), say, above 100 GeV, is given by

$$F_{>100\text{GeV}} \propto \frac{(1+z)L_{\text{ssc}}}{D_L^2} \max\{(\nu_c^{\text{ssc}})^{\frac{p-2}{2}},\ (\nu_m^{\text{ssc}})^{\frac{p-2}{2}}\}, \tag{5.1}$$

where L_{ssc} is the total luminosity of the SSC emission (see eq.(23-27) in Fan et al., 2008, for the expression), ν_m^{ssc} and ν_c^{ssc} are the typical SSC emission frequency and the SSC cooling frequency of the forward shock electrons (see eq.(33-34) in Fan et al., 2008, the case of $k = 0$, for the expressions). Therefore, GRBs with low z, large E_0, large ϵ_e, and

small ϵ_B in low density circumburst medium are more likely to be detected in the VHE band when referring to the basic parameters in the afterglow model.

Together with AGILE and FGST, ground-based γ-ray detectors will provide us with a continuous spectrum in high energy band during the early afterglow phase. They in turn will shed new light on both the GRB physical model and the cosmic background feature extending to the early universe.

5.6   Conclusions

In this work, we discuss the prospect of detecting VHE γ-rays with current ground-based detectors in the late afterglow phase. During this phase, the dominant radiation process in the VHE γ-ray regime is the SSC emission from the forward shock electrons. *Klein-Nishina* effects and CIB attenuation, both known to suppress the VHE γ-ray spectra, were taken into account. To minimize the effect of CIB attenuation, we chose a sample of six nearby GRBs in this study. We have calculated the detailed SSC emission numerically using the model developed by Fan et al. (2008), with a series of parameters which are able to reproduce the available multi-wavelength afterglow light curves. The results are consistent with the upper limits obtained using VHE observations of GRB 030329, GRB 050509B, and GRB 060505. Moreover, assuming observations taken 10 hours after the burst, the VHE signal predicted from five GRBs is below the sensitivity level of current Cherenkov detectors like MAGIC, H.E.S.S., and VERITAS. For those bright and nearby bursts like GRB 030329, a VHE detection is possible even with a delayed observation time of $\sim$10 hours.
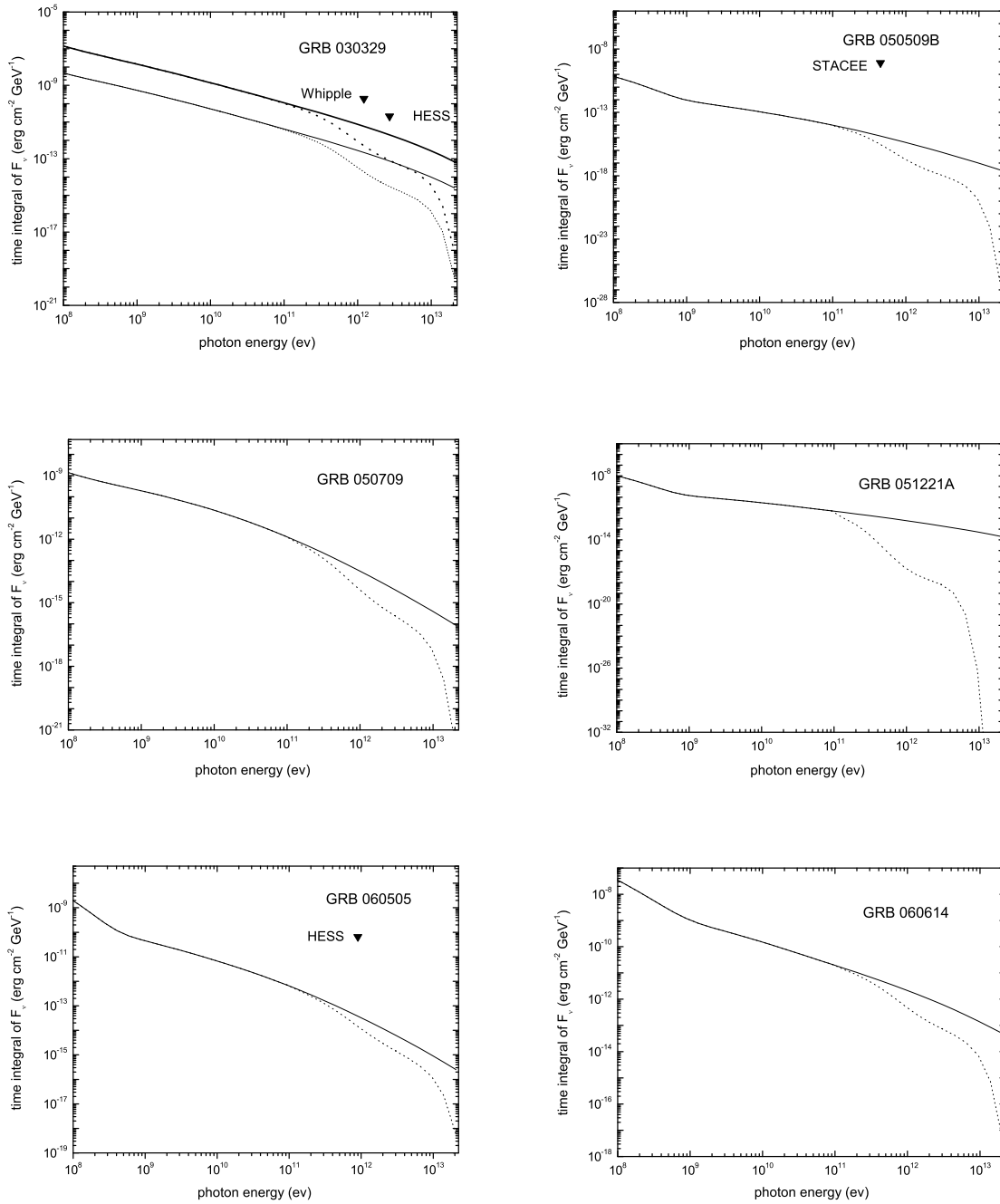
Figure 5.5: Modeled time-integrated 0.1 GeV – 20 TeV afterglow spectra of six GRBs, in comparison with VHE upper limits (triangles). Dotted and solid lines represent the spectra with and without CIB-correction, respectively. For GRB 030329, GRB 050509B, and GRB 060505, the spectra were integrated over the corresponding time intervals during which the upper limits were derived, as shown in Table 5.2. For GRB 030329, thick (upper) lines indicate the modeled spectrum for the Whipple observation time, and thin (lower) lines for the H.E.S.S. observation time. The data points are plotted at the corresponding average photon energies. The modeled spectra of the remaining three bursts are obtained by integrating the spectra over a time period of 2 hours, starting from 10 hours after the trigger.

Chapter 6

H.E.S.S. Observations of the Prompt and Afterglow Phases of GRB 060602B

The first part of this chapter (Abstract and Sections 6.1 to 6.7) was written by the H.E.S.S. collaboration as a paper, of which I am the corresponding author. It will be published[1] in the *Astrophysical Journal*. Special efforts were made on producing the effective areas of positions offset by 3 degrees from the center of the FoV by Konrad Bernlöhr and Dalibor Nedbal, as well as on verifying my results presented here by Mathieu de Naurois.

The second part of this chapter (Sections 6.8 and 6.9) presents my detailed studies on two specific aspects – large-offset observations and the nature of GRB 060602B.

Abstract   We report on the first completely simultaneous observation of a gamma-ray burst (GRB) using an array of Imaging Atmospheric Cherenkov Telescopes which is sensitive to photons in the very-high-energy (VHE) γ-ray range ($\gtrsim$ 100 GeV). On 2006 June 2, the *Swift* Burst Alert Telescope (BAT) registered an unusually soft γ-ray burst (GRB 060602B). The burst position was under observation using the High Energy Stereoscopic System (H.E.S.S.) at the time the burst occurred. Data were taken before, during, and after the burst. A total of 5 hours of observations were obtained during the night of 2006 June 2–3, and 5 additional hours were obtained over the next 3 nights. No VHE γ-ray signal was found during the period covered by the H.E.S.S. observations. The 99% confidence level flux upper limit (>1 TeV) for the *prompt* phase (9 s) of GRB 060602B is $2.9 \times 10^{-9} \, \mathrm{erg \, cm^{-2} \, s^{-1}}$. Due to the very soft BAT spectrum of the burst compared to other *Swift* GRBs and its proximity to the Galactic center, the burst is likely associated with a Galactic X-ray burster, although the possibility of it being a cosmological GRB cannot be ruled out. We discuss the implications of our flux limits in the context of these two bursting scenarios.

---

[1]a preprint version is available at http://arxiv.org/abs/0809.2334

6.1   Introduction

Gamma-ray bursts (GRBs) are brief and intense flares of γ-rays. Without precedent in astronomy, they arrive from random directions in the sky and last typically $\sim$0.1–100 s (*prompt* emission, see Klebesadel et al., 1973; Fishman & Meegan, 1995). The very nature of GRBs makes it operationally rather challenging to study their *prompt* phase simultaneously in any other wavelength.

The observed GRB properties are generally well explained by the *fireball* model, in which the emission is produced in relativistic shocks (Piran, 1999; Zhang & Mészáros, 2004; Mészáros, 2006). In this standard model, the highly-relativistic plasma, which emits the observed sub-MeV radiation, is expected to generate γ-rays up to the very-high-energy (VHE; $\gtrsim$100 GeV) regime, via inverse-Compton emission of electrons or proton-induced mechanisms (Zhang & Mészáros, 2001b; Pe'er & Waxman, 2005; Asano & Inoue, 2007; Fan et al., 2008). Therefore, the detection of gamma-rays or sufficiently sensitive upper limits would shed light on our understanding of the current model. Some important yet largely unknown parameters in GRB models, such as the bulk Lorentz factor and the opacity of the outflow just after the acceleration phase, can be directly measured through high-energy (HE; $\gtrsim$100 MeV) and VHE γ-ray observations during the *prompt* phase of GRBs (Razzaque et al., 2004; Baring, 2006).

There are two techniques used in VHE γ-ray astronomy to observe the *prompt* phase: the first technique is to slew quickly to the GRB position provided by a burst alert from satellites. This technique is used for Imaging Atmospheric Cherenkov Telescopes (IACTs), such as the High Energy Stereoscopic System (H.E.S.S.), which have a field of view (FoV) of a few degrees. The MAGIC telescope, operating in this mode, was able to slew to the position of GRB 050713A, 40 s after the GRB onset, while the *prompt* keV emission was still active. A total of 37 minutes of observations were made and no evidence of emission above 175 GeV was obtained (Albert et al., 2006a). The rapid follow-up observations using this telescope of 8 other GRBs show no evidence of VHE γ-ray emission from these GRBs during the *prompt* or the *early afterglow* phase (Albert et al., 2007b). However, there is always a delay in time for IACTs operating in this GRB-follow-up mode, as long as the GRB position lies outside the camera FoV at the onset of the GRB. This results in an incomplete coverage of the GRB *prompt* phase.

The second technique is to observe a large part of the sky continuously, at the expense of much lower sensitivity than the IACT detectors. This technique is used, e.g. for the water Cherenkov detector Milagro, which works at higher energies than current IACTs. Since the effect of extra-galactic background light (EBL) absorption increases with the energy of a γ-ray photon, the higher energy threshold of Milagro thus lowers its chance to detect VHE γ-rays from distant GRBs, when compared to IACT detectors. No evidence of VHE γ-ray emission was seen from 39 GRBs using this detector (Atkins et al., 2005; Abdo et al., 2007). Atkins et al. (2000) reported a possible VHE γ-ray enhancement coincident with GRB 970417A (with a post-trials probability 1.5×10^{-3} of being a background fluctuation) using Milagrito, the forerunner of Milagro.

In this paper, we report on the first completely simultaneous observation with an IACT instrument of a γ-ray burst (GRB 060602B) using H.E.S.S. The burst position fell serendipitously at the edge of the FoV of the H.E.S.S. cameras when the burst occurred.

6.2   GRB 060602B

At 23:54:33.9 UT on 2006 June 2 (denoted by t_0), the Burst Alert Telescope (BAT) on board *Swift*, which operates in the $15-350$ keV energy band, triggered on GRB 060602B (trigger 213190, Schady et al., 2006). The refined BAT position was R.A. $= 17^h49^m28.2^s$, Dec. $= -28°7'15.5''$ (J2000; Palmer et al., 2006b). The BAT light curve showed a single-peaked structure lasting from $t_0 - 1$ s to $t_0 + 9$ s (Figure 6.1). The peak was strongest in the 15–25 keV energy band and was not detected above 50 keV. T_{90} (defined as the time interval between the instants at which 5% and 95% of the total integral emission is detected in the 15–350 keV band) was 9 ± 2 s (Palmer et al., 2006b). This $\sim$9-s time interval is referred to as the *prompt* phase of this GRB in this work. Palmer et al. (2006b) fit the time-averaged energy spectrum from $t_0 - 1.1$ s to $t_0 + 8.8$ s by a simple power law with a photon index of 5.0 ± 0.52, placing it among the softest of the *Swift* GRBs. Using the data from the same time interval, a 15–150 keV fluence of $(1.8 \pm 0.2) \times 10^{-7}$ erg cm^{-2} was derived. No spectral evolution was observed during the burst (Wijnands et al., 2008).

Swift's other instrument, the X-ray Telescope (XRT), began data-taking 83 s after the BAT trigger and found a fading source. Beardmore et al. (2006) reported a position R.A. $= 17^h49^m31.6^s$, Dec. $= -28°8'3.2''$ (J2000), confirmed by later analyses (Butler, 2007; Wijnands et al., 2008). This position (with an error circle of radius $\sim3.7''$) was used in analyses presented in this paper. The flux faded temporally as a power law with an index of 0.99 ± 0.05 from $\sim t_0 + 100$ s up to $\sim t_0 + 10^6$ s (Wijnands et al., 2008).

Using data taken from $t_0 + 100$ s to $t_0 + 11.4$ ks, the time-averaged 0.3–10 keV energy spectrum was fitted by an absorbed power-law model, $dN/dE \propto E^{-\Gamma_X}$, where E is the photon energy in keV and Γ_X the photon index. The fit results in $\Gamma_X = 3.1^{+0.7}_{-0.6}$ and an absorption column density of $N_H = 4.6^{+1.6}_{-1.4} \times 10^{22}$cm^{-2}, with χ^2/d.o.f $= 34/35$. Fitting the same spectrum with an absorbed blackbody model, $dN/dE \propto E^2/[(kT)^4(e^{E/kT} - 1)]$, a temperature of $kT = 0.94^{+0.15}_{-0.13}$ keV and $N_H = 1.5^{+1.0}_{-0.9} \times 10^{22}$cm^{-2} were obtained, with χ^2/d.o.f $= 36/35$. These two modeled *source* spectra are shown in Figure 6.2, for comparison with the H.E.S.S. upper limits obtained over a comparable time interval. While the modeled *source* spectra look very different, after different levels of absorption along the line of sight, they both describe the observed data equally well, as shown by the normalized χ^2 values both close to 1. These results are consistent with the analyses of other authors (Beardmore et al., 2006; Wijnands et al., 2008).

In the optical or infrared band, no counterpart was found by the observations of several telescopes (Kubánek et al., 2006; Khamitov et al., 2006; Blustin et al., 2006; Melandri et al., 2006). This is expected because of the severe optical extinction along this line of sight.

6.3   The H.E.S.S. Observations

The H.E.S.S. array is a system of four 13m-diameter IACTs located in the Khomas Highland of Namibia (Hinton, 2004). The system has a point source sensitivity above 100 GeV of $\sim 4 \times 10^{-12}$ erg cm^{-2} s^{-1} (about 1% of the flux from the Crab nebula) for a 5σ detection in a 25 hour observation. The cameras of the H.E.S.S. telescopes detect Cherenkov
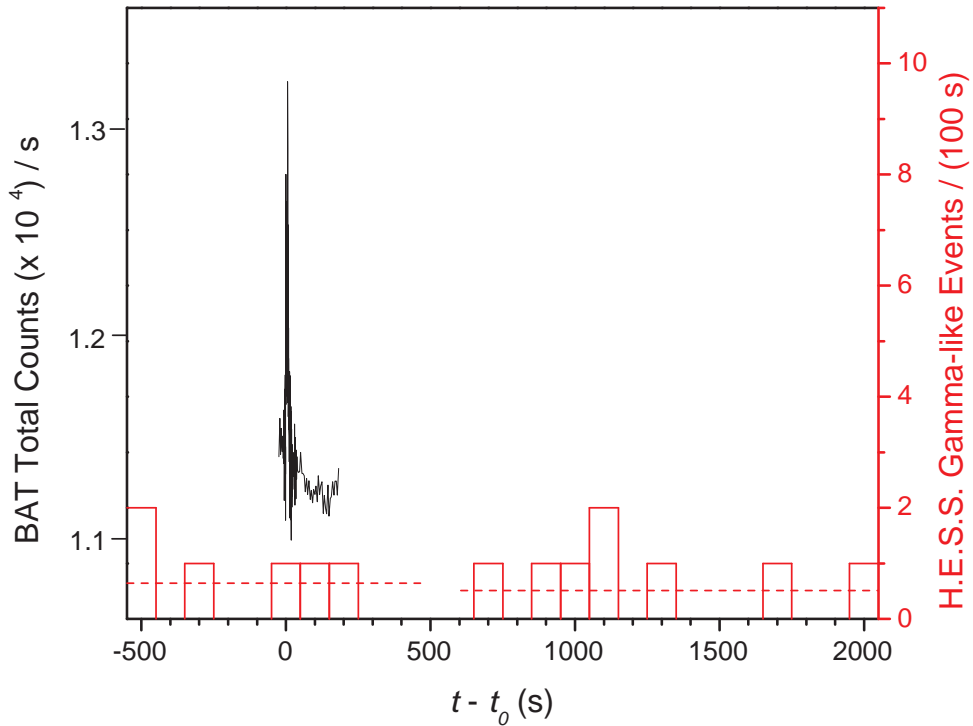
Figure 6.1: *Histograms and right scale*: Gamma-like events, i.e. those that passed standard cuts, as observed using H.E.S.S. within a circular region of radius $\theta_{\text{cut}} = 0.32°$ (for $t < t_0 + 500$s, with a large offset, see text) and $\theta_{\text{cut}} = 0.11°$ (for $t > t_0 + 600$s) centered at the burst position. The dashed horizontal lines indicate the expected number of background events in the circular regions, using the reflected-region background model (Berge et al., 2007). The gap between $\sim$500s and 600s is due to a transition between observation runs. *Solid curve and left scale*: *Swift*/BAT light curve in the 15-150 keV band.
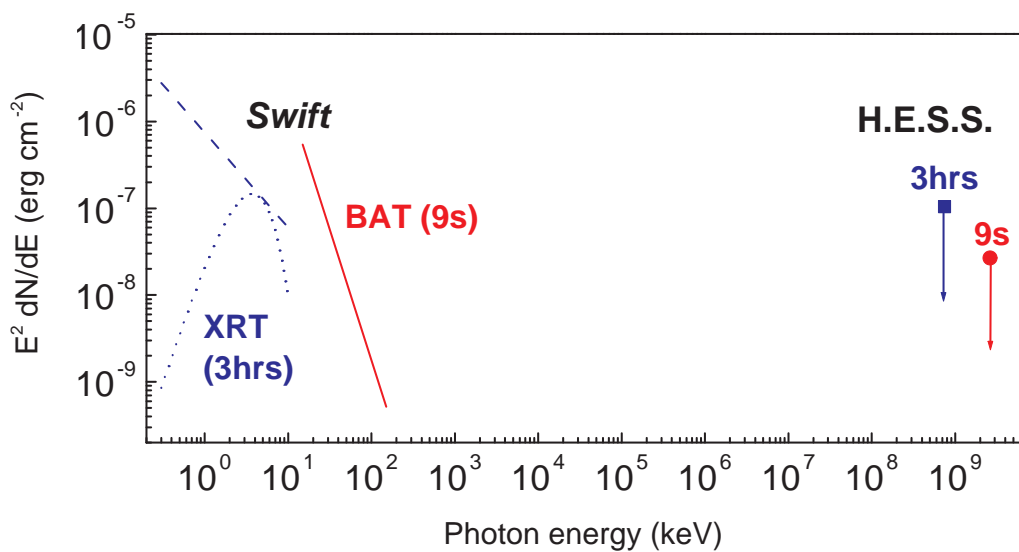
Figure 6.2: Time-integrated spectral energy distributions at the burst position during the 9-s *prompt* phase and during the 3-hour *afterglow* phase. A power-law model fitted to the BAT spectrum during the 9-s burst (solid line) is shown, as well as the *source* spectra used in an absorbed power-law model (dashed line) and an absorbed blackbody model (dotted line) to describe the XRT spectrum during $100\,\mathrm{s} - 11.4\,\mathrm{ks}$ after the burst onset. The H.E.S.S. upper limits derived from 9-s *prompt* data (circle) and 3-hour *afterglow* data (square) are also indicated. The H.E.S.S. *prompt* and *afterglow* limits are plotted at the corresponding average photon energies.

photons over a 5° FoV, thus enhancing its ability to detect serendipitous sources, as demonstrated in the Galactic plane survey (Aharonian et al., 2005c).

The position of GRB 060602B was under observation using H.E.S.S. before the burst, throughout the duration of the burst, and after the burst. The observations are shown in Table 6.1. The zenith angles (Z.A.) and the offsets of the GRB 060602B position from the center of the FoV are shown for each observation period. A total of 4.9 hours of observations were obtained during the night of 2006 June 2–3. This includes 1.7 hour *pre-burst*, 9 s *prompt*, and 3.2 hour *afterglow* phases. Additionally, 4.7 hours of observations at the burst position were obtained over the next 3 nights. All data were taken in good weather conditions and with good hardware status. The observations were taken with the GRB 060602B position placed at different offsets relative to the center of the FoV of the telescopes, because most observations were not dedicated to the position of GRB 060602B. The position offsets were rather large ($\geq 2.5°$) during the period before the burst until ∼9 minutes after the burst.

Due to the H.E.S.S. long term monitoring program of the Galactic center region, a deep exposure of the GRB 060602B position (over a period of several years) also exists (see Section 6.5).

6.4   H.E.S.S. Data Analysis

Calibration of data, event reconstruction and rejection of the cosmic-ray background (i.e. γ-ray event selection criteria) were performed as described in Aharonian et al. (2006b), which employ the techniques described by Hillas (1996). Targets are typically observed at a *normal* offset from the FoV center of 0.5° or 0.7° (*wobble* mode), to allow for a simultaneous background estimate from regions in the FoV that have identical properties as the source position. At *normal* offsets, the point spread function (PSF) and effective area for γ-rays are nearly identical to the values at the FoV center, according to air-shower simulations. However, the reconstructed event directions are less accurate at larger offsets. The PSF at the maximum offset of 2.9° is by a factor of ∼2 more extended than the one at *normal* offsets. Figure 6.3 shows the effective areas for various photon energies at offsets from 0° to 3° from the center of the FoV for Z.A.= 0°, using the standard cut analysis described below.

Gamma-like events were then taken from a circular region of radius θ_{cut} centered at the burst position. The background was estimated using the reflected-region background model as described in Berge et al. (2007).

Two sets of analysis cuts were applied to search for a VHE γ-ray signal. These include standard cuts (Aharonian et al., 2006b) and soft cuts (with lower energy thresholds, as described in Aharonian et al. (2006a)[2]). Standard cuts are optimized for a source with a photon index of $\Gamma = 2.6$. Soft cuts are optimized for sources with steep spectra ($\Gamma = 5.0$), thus having a better sensitivity at lower energies. The latter is useful for a source at cosmological distances, since the EBL absorption would greatly soften the intrinsic spectrum of the VHE γ-ray radiation from the source. For observational periods with a position offset of 2.9°, a larger θ_{cut} value of 0.32° was used to accommodate the larger PSF. Energy thresholds (E_{th}) obtained for a standard cut analysis in each period

Table 6.1: H.E.S.S. observations at the burst position

date[a]	T_start[b]	Z.A.[c]	offset[d]	E_th[e]	f_UL[f] $(> E_\mathrm{th})$	f_UL[f] $(> 1\ \mathrm{TeV})$
2	22:03:37	23.3	2.5	540	4.2 (7 %)	1.6
2	22:33:48	16.5	2.5	540	11 (19 %)	4.0
2	23:04:10	9.9	2.9	1170	5.5 (31 %)	7.1
2	23:34:10	3.7	2.9	1060	3.3 (16 %)	3.6
3	00:04:38	4.8	2.1	240	20 (11 %)	2.0
3	00:34:38	10.6	2.1	260	5.2 (3 %)	0.61
3	01:04:50	16.2	1.3	240	8.8 (5 %)	0.91
3	01:22:02	22.1	0.5	280	6.1 (4 %)	0.81
3	02:03:02	31.6	0.5	320	7.4 (6 %)	1.2
3	02:33:28	38.3	0.5	460	5.8 (8 %)	1.7
3	03:03:52	45.1	0.5	600	5.5 (11 %)	2.4
3	23:17:39	7.4	1.0	220	11 (5 %)	0.97
3	23:47:36	4.8	1.0	220	4.6 (2 %)	0.41
4	00:17:46	8.5	1.3	240	9 (5 %)	0.93
4	00:47:46	14.9	1.3	240	12 (6 %)	1.2
4	23:41:41	4.5	1.2	220	9.3 (4 %)	0.83
5	00:12:13	8.9	0.6	220	7 (3 %)	0.60
5	00:42:12	15.1	0.6	240	8.4 (4 %)	2.3
5	01:12:27	22.9	1.1	290	13 (9 %)	1.8
6	00:36:42	15.0	0.4	240	15 (8 %)	1.5
6	01:06:48	21.5	0.4	260	9.1 (5 %)	1.1

[a]Date in 2006 June

[b]Start time of the observation in UT. All but the seventh observation run, which has an exposure of 14 minutes, have an exposure time of 28 minutes.

[c]Mean zenith angle of the observation run in degrees.

[d]Offset of the burst position from the center of the FoV in degrees.

[e]Energy threshold for a standard cut analysis in GeV.

[f]99 % flux upper limit for a standard cut analysis in 10^{-12} photons cm^{-2} s^{-1}, assuming a photon spectral index of 2.6, where numerals in brackets indicate the fractional flux in Crab unit above the same threshold
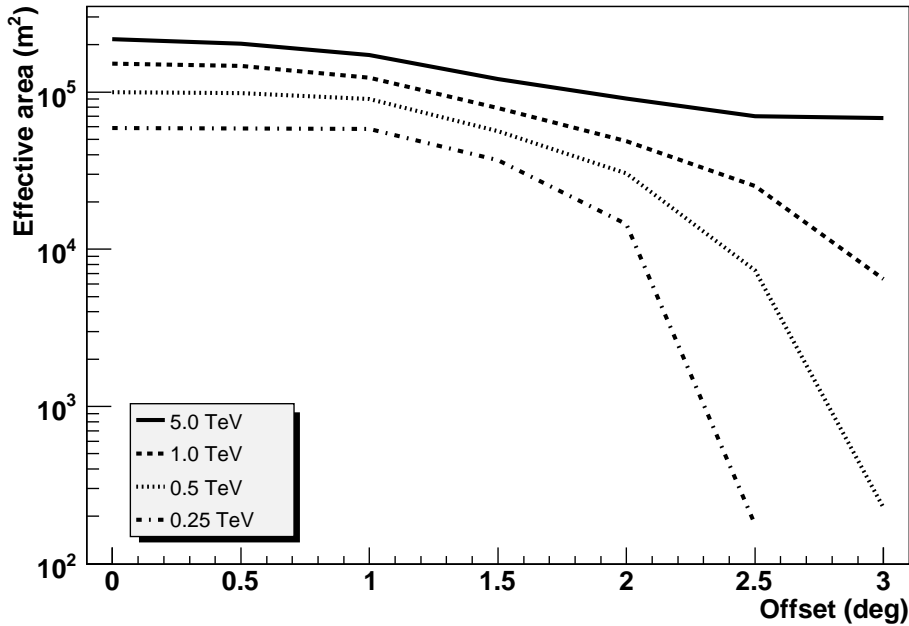
Figure 6.3: The effective areas for various photon energies at offsets from $0°$ to $3°$ from the center of the FoV for Z.A.$= 0°$, using the standard cut analysis used in this work

are shown in Table 6.1.

Figure 6.1 shows the rate of γ-like events (i.e. those that passed standard cuts) observed within a circular region of radius $\theta_{\text{cut}} = 0.32°$ (for $t < t_0 + 500\text{s}$) and $\theta_{\text{cut}} = 0.11°$ (for $t > t_0 + 600\text{s}$) centered at the source.

The independent *Model* analysis technique (de Naurois, 2005) was used to analyze the same data. The results obtained from both analyses are consistent with each other. Hence, only the analysis results based on Hillas parameters are presented in this paper.

6.5   Results

No evidence for excess γ-ray events was found at any time before, during, or after the event GRB 060602B. A *Crab-like* photon spectral index of 2.6 is assumed when deriving the flux limits presented in this section. The 99% confidence level flux upper limits obtained by the method of Feldman & Cousins (1998) for every observation run using standard cuts are included in Table 6.1. Figure 6.4 shows the 99% energy flux upper limits above 1 TeV during the *prompt* and *afterglow* phases up to 4 nights after the burst. The energy flux limit (>1 TeV) for the *prompt* phase of GRB 060602B is $2.9 \times 10^{-9}\,\text{erg cm}^{-2}\,\text{s}^{-1}$. The limits for the period $\sim 10^2 - 10^4$s after the burst are at levels comparable to the X-ray energy flux as observed by *Swift*/XRT during the same period. These limits are not very sensitive to the assumed photon spectral index (within a factor of 2 when changing the

---

[2] *Soft cuts* were called *spectrum cuts* in Aharonian et al. (2006a).
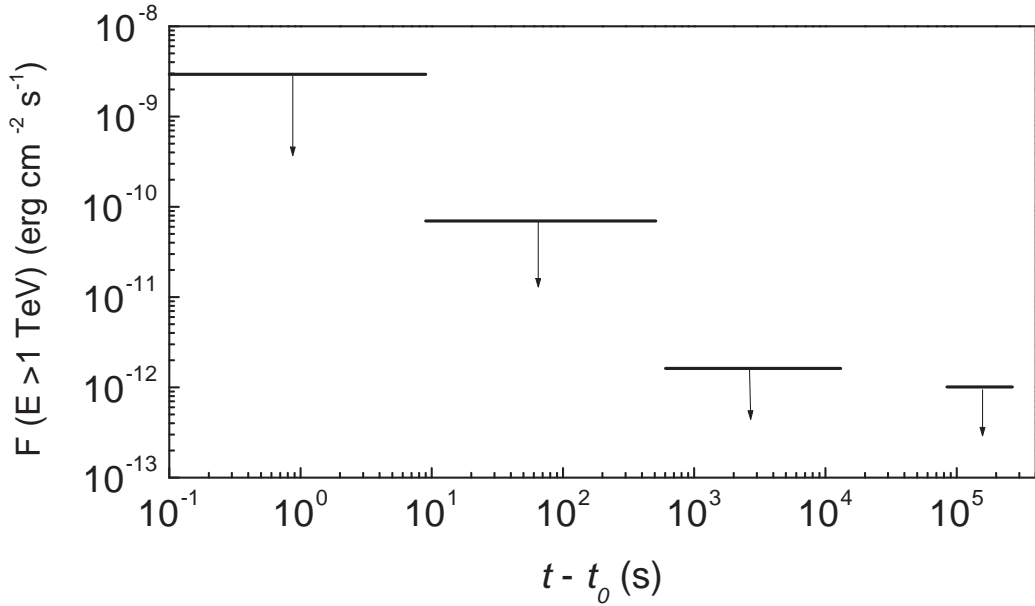
Figure 6.4: The 99% confidence level flux upper limits at energies $> 1\,\mathrm{TeV}$ derived from H.E.S.S. observations at the position of GRB 060602B during the *prompt* and *afterglow* phases. The two ends of the horizontal lines indicate the start time and the end time of the observations from which the upper limits were derived.

index to 2 or 4).

H.E.S.S. observations from 2004 to 2006 covering the position of GRB 060602B are used to constrain the time averaged emission from this object. No signal was found in the 128 hours of available data, of which more than 80% were taken before the burst. Assuming constant emission, a 99% flux upper limit (using standard cuts) of $9.0 \times 10^{-13}\,\mathrm{erg\,cm^{-2}\,s^{-1}}$ above 200 GeV (about 0.5% of the Crab flux) was found. This result is relevant for the Galactic scenario discussed in Section 6.6.2.

Figure 6.2 shows the spectral energy distribution of the burst during the first 9 s, and during the period $t_0 + 100\,\mathrm{s}$ to $11.4\,\mathrm{ks}$ (~ 3 hours) after the burst onset. It can be seen that the VHE energy fluence limits are of the similar level as the fluence at keV energies measured by *Swift* for both the 9-s *prompt* and 3-hour *afterglow* phases. Due to the soft keV spectra, any radiation in the VHE range would very likely come from a high-energy component separated from that of the sub-MeV radiation.

6.6   Discussion

The nature of GRB 060602B is unclear. The softness of the BAT spectrum and the proximity of GRB 060602B to the Galactic center suggest a possible Galactic origin of

the event. The observed temperature of $\sim$1 keV (using an absorbed blackbody fit) using XRT data is within the range seen from type-I X-ray bursts (Kuulkers et al., 2003). The *Swift*/BAT team has consequently classified the event as an X-ray burst (Barthelmy, 2007). Halpern (2006) noted that a faint source had been visible in an *XMM-Newton* observation taken in the neighborhood of the GRB 060602B position. Two other *XMM-Newton* observations were performed almost four months after the burst and a faint source was detected. The position of the faint source is marginally consistent with the *Swift*/XRT position of GRB 060602B, within the large positional errors (up to 4″, Wijnands et al., 2008). However, no indication of variability of the source was seen and no secure spatial association of the source with GRB 060602B was established.

Although a Galactic origin is more likely, the possibility of the GRB as a cosmological GRB is not ruled out. In this section, we briefly discuss the implications of the H.E.S.S. observations according to these two scenarios.

6.6.1 Implications for the cosmological gamma-ray burst scenario

HE γ-ray emission have been detected in the *prompt* and/or *afterglow* phases of several GRBs (Hurley et al., 1994; González et al., 2003; Kaneko et al., 2008). In these cases, no evidence for a high-energy cut-off was seen. The temporal evolution of the HE emission of GRB 941017 was found to be significantly different from its low-energy γ-ray light curve (González et al., 2003). For GRB 970417A, if the excess events observed by Milagrito were actually associated with the burst, the photon energy must be at least 650 GeV and the VHE γ-ray energy fluence must be at least an order of magnitude higher than the 50–300 keV energy fluence as seen by BATSE (Atkins et al., 2003).

In the VHE regime, possible radiation mechanisms include leptonic scenarios: external-shock accelerated electrons up-scattering self-emitted photons (Dermer et al., 2000; Zhang & Mészáros, 2001b) or photons from other shocked regions (Wang et al., 2001, 2006), and hadronic scenarios: proton synchrotron emission (Böttcher & Dermer, 1998; Totani, 1998a,b) or cascades initiated by π^0 produced via photo-meson interactions (Böttcher & Dermer, 1998; Waxman & Bahcall, 2000). In leptonic models, one typically expects a positive correlation between X-ray flux and VHE γ-ray flux. We note that the X-ray emission as seen by XRT decayed quickly, so one might expect the strongest VHE γ-ray emission to occur during the *prompt* phase or soon after. In fact, during the *early afterglow* phase, some authors predict VHE γ-ray energy flux levels comparable to or even higher than those in X-rays (Wang et al., 2001; Pe'er & Waxman, 2005).

The energy threshold of the H.E.S.S. observations was about 1 TeV and 250 GeV during the *prompt* and *afterglow* phases, respectively. For a cosmological GRB, VHE γ-ray radiation is attenuated by the EBL. The optical depth, τ, of the EBL absorption for a 1 TeV and 250 GeV photon is about unity at $z = 0.1$ and 0.3, respectively (Aharonian et al., 2006d). Therefore, if GRB 060602B occurred at $z \lesssim 0.2$, EBL absorption could be neglected. Under this assumption, the H.E.S.S. flux limits would exclude an intrinsic VHE γ-ray *prompt* and *afterglow* energy fluence much higher than that at sub-MeV energies (see Figure 6.2). Also, a VHE γ-ray fluence level such as the one implied by the possible

γ-ray events associated with GRB 970417A would be excluded for GRB 060602B. And the upper limits would constrain models which predict VHE γ-ray energy flux levels higher than those in X-rays during $\sim 10^2 - 10^4$s after the burst. If, however, GRB 060602B occurred at $z \gtrsim 0.2$, EBL absorption would be more severe and the observed limits would have to be increased by a factor which depends both on the redshift and the detailed gamma-ray spectrum of the GRB. In this case, the limits would be less constraining.

6.6.2 Implications for the Galactic X-ray binary scenario

X-ray binaries have been suspected to be VHE γ-ray emitters for decades, see, e.g. the review by Weekes (1992), and have recently been confirmed for at least three cases (Aharonian et al., 2005b, 2006c; Albert et al., 2006b).

Type-I X-ray bursts, originating from low-mass X-ray binaries (LMXBs) and with typical duration of 10 s up to several minutes, are caused by thermonuclear flashes on the surface of accreting neutron stars[3] (Lewin et al., 1993). Although most X-ray bursts are detected from known X-ray sources or transients, some X-ray bursts originated from the so-called *burst-only* sources, whose quiescent X-ray luminosity is too low to be detected by current X-ray detectors (Cornelisse et al., 2004).

Based on the BAT spectrum of the burst and the possible identification of a faint *XMM-Newton* X-ray counterpart, Wijnands et al. (2008) prefer the type-I X-ray burst scenario. In this case, the source might have been active in X-rays before the BAT trigger, although there was no detection with the *RXTE*/ASM before the burst (Wijnands et al., 2008). The GRB 060602B position had been in the FoV of H.E.S.S. for $\sim$2 hours when BAT triggered the event. No significant VHE γ-ray emission was observed during this period. If this scenario is true, the H.E.S.S. observations rule out that this X-ray burst was accompanied by a VHE γ-ray burst of similar energy flux. To our knowledge, no simultaneous VHE γ-ray observation of a type-I X-ray burst has been reported. Aharonian et al. (1998) reported a tentative evidence of a possible TeV burst emission with HEGRA during radio/X-ray outbursts (on a scale of days) of the microquasar GRS 1915+105, which is a LMXB listed in Liu et al. (2001).

Persistent VHE γ-ray emission from LMXBs containing a neutron star was predicted (Király & Mészáros, 1988; Cheng & Ruderman, 1991). For example, particles can be accelerated in the vicinity of accreting neutron stars, giving rise to VHE γ-ray emission through interactions of ultra-high-energy nuclei with surrounding material. No steady VHE γ-ray emission of the progenitor of GRB 060602B was obtained from our long-term data. More than a dozen LMXBs (including GRS 1915+105) and several high-mass X-ray binaries have also been observed with H.E.S.S. and no detection was seen from any of them (Dickinson et al., 2008).

---

[3]This process was proposed to explain the origin of GRBs (see, e.g. Hameury et al., 1982; Woosley & Wallace, 1982).

6.7 Conclusions

On 2006 June 2, the first completely simultaneous observations of a γ-ray burst (GRB 060602B) in hard X-rays and in VHE γ-rays with an IACT instrument were obtained.

The burst position was observed with H.E.S.S. at VHE energies before, during, and after the burst. A search for a VHE γ-ray signal coincident with the burst event, as well as before and after the burst, yielded no positive result. The 99% confidence level flux upper limit (>1 TeV) for the prompt phase of GRB 060602B is $2.9 \times 10^{-9}\,\mathrm{erg\,cm^{-2}\,s^{-1}}$.

The nature of GRB 060602B is not yet clear, although a Galactic origin seems to be more likely. The complete and simultaneous coverage of the burst with an IACT instrument operating at VHE energies places constraints either in the Galactic X-ray binary scenario or the cosmological GRB scenario.

6.8 On observations at large offsets

The above results highlights the feasibility of an observation, using an array of IACTs, in an extreme experimental condition, i.e. $\sim 3°$ offset from the center of the FoV. In this section, observations of a transient event at the 'edge' of the FoV of the instrument is discussed. For the purpose here, the 'edge' of the FoV refers to the region with a distance of $\sim 2.5°–3.0°$ to the center of the FoV.

6.8.1 Rate of Occurrence

Simultaneous observations of high energy transient lasting only for seconds using an IACT instrument, such as the one happened for GRB 060602B, are rare. For H.E.S.S. which currently has one of the largest camera FoV ($\sim 5°$) among other IACTs (see Figure 2 in Hinton, 2008), the chance probability of capturing such kind of transients within $3°$ radius from the center of the camera FoV at any instant during an observation is

$$P = (\text{sky fraction of the FoV}) \times (\text{occurrence rate of such kind of transients}) \times (\text{duration of a transient}) \tag{6.1}$$

Assuming that such kind of transients occur once per day and the duration of each transient is ~ 10 seconds, one obtains

$$
\begin{aligned}
P &= \left(\frac{(3°)^2 \pi}{4\pi} \right) \left(\frac{10\,\mathrm{s}}{1\,\mathrm{day}} \right) \\
&\approx 8 \times 10^{-8}.
\end{aligned}
\tag{6.2}
$$

For an instrument like H.E.S.S. which has been operating for ≈ 5 years with an average of 1000 hours of observation hours per year, the chance probability of such an occasion happening at least once approaches one.

6.8.2 prospects of large-offset observations

In the stereoscopic technique, i.e. images from at least two telescopes are used to reconstruct the event directions. Consider a shower initiated by a γ-ray event or a cosmic ray
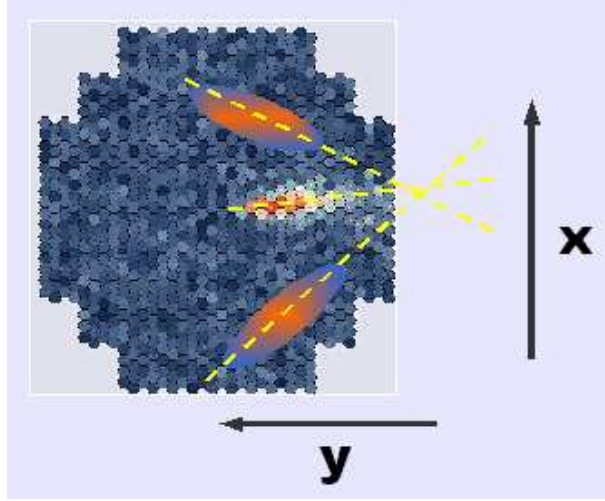
Figure 6.5: An illustrative example of direction reconstruction of a large offset event at the *edge of the FoV*.

event coming from a direction just outside the camera FoV of ∼5° (e.g. 'edge' of the FoV as specified above). This event may be observable by the array because of the observation technique employed for the IACTs, where images of Cherenkov light from the air showers of the incoming γ-ray/cosmic-ray, instead of the γ-ray/cosmic-ray itself, are recorded by the array system. The shower image may be visible in the camera's physical FoV. Figure 6.5 illustrates the shower image recorded by one of the four H.E.S.S. cameras, which is made of 960 PMTs. The two ellipses are added artificially to illustrate the principle of direction reconstruction. Each of them represents the shower images from two other cameras. The yellow dashed lines indicates the reconstruction direction of the shower direction based on each of the three camera images.

Geometrical effects, such as fewer air shower images available in direction reconstruction and that most air showers are coming from only one side of the source position (corresponding to the positive y-direction as seen in Figure 6.5), may contribute to worsen the accuracy of the direction reconstruction for large-offset positions. As seen in Figure 6.5, the direction reconstruction in the x-direction would be better than that in the y-direction. In turn, the point spread function (PSF) at a 3° offset position is more extended than that for an offset of, e.g. < 2°.

Effective areas at 3° offset for different photon energies are shown in the upper panel of Figure 6.6. A zenith angle of zero degree and a photon spectral index of 2 of a factitious source is assumed in the simulation. The effective area increases from $10^3 \, \mathrm{m}^2$ at 600 GeV to more than $10^5 \, \mathrm{m}^2$ at energies > 15 TeV. The lower panel of Figure 6.6 shows the differential γ-ray rate plotted against photon energy. The peak of this curve, which is located at ∼3 TeV, defines the energy threshold. By this definition, a steeper spectrum (e.g. $\Gamma = 3$) gives a smaller energy threshold.

To briefly summarize the above discussion, it is demonstrated that the H.E.S.S. instrument has certain sensitivity outside the nominal camera's FoV of ∼2.5°. For comparison, even at such a large offset of ∼3° from the center of the camera FoV, the upper limit

Figure 6.6: Upper panel: Effective area at 3° offset versus photon energy from MC data. Standard analysis cuts were used to select γ-like events. A larger θ_{cut} value of 0.32° was used to accommodate the larger PSF at this offset. Lower panel: Differential γ-ray rate plotted against photon energy. The peak-rate energy threshold is located at $\sim$3 TeV.
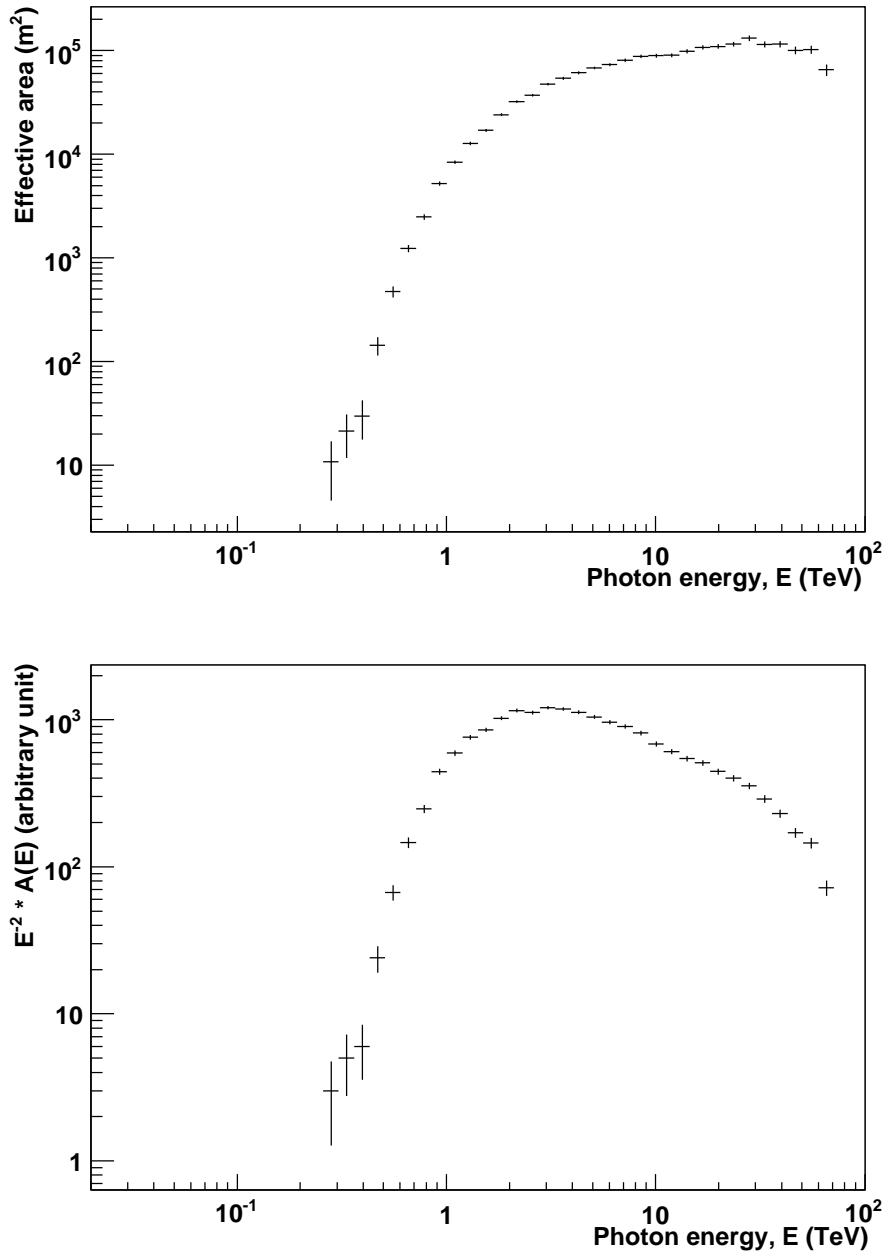
obtained for the prompt emission at VHE energies for the case of GRB 060602B (see section 6.5) is about an order of magnitude more stringent than an average upper limit obtained for the observations of GRBs using the all-sky Milagro detector (c.f. Atkins et al., 2005).

6.8.3 Relative photon acceptance and effective field of view

As discussed above, unlike an optical or X-ray telescope, there is no sharp boundary outside which no photons can be recorded. An important parameter here is the *relative photon acceptance* at different offsets from the center of the FoV. It is the ratio of the number of photons accepted when a γ-ray source (e.g. the Crab Nebula) is placed at a certain offset from the center of the FoV to the number of photons accepted when the same source is placed at the center of the FoV. In general, this radio is different from the radial relative acceptance of cosmic-ray background (c.f. Figure 8 in Aharonian et al., 2006b).

The relative acceptance depends on the photon energy. At $\sim2.5°$ offset from the center of the FoV, the relative gamma-ray acceptance increases from about 0.7% for a 250 GeV photon to about 15% for a 1 TeV photon. Concerning the observations of the prompt phase of GRB 060602B, the relative gamma acceptance at $2°.9$ offset is $\sim5\%$ for a 1 TeV photon.

Using the effective areas derived from MC data (for offsets $0°$, $0°.5$, $1°.0$, $1°.5$, $2°.0$, $2°.5$, $3°.0$) at ZA= $0°$ and the usual interpolation procedure (for getting the effective areas at offsets in between), the relative acceptance is obtained by dividing the effective area at a certain offset by that at the center of the FoV. The relative acceptance drops below a certain value (e.g., 50%, 20%, 5%, and 1%) at a certain offset from the center of the FoV. This offset can be regarded as the radius of the *effective* FoV and is shown in Figure 6.7 for different photon energies. It should be cautioned that errors are not included in plotting this figure. Sources of errors include systematic errors of an order of 0.1 degree (which may arise from, e.g. the interpolation procedure) and statistical errors arising from the finite number of MC data, especially at large offsets.

6.9 On the nature of GRB 060602B

While the fluence and the duration of GRB 060602B are consistent with it being a GRB or an X-ray burst, the following considerations are based on its sky location, spectral properties, and counterpart search.

Sky location

The galactic coordinates of the source are $(l,\ b) = (1°.15, -0°.30)$. This position supports a galactic origin of the event, since LMXBs, believed to be the progenitors of X-ray bursts, concentrate strongly toward the galactic bulge of our galaxy. On the other hand, if GRB 060602B were a cosmological GRB, it would be one which happened to be to the direction next to the galactic center.
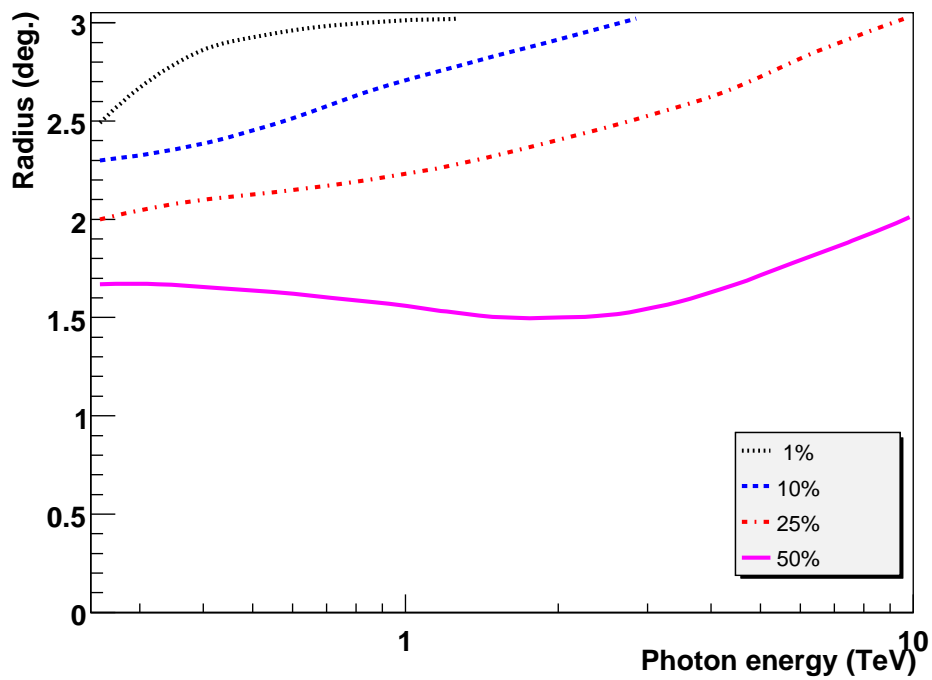
Figure 6.7: Radius of the *effective* FoV (in degrees) of the H.E.S.S. array versus the photon energy. The relative acceptance drops below a certain value (50%, 20%, 5%, and 1%) at an offset from the center of the FoV, this offset is then defined as the radius of the *effective* FoV. Errors are not included in plotting this figure.

Counterpart search

The galactic location means that the field around GRB 060602B is likely to be crowded. In the proximity of the *Swift*/XRT position of GRB 060602B, a faint XMM-Newton source was detected on September 23, 2000, as first noticed by Halpern (2006). It is listed in the second XMMSSC-XMM-Newton Serendipitous Source Catalog as located at R.A. $= 17^\mathrm{h}49^\mathrm{m}31\overset{\mathrm{s}}{.}685$, Dec. $= -28°08'06\overset{''}{.}92$ with an error of $1\overset{''}{.}08$ (statistics) $+0\overset{''}{.}5$ (systematics), i.e. about $4''$ from the GRB 060602B XRT position, with a flux of $(2.33 \pm 0.35) \times 10^{-13}\mathrm{erg\,cm^{-2}\,s^{-1}}$ in the 0.2–12 keV range (Watson et al., 2008). Assuming a distance of 8 kpc, the luminosity of this source is $\sim 1.7 \times 10^{33}\mathrm{erg\,s^{-1}}$, consistent with the level of quiescent LMXBs. However, the association of this source with GRB 060602B event has not been established.

Temporal properties

The left panel of Figure 6.8 shows the *Swift*/BAT raw photon count rate in the 15–150 keV range. The largest spike at $\sim t_0 + 6$s has a peak photon flux of $0.8 \pm 0.1\ \mathrm{cm^{-2}\ s^{-1}}$ (Palmer et al., 2006a). The fast-rise-exponential-decay (FRED) shape resembles the light curve of a typical X-ray burst and also many of typical GRBs.

Swift/XRT started observations from 83 seconds after the BAT trigger. The 0.3–10 keV flux decayed more than an order of magnitude in less than a day.

Spectral properties

The BAT spectrum in the 15–150 keV band can be fitted using a power-law with a photon index of $\Gamma = 5.0 \pm 0.52$ (Palmer et al., 2006a). The very soft spectrum of GRB 060602B suggests that the spectrum actually peaks at X-ray energies. Fitting the spectrum with a blackbody model, Wijnands et al. (2008) obtained a temperature of $\sim$3 keV (see the right panel of Figure 6.8). Softening of its spectrum with time, a typical behavior observed both in GRBs *and* X-ray bursts, is not seen, but cannot be ruled out because of the limited photon statistics (Wijnands et al., 2008).

As already described in section 6.2, a blackbody model and a power-law model both fit the average XRT spectra equally well. The temporally resolved spectra seem to indicate a thermal to non-thermal transition around $t_0 + 550$ s (Wijnands et al., 2008). As shown in Figure 6.9, the X-ray spectrum may have undergone a hardening over time. Although albeit with large uncertainties in fitting parameters due to limited statistics, this behavior is atypical in both GRB and X-ray burst scenario.

6.9.1   Is GRB 060602B an X-ray burst?

Although mainly built for observing GRBs, *Swift*/BAT also triggers on X-ray bursts, whose energy is mostly released in the X-ray band and in most cases $E_\mathrm{peak} < 10$ keV. In two reported occasions, namely BAT trigger numbers 223918 (Romano et al., 2006) and 318166 (Sakamoto et al., 2008b), the triggers are believed to be X-ray bursts, based on their very soft BAT spectrum *and* the positional coincidence of the established X-ray bursters. See Kong (2006) and Linares et al. (2008), respectively. In fact, there is
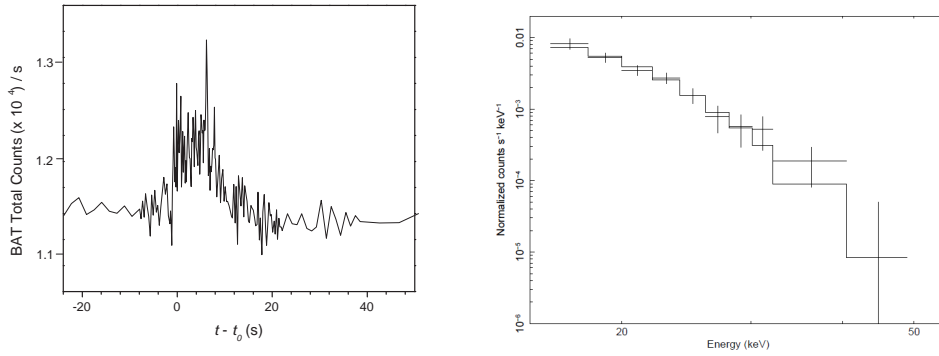
Figure 6.8: *Left panel*: *Swift*/BAT photon count rate. *Right panel*: *Swift*/BAT spectral data overlayed with the best fit blackbody model (solid line, Wijnands et al., 2008). An equally well-fit power-law model gives a photon index $\Gamma \approx 5$.
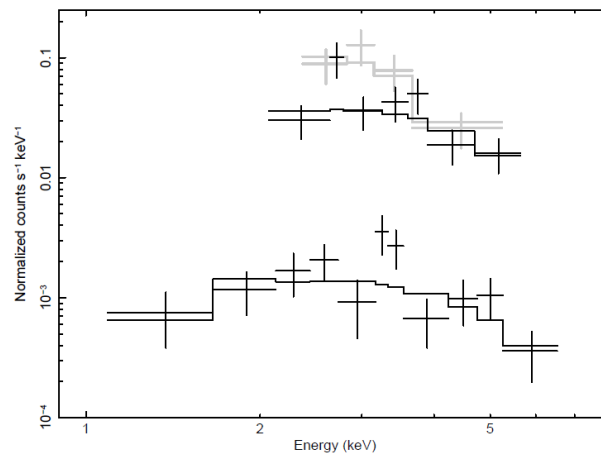
Figure 6.9: *Swift*/XRT spectral data during the delayed time intervals after the burst: $\sim 90 - 300$s (grey), $\sim 550 - 1200$s (upper black), and the rest up to ~ 50ks (lower black). Solid lines are fit models (from Wijnands et al., 2008).

Trigger number	Photon index Γ (power-law fit)	Activity above 25 keV	Source
223918	5.4 ± 0.54	N	1A 1246-588
318166	4.1 ± 0.67	N	XTE J1701-407
213190 (=GRB 060602B)	5.0 ± 0.52	Y	unidentified (see text)

Table 6.2: A comparison of three *Swift*/BAT triggers possibly caused by type-I X-ray bursts, including GRB 060602B. The photon indexes are taken from an online repository, http://gcn.gsfc.nasa.gov/notices_s/223918/BA, http://gcn.gsfc.nasa.gov/notices_s/318166/BA, and Schady et al. (2006, for GRB 060602B).

no activity seen at energies above 25 keV in these two cases. A comparison of simple power-law fit of the BAT spectra of these two events and their known hosts with those of GRB 060602B is shown in Table 6.2. It should be noted that there may be other *Swift*/BAT-triggered X-ray bursts which are unnoticed and are therefore not included here.

6.9.2   Is GRB 060602B an X-ray flash?

The very soft spectrum (photon index $\Gamma = 5.0 \pm 0.52$ and $E_{\mathrm{peak}} < 15$ keV) of GRB 060602B places it clearly as an outlier among typical GRBs. For comparison, the mean Γ of a large sample of other *Swift* GRBs is 1.68, and the softest one, GRB 050416A, which is classified as an X-ray flash, has $\Gamma = 3.1 \pm 0.2$ (Sakamoto et al., 2008c, see also Figure 13 of Sakamoto et al. (2008a)). X-ray flashes (XRFs), closely related to GRBs, have a larger energy fluence in the X-ray band than in the γ-ray band. This naturally raises a question: can GRB 060602B be an X-ray flash?

XRFs are bright X-ray transients with duration $< 10^3$ s (Heise et al., 2001). The fact that the population of XRFs form a continuum with GRBs in almost every aspect (e.g. Figure 2 in Sakamoto et al., 2005) strongly suggests a similar physical origin between these two phenomena. XRFs mimic GRBs in many ways but with much softer emission. Nine out of 16 XRFs in the HETE-II sample have $E_{\mathrm{peak}} < 20$ keV (Sakamoto et al., 2005). Unlike X-ray bursts which exhibit a blackbody spectrum, many XRFs are well fitted by the Band function, similar to GRBs. Based on the hardness ratio between the fluence in the 25–50 keV ($S_{25-50\,\mathrm{keV}}$) and the 50–100 keV band ($S_{50-100\,\mathrm{keV}}$), Sakamoto et al. (2005) define XRFs as those GRBs having $S_{25-50\,\mathrm{keV}}/S_{50-100\,\mathrm{keV}} > 1$ and found 10 XRFs in the $\approx$2-year's GRB sample. Figure 6.10 shows the photon indices as obtained from simple power-law fits of these XRFs, as well as their hardness ratio versus energy fluence in the 15–150 keV energy band. In both cases, the datum of GRB 060602B is also plotted for comparison. These results show that GRB 060602B may also be an outlier among other XRFs, thus may indeed has a different physical origin. Based on a search of very soft events in the BATSE database, Tikhomirova et al. (2006) point out that a photon index of $\Gamma > 3$ may be a distinguishing feature of non-GRB events.
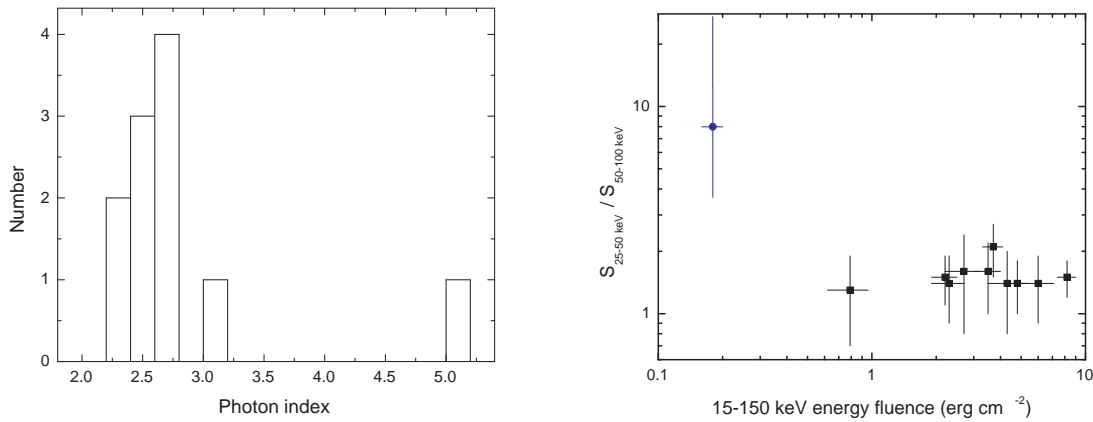
Figure 6.10: *Left*: Photon indices as obtained from simple power-law fits to the *Swift*/BAT XRFs presented in Sakamoto et al. (2008c). The rightmost one is for GRB 060602B. *Right*: Hardness ratio against energy fluence in the BAT 15–150 keV energy band, from the same XRF sample. The datum shown in blue circle represents GRB 060602B, the hardness ratio of which was derived using the data from the page http://gcn.gsfc.nasa.gov/notices_s/213190/BA on September 2, 2008.

6.9.3   Simultaneous VHE γ-ray observations of X-ray bursts

In order to understand the significance of the simultaneous observation of GRB 060602B, it may be helpful to see whether such simultaneous observation in the VHE γ-ray band of X-ray bursts has ever existed. Although no such observation has been reported, I have looked into the whole H.E.S.S. database and see whether this has happened. Two large samples of triggers on X-ray bursts since 2004 were used to search for such a coincidence. They are the INTEGRAL/IBIS sample (Chelovekov et al., 2006, expanded in Chelovekov et al. (2007)) and the RXTE sample (Galloway et al., 2008). Two INTEGRAL/IBIS bursts were found to fall serendipitously into the FoV of the H.E.S.S. camera when they occurred. They are associated with two known X-ray bursters KS 1741-293 and SLX 1744-299. Figure 6.11 shows these two bursts as detected in the 15–25 keV band of IBIS. The burst properties and the associated H.E.S.S. observations and results are presented in Table 6.3. The H.E.S.S. flux limits were derived using the time interval of the duration of the burst centered at the burst maximum. Standard cuts with $\theta_{\rm cut} = 0.11°$ are used in the analysis and background estimation was made using the reflected region background model.

The ambiguity of the nature of GRB 060602B is not a unique situation. The identification of the galactic or extragalactic origin of some bursts in the γ-ray energies is not trivial. For example, a "fast X-ray transient source" (designated SAX J0840.7+2248) was detected with BeppoSAX on April 29, 1998 (Heise & in 't Zand, 1998) and was subsequently classified as a *burst-only* LMXB. However, later observations with *Swift*/XRT of the position and refined analysis of the 1998 burst showed that the burst was actually
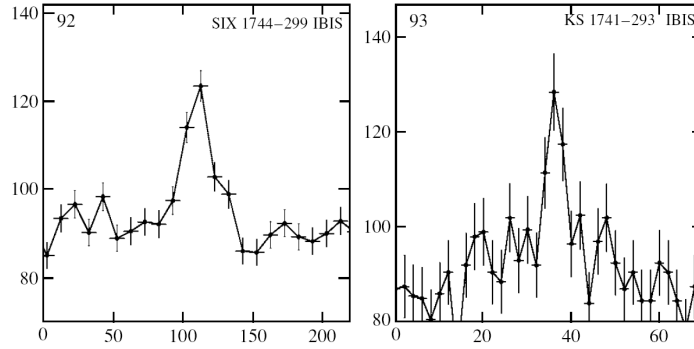
Figure 6.11: The count rate (per second; y-axis) plotted against time (seconds, arbitrary starting time; x-axis) during the X-ray bursts from SLX 1744-299 and KS 1741-293, as seen in IBIS/ISGRI detector on board INTEGRAL (from Chelovekov et al., 2006). The numbers in the upper left corners of each plot indicate the burst number in the sample presented in the above reference.

Table 6.3: The two X-ray bursts triggered by INTEGRAL/IBIS with simultaneous H.E.S.S. observations at March 30, 2004

	Burst properties			H.E.S.S. observations				
source	time[a]	flux	duration	Z.A.	offset[b]	E_{th}	flux upper limit[c]	
		(Crab unit)	(s)	(deg)	(deg)	(GeV)	$(> E_{th})$	$(> 1\ \mathrm{TeV})$
SLX 1744-299	03:37:46	0.81	22	10.7	1.8	170	56 (1.8)	3.4 (1.5)
KS 1741-293	03:43:45	0.88	7	9.7	1.0	170	84 (2.7)	5.0 (2.2)

[a]Time of the burst maximum

[b]Offset of the burst position from the center of the FoV.

[c]99 % flux upper limit for a standard cut analysis in 10^{-11} photons cm^{-2} s^{-1}, assuming a photon spectral index of 2.6, where numerals in brackets indicate the flux in Crab unit above the same threshold

an X-ray rich GRB (Romano et al., 2008). On the other hand, the *Swift*/BAT triggered GRB 070610, with a duration and spectral properties (e.g. hardness ratio) typical of other *Swift* GRBs, was subsequently identified as a galactic transient using optical and X-ray data by Kasliwal et al. (2008).

Therefore, there is hope that the nature of GRB 060602B will become clearer in the future.

Chapter 7

GRB science of the next generation Cherenkov array

This chapter was submitted as a GRB science proposal for the Cherenkov Telescope Array (CTA) – a next generation Cherenkov array – in June 2008.

7.1 Introduction

A gamma-ray burst (GRB) is the most intense soft gamma-ray source on the sky for a short period of time lasting 0.01 second to several hundred of seconds. GRBs are among the potential extragalactic sources to emit VHE gamma-rays. Exploring this highest photon energy regime is necessary to fully understand the energetics and properties of GRBs. Once detected, VHE emission from GRBs can have strong implications for GRB models and possibly cosmic-ray origin.

7.2 Current status of VHE observations of GRBs

Prompt and follow-up observations of GRBs at VHE energies make use of several types of instruments. The first type is the air shower detectors, with MILAGRO as its most sensitive example. Being a water Cerenkov detector with a large field of view, it monitors the sky all the time for associated TeV emission from GRBs. No significant signal has been detected. The photon excess events from GRB 970417A using the MILAGRITO (the forerunner of MILAGRO) during the prompt phase is thrilling but not conclusive (Atkins et al., 2000). The upcoming HAWC detector will be ∼10 times more sensitive than MILAGRO. However, a big disadvantage of this type of detectors is their poor sensitivity and a high energy threshold (>1 TeV), thus a significant absorption of TeV photons by the extragalactic background light (EBL) is expected.

Atmospheric Cherenkov telescopes are more sensitive and working at lower energies. Using the Whipple telescope, the first serious search for VHE bursts was carried out in 1970s (Porter & Weekes, 1978). The second generation of Cherenkov telescopes, including MAGIC, H.E.S.S., and VERITAS, can reach a sensitivity of ∼3% Crab flux in a 2h observation. Remarkably, the MAGIC telescope, having a 17m diameter dish, slewed

to the GRB 050713A position 40s after the GRB onset, while the prompt emission was still active. The rapid follow-up observations using this telescope of 9 GRBs (including GRB 050713A) show no evidence of associated VHE gamma-ray emission during the prompt or the early afterglow phase Albert et al. (2007b). Searches in GRB data taken with other Cherenkov telescopes yielded similar results (Horan et al., 2007; Tam et al., 2008). The null detection of these observations does not exclude VHE Emission from GRBs as predicted in many GRB models, since the redshifts of a large fraction of the observed GRBs are either unknown or larger than 1.0, prohibiting a definite interpretation of these data.

7.3 Predicted VHE emission from GRBs

The fireball model is a widely accepted model to reproduce the general properties of GRBs (Piran, 1999). In the internal-external shock scenario, internal shocks (responsible for the prompt emission) occur at $R \sim 10^{12} - 10^{14}$cm from the progenitor, while external shock (responsible for the afterglow emission) form at $R \sim 10^{16} - 10^{17}$cm when the ejecta is decelerated by the surrounding medium. Independent of the radiation mechanisms involved, any VHE gamma-rays produced would suffer from internal gamma-gamma absorption before they escape from the source. The optical depth, τ, would be large in the internal shock region (if the bulk Lorentz factor $\Gamma < 10^3$) but a detection during the prompt phase would put a lower limit on Γ (Baring, 2006) and have strong implications to prompt emission models. τ is much lower in the external shock region.

A promising mechanism to produce VHE gamma-rays in the afterglow phase is the inverse-Compton (IC) scattering by the relativistic electrons accelerated in the external shock. The seed photons can be the synchrotron photons produced by the same electrons (SSC) or photons from other regions (EC, e.g. reverse shock region or central engine). The best time window to look for VHE gamma-ray signal might be the early-afterglow phase (starting ~10s after the burst), when both forward and reverse shocks (being two components of the external shock) are at work to accelerate particles to ultra-relativistic speeds (Wang et al., 2001; Pe'er & Waxman, 2005). One such model, involving contributions from both emitting regions by SSC processes is depicted in Figure 7.1. Afterwards, the IC component from the forward shock continues to contribute the VHE emission. An SSC forward-shock model is illustrated in Figure 7.2, where board band spectral energy distributions at 200 s, 2×10^4 s and 2×10^6 s after the burst are shown.

Apart from the VHE predictions described above, there may be further contribution to VHE flux from other channels, including the X-ray flare phenomenon. X-ray flares are found in more than 50% of the Swift GRBs during the afterglow phase. The energy fluence of some of them (e.g. GRB 050502B) is comparable to that of the prompt emission. The origin of the flares is still under debate. The accompanying EC flare may be weak (Fan et al., 2008) if the flare originated behind the external shock, e.g. from prolonged central engine activity. However, in the external shock model of X-ray flares, the expected SSC flare at GeV energies is very strong and can be readily detected, for a typical GRB of z~1, using a VHE instrument with an energy threshold of tens of GeV (Galli & Piro, 2008). Therefore, detection of an accompanying ~100 GeV flare or sensitive enough upper limits
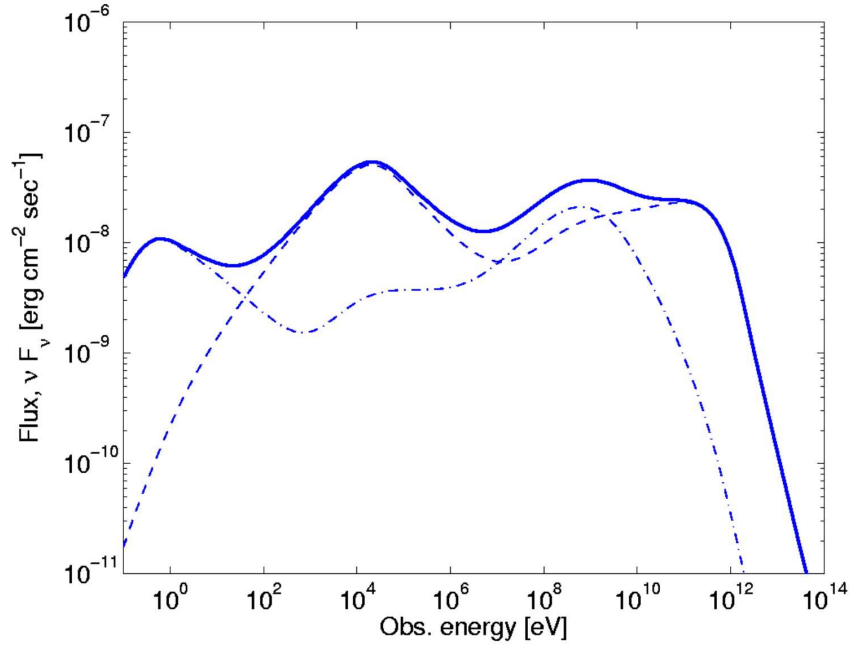
Figure 7.1: Predicted spectra for a GRB at $z = 1$ at 10 sec after the burst. Forward shock emission (dashed), reverse shock emission (dash-dotted) and total spectra (solid) are shown (from Pe'er & Waxman, 2005). Note that absorption due to EBL is not included in the spectra.
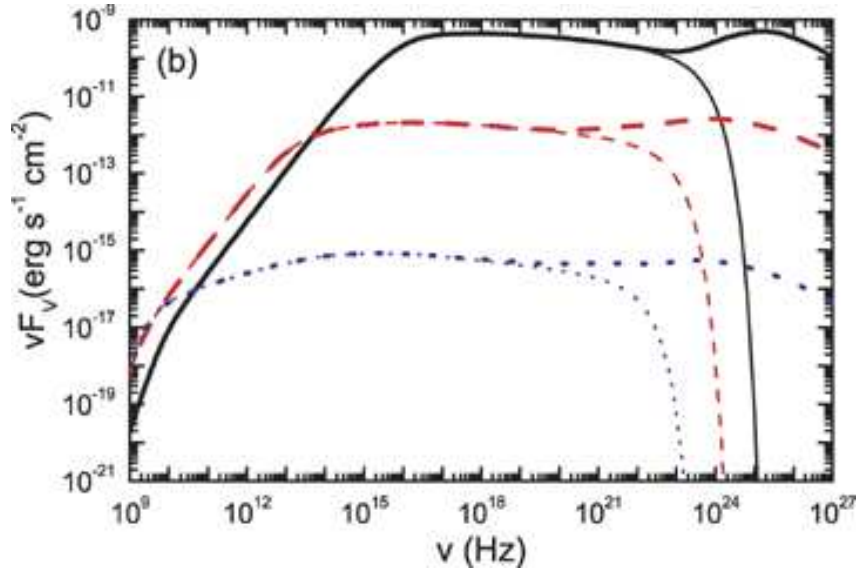
Figure 7.2: Board band spectra from the forward shock at 200 s (solid black), 2×10^4s (dashed red) and 2×10^6s (dotted blue) after the burst. Thin lines indicate the synchrotron component, while thick lines indicate the total spectra including the SSC component (from Fan et al., 2008). Note that absorption due to EBL is not included in the spectra.

of the flux at ~ 100 GeV during X-ray flares would be useful to test and constrain this model and may provide a diagnosis of the origin of X-ray flares, which in some models are originated from late central engine activities (e.g. Zhang et al., 2006).

Protons may also be accelerated together with the electrons. Although generally not expected to be as important as the IC emission, detection of VHE emission through the π_0-decay channel may have important implications of the origin of cosmic rays at the highest energies (Waxman, 2006). Even if they are detected, it seems difficult to differentiate the leptonic or hadronic origin of VHE photons through its spectrum alone, due to the imprints of pair production. Simultaneous detection of neutrinos with VHE gamma-rays would be the main signature of acceleration of protons or heavy nuclei in GRBs (Murase et al., 2008).

7.4   What can we learn from CTA?

As outlined above, in the framework of the standard fireball model, VHE gamma-rays from GRBs during the prompt to afterglow phases are expected. While prompt VHE emission (i.e. from internal shocks) may suffer from pair-production before they escape the source, VHE emission from IC scattering off forward-shock photons giving rise to afterglow or X-ray flare photons may offer the best opportunities to be detected by ground-based Cherenkov arrays. The current generation of IACTs, including MAGIC-I or -II and H.E.S.S.-I or II, may detect the first VHE photons from GRBs. However, a light curve (which requires a detection of several tens of photons) is probably desired to map out important GRB properties like Lorentz factors, location of emission, micro-physical shock parameters (ϵ_e, ϵ_B), and density of the surrounding medium. This seems not possible with the current instruments. The contribution from hadronic components should not be neglected since GRBs are one of a few potential sites able to accelerate protons and heavy nuclei to UHE energies (Murase et al., 2008; Asano et al., 2008).

To maximize the chance of detection for CTA, the following requirements are desirable. Firstly, the instrument has to react fast enough (e.g. on target anywhere on the sky in ~ 50 s). A slew rate similar to that of MAGIC would be desirable to probe the early-afterglow phase $\sim 10 - 100$ seconds after the trigger. Secondly, a low energy threshold of ~ 20 GeV is also needed to avoid an appreciable level of absorption due to EBL. Indeed, a ~ 20 GeV photon was detected using EGRET back in 1994, with its relatively small effective area (Hurley et al., 1994). Thirdly, a high sensitivity below 1 TeV (~ 10 times that of H.E.S.S.) is needed to be able to detect enough photons for temporal and spectral studies to gain knowledge on physical paramters in contemporary GRB models.

The effective area at ~ 50 GeV of CTA is much larger than LAT on board GLAST, which was successfully launched on June 11, 2008. While LAT is expected to detect photons at tens of GeV energies from a number of bursts like GRB 940217, there is a good chance for CTA to detect >10 photons at tens of GeV energies, if (a) the energy threshold of CTA is about 20 GeV, which is probably not achievable by MAGIC; and (b) the sensitivity of CTA at ~ 50 GeV is a few times that of the single 28-meter diameter telescope in the H.E.S.S.-II array. Stereo technique is required to achieve that. If these performances can be realized, CTA would be the most suitable instrument to observe

the highest end of a GRB spectrum, thus constraining GRB energetics and properties. Since the horizon of a $\sim$20 GeV photon is $z \sim 2$, EBL absorption is not a major obstacle anymore for a large fraction of all GRBs. These in turn have implications on GRB environment, progenitor models, and jet physics. On the other hand, detection of GRBs located at z$\sim$1 at $\sim 50 - 100$ GeV energies may probe the EBL shape at z>0.2 which is at the moment still uncertain.

Chapter 8

Concluding remarks

8.1 Summary of this thesis

A study of GRBs using VHE γ-ray observations is presented in this thesis. The current understanding of GRBs from γ-ray observations in various energy bands is reviewed in Chapter 1. Previous attempts to detect VHE emission from GRBs are summarized, where the first convincing case of detection has yet to accomplish.

Several important radiation mechanisms responsible for generating GRBs and the afterglows (including synchrotron emission and the SSC emission) are reviewed in Chapter 2. Predictions of VHE γ-ray emission under the current understanding of GRBs are presented. The general consensus is that VHE emission is expected in widely-discussed GRB models (e.g. the internal-external scenario) during the prompt[1] and the afterglow phases, for nearby GRBs to avoid severe EBL absorption. Some expectations are *natural* (e.g. an SSC component), i.e. they are based on leptonic emission models which can describe the most important observational facts of GRBs and their afterglows. It is intuitive to note that VHE emission has been detected from objects like blazars and supernova remnants after similar arguments were suggested. Other expectations do come from more speculative models, including radiation from accelerated protons, from which the expected VHE flux can even be higher.

These expectations have motivated the search of high-energy emission associated with GRBs using current VHE instruments. The launch of Swift satellite in 2004 and the operation of the H.E.S.S. array with unprecedent sensitivity have provided a strong experimental basis for this search. The H.E.S.S. GRB observing program is described in Chapter 3. The basic idea is to perform follow-up observations on the GRB positions distributed from satellites via the GCN network. Dedicated observations of a total of 34 GRBs have been performed since the H.E.S.S. experiment was started in 2003. After selecting those high-quality data, the data obtained from 21 GRB observations were analyzed. No significant detection was found. The results are presented in Chapter 4.

On 2006 June 2, the position of a *Swift*-triggered GRB fell serendipitously at the edge of the FoV of the H.E.S.S. cameras when the burst occurred. This results in the first completely simultaneous observation of a GRB using an IACT array. On the other hand,

---

[1]for those GRBs with high bulk Lorentz factor

the nature of the GRB has been in doubt. Although the burst is likely to be a Galactic event, the possibility of it being a cosmological GRB cannot be ruled out. The analysis methods, results, and implications are detailed in Chapter 6. Since the position was at an offset of ∼3° from the center of the camera FoV, special care was taken to analyze the data. This is also presented in Chapter 6.

Chapter 5 presents a calculation of the VHE afterglow emission based on an SSC model developed in Fan et al. (2008) of selected 6 low-redshift GRBs. A comparison of the modeled flux with VHE observational data, including those derived from H.E.S.S. observations of GRB 030329 and GRB 060505, was carried out. It was found that the modeled VHE fluxes are below the upper limits. However, it was argued that a VHE detection is possible even ∼10 hours after the GRB for those bright and nearby events like GRB 030329. Continuous VHE monitoring of GRB positions during the afterglow phase is encouraged to probe the current models. An emphasis on observations of those bright and nearby GRBs may provide stronger constraints in the future. Finally, a discussion on GRB science to be done with a planned IACT array — CTA is given in Chapter 7.

8.2   Future prospects

A large sample of upper limits through H.E.S.S. observations of the GRB afterglows, together with an upper limit of the prompt VHE γ-ray emission of GRB 060602B (the origin of which is disputed) is presented in this thesis. A critical parameter, namely the redshifts of the GRBs, is unknown in many cases. This prohibits a physical interpretation of the limits due to the EBL absorption. Therefore, successful redshift determinations of *these* GRBs (if possible, e.g., by searching for host galaxies) would be interesting to better constrain VHE emission from these GRBs. Redshift determinations of a large fraction of *future* GRBs are also highly encouraged. The same is true even if we had detected any emission. In the latter case (which may, however, happen in the future, as outlined above), the inability to translate the detected VHE flux to the knowledge of the intrinsic VHE emission would not be very helpful for our understanding of what happens in GRBs.

Some future prospects of VHE γ-ray emission from GRB are summarized below.

- Predictions of the 'intrinsic' VHE luminosity of GRBs differ in different models. Among various leptonic models, the highest VHE flux is predicted in the external shock model of GRBs and X-ray flares (Galli & Piro, 2008; Dermer, 2008). In this model, due to the much lower opacity of pair production at large distance from the inner engine, up-scattering of X-ray flare photons gives rise to a strong VHE flux which is within the sensitivity of *current* instruments. In the widely-discussed internal-external shock scenario (Piran, 1999), the best time window is the early-afterglow phase (∼10–100 seconds after the burst) — the onset of the external shock at which both reverse shock and forward shock components contribute to the VHE flux (Pe'er & Waxman, 2005). In contrast, Poynting flux-dominated GRB models would give rise to a very weak IC component, because of the high magnetic field density.

- The recent observations of the 'naked-eye' GRB 080319B have challenged a conventional view that prompt γ-ray emission is generated by synchrotron processes, at least for those GRBs with a high prompt optical emission. A simultaneous $\sim 10 - 100$ GeV burst from GRB 080319B due to the second-order IC component was suggested by Racusin et al. (2008) and Fan & Piran (2008). This highlights that optical observations are crucial to diagnose those GRBs generated by SSC processes from those by synchrotron emission. The H.E.S.S. site is also equipped with ROTSE IIIc and ATOM optical telescopes. If a similar event at $z \lesssim 1$ can be observed simultaneously in the optical and VHE γ-ray band, either a detection or upper limit of the VHE emission could constrain the radiation mechanisms of GRBs.

- Protons may accelerate to relativistic speeds in GRBs as well (Böttcher & Dermer, 1998; Waxman & Bahcall, 2000), although lacking of observational support to date. If most energy resides in protons so that $E_p \gg E_e$, a strong VHE emission is expected from these 'proton-dominated' GRBs (Totani, 1998a; Asano et al., 2008). This idea was suggested to explain the MILAGRITO burst (Totani, 1998b). The existence of such a population of 'proton-dominated' GRBs is allowed both in the parameter space of theories and by current observations. If these GRBs exist, they would have a significant impact on our understanding on the origin of UHECRs (e.g. Murase et al., 2008). Together with neutrino experiments, observations of GRBs at the highest energies are crucial to test these ideas.

- The EBL absorption of VHE photons has been providing the largest obstacle to probe the VHE emission, independent of the emission models. One may argue that it is only a matter of time as whether the first VHE photons will be detected. How long we have to wait may simply rely on the happening rate of a nearby GRB. As pointed out in the discussion part of Chapter 5, the rate of nearby, energetic GRBs (such as GRB 030329) is not clear. If GRB 940217 was also nearby, the event rate would be ~ 1 in a few years. A distinct population of low-luminosity (LL) GRBs ($E_{GRB} \lesssim 10^{49}$ erg s^{-1}) from that of high-luminosity (HL) GRBs ($E_{GRB} \gtrsim 10^{49}$ erg s^{-1}) was suggested based on the high detection rate of low-redshift LL GRBs (e.g. GRB 980425 and GRB 060218; Liang et al., 2007; Guetta & Della Valle, 2007). A study on the predicted VHE emission from these LL GRBs and their event rate is needed to answer this question.

- For HL GRBs which happened at an average redshift of $z \sim 1 - 2$, the detection prospects depend on the opacity of the intergalactic medium to VHE γ-rays due to absorption by the EBL in the infrared and optical ranges. The EBL level has not been well understood and different modelers come up with different levels (Kneiske et al., 2004; Primack et al., 2005; Stecker et al., 2006). A very low EBL level was suggested by Franceschini et al. (2008). It is obvious that a low EBL level implies a larger horizon for VHE γ-rays. Therefore, on-going GRB observations with H.E.S.S., as well as other ground-based VHE detectors, are crucial to test this model. A future IACT array (such as the planned CTA or AGIS) equipped with

a low energy threshold would open a new window to probe the high energy regime from a larger fraction of GRBs.

References

Abdo, A. A., et al. 2007, ApJ, 666, 361

Aharonian, F. A., & Atoyan, A. M. 1981, Ap&SS, 79, 321

Aharonian, F. A., et al. (HEGRA collaboration) 1998, Nuclear Physics B Proceedings Supplements, 60, 193

Aharonian, F. A., et al. (H.E.S.S. collaboration) 2005a, A&A, 436, L17

Aharonian, F. A., et al. (H.E.S.S. collaboration) 2005a, A&A, 437, 135

Aharonian, F. A., et al. (H.E.S.S. collaboration) 2005b, A&A, 442, 1

Aharonian, F. A., et al. (H.E.S.S. collaboration) 2005c, Science, 307, 1938

Aharonian, F. A., et al. (H.E.S.S. collaboration) 2006a, A&A, 448, L19

Aharonian, F. A., et al. (H.E.S.S. collaboration) 2006b, A&A, 457, 899

Aharonian, F. A., et al. (H.E.S.S. collaboration) 2006c, A&A, 460, 743

Aharonian, F. A., et al. (H.E.S.S. collaboration) 2006d, Nature, 440, 1018

Aharonian, F. A., et al. (H.E.S.S. collaboration) 2008a, A&A, 477, 481

Aharonian, F. A., Buckley, J., Kifune, T., & Sinnis, G. 2008b, Reports on Progress in Physics, 71, 096901

Aharonian, F. A., et al. (H.E.S.S. collaboration) 2009, ApJ, in press, preprint [arXiv:0809.2334]

Albert, J., et al. (MAGIC collaboration) 2006a, ApJ, 641, L9

Albert, J., et al. (MAGIC collaboration) 2006b, Science, 312, 1771

Albert, J., et al. (MAGIC collaboration) 2007a, ApJ, 667, L21

Albert, J., et al. (MAGIC collaboration) 2007b, ApJ, 667, 358

Albert, J., et al. (MAGIC collaboration) 2008, Science, 320, 1752

Alvarez, C., et al. 2005, 29th ICRC proceeding, 4, 443

Amati L., et al. 2008, MNRAS, in press, preprint [arXiv:0805.0377]

Amenomori, M. et al. 1996, A&A, 311, 919

Asano, K., & Inoue, S. 2007, ApJ, 671, 645

Asano, K., Inoue, S., & Mészáros, P. 2008, submitted, [arXiv:0807.0951]

Atkins, R., et al. 2000, ApJ, 533, L119

Atkins, R., et al. 2003, ApJ, 583, 824

Atkins, R., et al. 2004, ApJ, 604, L25

Atkins, R., et al. 2005, ApJ, 630, 996

Band, D. L., et al. 1993, ApJ, 413, 281

Baring, M. G. 2006, ApJ, 650, 1004

Barthelmy, S. D. 2007, GCN Circ. 6013

Barthelmy, S. D., et al. 1994, AIP Conference Proceedings, 307, 643

Beardmore, A. P., Godet, O., & Sakamoto, T. 2006, GCN Circ. 5209

Belian, R. D., Conner, J. P., & Evans, W. D. 1976, ApJ, 206, L135

Berge, D., Funk, S., & Hinton, J. A. 2007, A&A, 466, 1219

Berger, E., & Fox, D. 2007, GCN Circular 6101

Berger, E., & Gladders, M. 2006, GCN Circular 5170

Berger, E., et al. 2003, Nature, 426, 154

Berger, E., Fox, D. B., Price, P. A., et al. 2007, ApJ, 664, 1000

Blandford, R. D., & Königl, A. 1979, ApJ, 232, 34

Bloom, J., Blake, C., Prochaska, J. X., Hennawi, J., Gladders, M., & Koester, B. 2005, GCN Circ. 3386

Bloom, J. S., et al. 2006, ApJ, 638, 354

Blumenthal, G. R., & Gould, R. J. 1970, Reviews of Modern Physics, 42, 237

Blustin, A. J., Schady, P., & Pandey, S. B. 2006, GCN Circ. 5207

Butler, N. R. 2007, AJ, 133, 1027

Böttcher, M., & Dermer, C. D. 1998, ApJ, 499, L131

Böttcher, M., & Dermer, C. D. 2000, ApJ, 529, 635

Böttcher,M., & Schlickeiser, R. 1997, Astropart. Phys., 325, 866

Bouvier, A. et al. 2008, GCN Circular 8183

Briggs, M. S., et al. 1999, ApJ, 524, 82

Burrows, D. N., et al. 2006, ApJ, 653, 468

Cabrera, R., et al. 1999, A&AS, 138, 599

Cantanese, M., et al. 1998, ApJ, 501, 616

Chadwick, P. M., et al. 1999, Astropart. Phys., 11, 145

Chelovekov, I. V., Grebenev, S. A., & Sunyaev, R. A. 2006, Astronomy Letters, 32, 456
    (originally published in Russian language in 2006, AZh, 32, 508)

Chelovekov, I. V., Grebenev, S. A., & Sunyaev, R. A. 2007, ESA SP-622, p.445, preprint
    [arXiv:0709.2328]

Cheng, K. S. 2005, Radiation Processes in Lecture Notes of the course 'Astrophysics' at
    the University of Hong Kong, chapter 2

Cheng, K. S., & Ruderman, M. 1991, ApJ, 373, 187

Cheng, K. S., & Wei, D. M. 1996, MNRAS, 283, L133

Chincarini, G., et al. 2007, ApJ, 671, 1903

Cobb, B. E., Bailyn, C. D., van Dokkum, P. G., & Natarajan, P. 2006, ApJ, 651, L85

Cohen, E., & Piran, T. 1999, ApJ, 518, 346

Conciatore, M. L., Capalbi, M., Vetere, L., Palmer, D., & Burrows, D. 2006, GCN Circ.
    5078

Connaughton, V., et al. 1997, ApJ, 479, 859

Connaughton, V., et al. 1998, Astropart. Phys., 8, 179

Coppi, P. S., & Blandford, R. D. 1990, MNRAS, 245, 453

Cornelisse, R., et al. 2004, Nuclear Physics B Proceedings Supplements, 132, 518

Costa, E., et al. 1997, Nature, 387, 783

Covino, S., et al. 2006, A&A, 447, L5

Coward, D. M., Guetta, D., Burman, R. R., & Imerito, A. 2008, MNRAS, 386, 111

Cucchiara, A., et al. 2007, GCN Circular 6665

Cummings, J., et al. 2005, GCN Circ. 4365

Curran, P. A., Starling, R. L. C., O'Brien, P. T., et al. 2008, A&A, 487, 533

Dai Z. G., & Lu T., 1998, A&A, 333, L87

Dar, A. & De Rújula, A. 2004, Physics Reports, 405, 203

Derishev, E. V., Kocharovsky, V. V., & Kocharovsky, V. V. 2001, A&A, 372, 1071

Dermer, C. D. 1996, AIP Conference Proceedings, 384, 744

Dermer, C. D. 2007, ApJ, 664, 384

Dermer, C. D. 2008, ApJ, 684, 430

Dermer, C. D., Chiang, J., & Mitman, K. E. 2000, ApJ, 537, 785

Dickinson, H., Latham, I., Chadwick, P., et al. 2008, 30th ICRC proceeding, submitted, preprint [arXiv:0710.4057, p.59]

Dingus, B. L. 1995, Ap&SS, 231, 187

Evans, P. A., Beardmore, A. P., & Page, K. L., et al. 2007, A&A, 469, 379

Falcone, A. D., et al. 2007, ApJ, 671, 1921

Fan, Y.-Z., & Piran, T. 2008, Frontiers of Physics in China, 3, 306

Fan, Y.-Z., & Xu, D. 2006, MNRAS, 372, L19

Fan, Y.-Z., Piran, T., Narayan, R., & Wei, D.-M. 2008, MNRAS, 384, 1483

Fan, Y.-Z., Piran, T., & Wei, D.-M. 2008, AIP Conference Proceedings, 968, 32

Feldman, G. J., & Cousins, R. D. 1998, Phys. Rev. D, 57, 3873

Fiore, F., Guetta, D., Piranomonte, S., D'Elia, V., & Antonelli, L. A. 2007, A&A, 470, 515

Fishman, G. J., & Meegan, C. A. 1995, ARA&A, 33, 415

Fox, D. B., Frail, D. A., Cameron, P. B., & Cenko, S. B. 2005, GCN Circ. 3585

Frail, D. A., et al. 2001, ApJ, 562, L55

Franceschini, A., Rodighiero, G., & Vaccari, M. 2008, A&A, 487, 837

Fugazza, D., et al. 2006, GCN Circ. 5276

Funk, S., Hermann, G., Hinton, J. A. et al. 2004, Astropart. Phys., 22, 285

Galama, T. J., Wijers, R. A. M. J., Bremer, M., Groot, P. J., Strom, R. G., Kouveliotou, C., & van Paradijs, J. 1998, ApJ, 500, L97

Galli, A., & Guetta, D. 2008, A&A, 480, 5

Galli, A., & Piro, L. 2007, A&A, 475, 421

Galli, A., & Piro, L. 2008, A&A, 489, 1073

Galloway, D. K., Muno, M. P., Hartman, J. M., Psaltis, D., & Chakrabarty, D. 2006, A&AS, in press, preprint [astro-ph/0608259]

Gehrels, N., et al. 2005, Nature, 437, 851

Ghisellini, G., & Celotti, A. 1999, ApJ, 511, L93

Ghisellini, G., Celotti, A., & Lazzati, D. 2000, MNRAS, 313, L1

Golenetskii, S., Aptekar, R., Mazets, E., Pal'shin, V., Frederiks, D., & Cline, T. 2006, GCN Circ. 5264

González, M. M., Dingus, B. L., Kaneko, Y., Preece, R. D., Dermer, C. D., & Briggs, M. S. 2003, Nature, 424, 749

Götting, N. & Horns, D. 2001, GCN Circ. 1007

Gou, L. J., & Mészáros, P. 2007, ApJ, 668, 392

Granot, J., Cohen-Tanugi, J., & do Couto e Silva, E. 2008, ApJ, 677, 92

Greiner, J. 1999, Memorie della Societa Astronomica Italiana, 70, 891

Greiner, J., et al. 2003, GCN, 2020

Grindlay, J., et al. 1976, ApJ, 205, L127

Guetta, D. & Della Valle, M. 2007, ApJ, 657, L73

Guetta, D. & Granot, J. 2003, MNRAS, 340, 115

Gupta, N., & Zhang, B. 2007, MNRAS, 380, 78

Halpern, J. 2006, GCN Circ. 5210

Hameury, J. M., Bonazzola, S., Heyvaerts, J., & Ventura, J. 1982, A&A, 111, 242

Hartmann, D. & Woosley, S. E. 1988, X-Ray and γ-Ray Bursts, in Multiwavelength Astrophysics, ed. F. Córdova (Cambridge University Press), 189

Heise J. & in 't Zand, J. 1998, IAU Circ. 6892

Heise J., in 't Zand, J., Kippen, R. M., & Woods, P. M. 2001, in Gamma-Ray Bursts in the Afterglow Era, ed. E. Costa, F. Frontera, & J. Hjorth (Berlin: Springer), p. 16

Hillas, A. M. 1996, Space Sci. Rev., 75, 17

Hinton, J. A. 2004, NewA Rev., 48, 331

Hinton, J. A. 2008, New Journal of Physics, in press, preprint [arXiv:0803.1609]

Hjorth, J., et al. 2005, Nature, 437, 859

Horan, D., et al. 2002, ApJ, 571, 753

Horan, D., et al. 2007, ApJ, 655, 396

Horan, D., et al. 2008, submitted to 30th ICRC proceeding, preprint [arXiv:0709.3830]

van der Horst, A. J., & Connaughton, V. 2008, GCN Circ. 8141

van der Horst, A. J., et al. 2008, A&A, 480, 35

Huang, Y. F., Cheng, K. S., Gao, T. T. 2006, ApJ, 637, 873

Huang, Y. F., Gou, L. J., Dai, Z. G. & Lu, T. 2000, ApJ, 543, 90

Hullinger, D., et al. 2006, GCN Circ. 5142

Hurley, K., Cline, T., & Mazets, E., et al. 2003, GCN Circular 2359

Hurley, K., Dingus, B. L., Mukherjee, R., et al. 1994, Nature, 372, 652

Jakobsson, P., Levan, A., Fynbo, J. P. U., et al. 2006, A&A, 447, 897

Jarvis, A., et al. 2008, submitted to 30th ICRC proceeding, preprint [arXiv:0710.4149]

Jensen, B. L., et al. 2005, GCN Circ. 3589

Kaneko, Y., Gonzalez, M. M., Preece, R., Dingus, B. L., & Briggs, M. S. 2008, ApJ, 677, 1168

Kasliwal, M. M., et al. 2008, ApJ, 678, 1127

Katz, J. I. 1994, ApJ, 432, L107

Khamitov, I., Bikmaev, I., Sakhibullin, N., Aslan, Z., Kiziloglu, U., Gogus, E., Burenin, R., & Pavlinsky, M. 2006, GCN Circ. 5205

Király, P., & Mészáros, P. 1988, ApJ, 333, 719

Klebesadel, R. W., Strong, I. B., & Olson, R. A. 1973, ApJ, 182, L85

Kneiske, T. M., Bretz, T., Mannheim, K., & Hartmann, D. H. 2004, A&A, 413, 807

Kneiske, T. M., Mannheim, K., & Hartmann, D. H. 2002, A&A, 386, 1

Kong, A. K. H. 2006, ATel #875

Konopelko, A., Hemberger, M., Aharonian, F. et al. (HEGRA Collaboration) 1999, Astropart. Phys., 10, 275

Kubánek, P., Jelínek, M., & French, J. 2006, GCN Circ. 5199

Kumar, P., & McMahon, E. 2008, MNRAS, 384, 33

Kumar, P., & Panaitescu, A. 2008, MNRAS, 391, L19

Kuulkers, E., den Hartog, P. R., in't Zand, J. J. M., Verbunt, F. W. M., Harris, W. E., & Cocchi, M. 2003, A&A, 399, 663

LeBohec, S. & Holder, J. 2003, Astropart. Phys., 19, 221

Lewin, W. H. G., van Paradijs, J., & van den Heuvel, E. P. J. 1993, Space Sci. Rev., 62, 223

Lewin, W. H. G., van Paradijs, J., & van den Heuvel, E. P. J. 1995, X-Ray Binaries (Cambridge University Press, Cambridge) 178

Li, T.-P., & Ma, Y.-Q. 1983, ApJ, 272, 317

Liang, E., Zhang, B., Virgili, F., & Dai, Z. G. 2007, ApJ, 662, 1111

Linares, M., Watts, A., Wijnands, R., et al. 2008, MNRAS, in press, preprint [arXiv:0808.3950]

Lipkin, Y. M., et al. 2004, ApJ, 606, 381

Lithwick, Y., & Sari, R. 2001, ApJ, 555, 540

Liu, Q. Z., van Paradijs, J., & van den Heuvel, E. P. J. 2001, A&A, 368, 1021

Lyutikov, M., & Blandford, R. 2003, arXiv:astro-ph/0312347

Malesani, D., Jakobsson, P., Fynbo, J. P. U., Hjorth, J., & Vreeswijk, P. M. 2007, GCN Circular 6651

Melandri, A., et al. 2006, GCN Circ. 5229

Mészáros, P. 2006, Rep. Prog. Phys., 69, 2259

Mészáros, P., & Rees, M. J. 1994, MNRAS, 269, L41

Mészáros, P., & Rees, M. J. 1997, ApJ, 476, 232

Meszaros, P., Rees, M. J., & Papathanassiou, H. 1994, ApJ, 432, 181

Metzger, M. R., Djorgovski, S. G., Kulkarni, S. R., Steidel, C. C., Adelberger, K. L., Frail, D. A., Costa, E., & Frontera, F. 1997, Nature, 387, 878

Moderski, R., Sikora, M., & Bulik, T., 2000, ApJ, 529, 151

Murase, K., Ioka, K., Nagataki, S., & Nakamura, T. 2008, Phys. Rev. D, 78, 023005

Narayan, R., Paczynski, B., & Piran, T. 1992, ApJ, 395, L83

de Naurois, M. 2005, in proceedings of the conference *Towards a Network of Atmospheric Cherenkov Detectors VII*, Palaiseau, France, preprint [astro-ph/0607247]

Nikishov, A. I., 1962, Sov. Phys. JETP, 14, 393

Nousek, J. A., Kouveliotou, C., Grupe, D., et al. 2006, ApJ, 642, 389

Ofek, E. O., Cenko, S. B., Gal-Yam, A., Peterson, B., Schmidt, B. P., Fox, D. B., & Price, P. A. 2006, GCN Circ. 5123

Ofek, E. O., Cenko, S. B., Gal-Yam, A., et al. 2007, ApJ, 662, 1129

Paczynski, B., & Rhoads, J. E. 1993, ApJ, 418, L5

Padilla, L., et al. 1998, A&A, 337, 43

Palmer, D., Cummings, J., Stamatikos, M., Markwardt, C., & Sakamoto, T. 2006a, GCN Circular 5076

Palmer, D., et al. 2006b, GCN Circ. 5208

Panaitescu, A. 2006, MNRAS, 367, L42

Panaitescu, A. 2008, MNRAS, 385, 1628

Panaitescu, A., & Kumar, P. 2002, ApJ, 571, 779

Panaitescu, A., Mészáros, P., Burrows, D., et al. 2006, MNRAS, 369, 2059

van Paradijs, J., Kouveliotou, C., & Wijers, R. A. M. J., 2000, ARA&A, 38, 379

Parsons, A. M., et al. 2006, GCN Circ. 5252

de Pasquale, M., et al. 2007, MNRAS, 377, 1638

Pe'er, A. & Waxman, E. 2004, ApJ, 613, 448

Pe'er, A. & Waxman, E. 2005, ApJ, 633, 1018

Pe'er, A., Mészáros, P., & Rees, M. J. 2007, Royal Society of London Philosophical Transactions Series A, 365, 1171

Pélangeon, A. & Atteia, J.-L., retrieved from http://cosmos.ast.obs-mip.fr/projet/catalog_pz.php at August 18, 2008

Pélangeon, A., Atteia, J.-L., Lamb, D. Q., & Ricker, G. R. 2006, AIPC, 836, 149

Perley, D. A., Li, W., Chornock, R., et al. 2008, ApJ, in press, preprint [arXiv:0805.2394]

Pilla, R. P., & Loeb, A. 1998, ApJ, 494, L167

Piran, T. 1999, Phys. Rep., 314, 575

Piran, T. 2005, Reviews of Modern Physics, 76, 1143

Piran, T., Sari, R., & Zou, Y.-C. 2008, arXiv:0807.3954

Poirier, J., D'Andrea, C., Fragile, P. C., Gress, J., Mathews, G. J., & Race, D. 2003, Phys. Rev. D, 67, 042001

Porter, N. A. & Weekes, T. C. 1978, MNRAS, 183, 205

Preece, R. D., Briggs, M. S., Giblin, T. W., Mallozzi, R. S., Pendleton, G. N., Paciesas, W. S., & Band, D. L. 2002, ApJ, 581, 1248

Preece, R. D., Briggs, M. S., Mallozzi, R. S., Pendleton, G. N., Paciesas, W. S., & Band, D. L. 1998, ApJ, 506, L23

Preece, R. D., Briggs, M. S., Mallozzi, R. S., Pendleton, G. N., Paciesas, W. S., & Band, D. L. 2000, ApJS, 126, 19

Price, P. A., Berger, E., & Fox, D. B., 2006, GCN Circ. 5275

Price, P. A., Roth, K., & Fox, D. W. 2005, GCN Circ. 3605

Primack, J. R., Bullock, J. S., & Somerville, R. S. 2005, AIP Conference Proceedings, 745, 23

Primack, J. R., Somerville, R. S., Bullock, J. S., & Devriendt, J. E. G. 2001, APIC Proc., 558, 463

Prochaska, J. X., Bloom, J. S., Chen, H.-W., & Hurley, K. 2005, GCN Circ. 3399

Punch, M., et al. 1992, Nature, 358, 477

Quinn, J., et al. 1996, ApJ, 456, L83

Racusin, J. L., Karpov, S. V., Sokolowski, M., et al. 2008, Nature, 455, 183

Razzaque, S., Mészáros, P., & Zhang, B. 2004, ApJ, 613, 1072

Rhoads, J. E., 1999, ApJ, 525, 737

Romano, P., Barthelmy, S. D., Gehrels, N. et al. 2006, GCN Circ. 5436

Romano, P., Guidorzi, C., Sidoli, L. et al. 2008, GAMMA-RAY BURSTS 2007: Proceedings of the Santa Fe Conference, preprint [arXiv:0806.0925]

Ruderman, M. 1975, New York Academy Sciences Annals, 262, 164

Rybicki, G. B., & Lightman, A. P., 1979, *Radiative Processes in Astrophysics,* New York: Wiley

Sakamoto, T., Barthelmy, S. D., Barbier, L. et al. 2008a, ApJS, 175, 179

Sakamoto, T., Barthelmy, S. D., Beardmore, A. P. 2008b, GCN Circ. 8034

Sakamoto, T., Hullinger, D., Sato, G., et al. 2008c, ApJ, 679, 570

Sakamoto, T., Lamb, D. Q., Kawai, N., et al. 2005, ApJ, 629, 311

Sari, R., & Esin, A. A. 2001, ApJ, 548, 787

Sari, R., Piran, T., & Halpern, J. P., 1999, ApJ, 519, L17

Sari, R., Piran, T., & Narayan, R., 1998, ApJ, 497, L17

Sbarufatti, B., et al. 2007, GCN Report 67.2

Schady, P., Beardmore, A. P., Marshall, F. E., Palmer, D. M., Rol, E., & Sato, G. 2006, GCN Circ. 5200

Schaefer, B. E., et al. 1998, ApJ, 492, 696

Schmidt, B., Peterson, B., & Lewis, K. 2006, GCN Circ. 5258

di Sciascio, G., & di Girolamo, T. 2007, Ap&SS, 309, 537

Share, G. H., et al. 1986, Adv. Space Res., 6, 15

Shaviv, N. J., & Dar, A. 1995, ApJ, 447, 863

Shemi, A. 1994, MNRAS, 269, 1112

Shirasaki, Y., Yoshida, A., Kawai, N., et al. 2008, PASJ, 60, 919

Soderberg, A. M., et al. 2006a, ApJ, 636, 391

Soderberg, A. M., et al. 2006b, ApJ, 650, 261

Stamatikos, M., Barbier, L., Barthelmy, S. D., et al. 2007, GCN Circular 6711

Stanek, K. Z., Matheson, T., Garnavich, P. M. et al. 2003, ApJ, 591, L17

Stecker, F. W., Malkan, M. A., & Scully, S. T. 2006, ApJ, 648, 774

Stern, B. E., & Poutanen, J. 2004, MNRAS, 352, L35

Svensson, R. 1987, MNRAS, 227, 403

Tam, P. H., Chadwick, P., Gallant, Y., Horns, D., Pühlhofer, G., Rowell, G., & Wagner, S. 2008, submitted to 30th ICRC proceeding, preprint [arXiv:0710.4057, p.157]

Tavani, M. 1996, ApJ, 466, 768

Thoene, C. C., Fynbo, J. P. U., Sollerman, J., Jensen, B. L., Hjorth, J., Jakobsson, P., & Klose, S. 2006, GCN Circ. 5161

Tiengo, A., Mereghetti, S., Ghisellini, G., Tavecchio, F., & Ghirlanda, G. 2004, A&A, 423, 861

Tikhomirova, Y., Stern, B. E., Kozyreva, A., & Poutanen, J. 2006, MNRAS, 367, 1473

Totani, T. 1998a, ApJ, 502, L13

Totani, T. 1998b, ApJ, 509, L81

Totani, T., & Takeuchi, T. T. 2002, ApJ, 570, 470

Vanderspek, R., et al. 2004, ApJ, 617, 1251

Villasenor, J. S, et al. 2005, Nature, 437, 855

Wang, X. Y., Dai, Z. G., & Lu, T. 2001, ApJ, 556, 1010

Wang, X. Y., Li, Z., & Mészáros, P. 2006, ApJ, 641, L89

Watson et al. 2008, "The XMM-Newton Serendipitous Survey. VI. The Second XMM-Newton Serendipitous Source Catalogue", submitted

Waxman, E. 2006, Nuclear Physics B (Proc. Suppl.), 151, 46

Waxman, E., & Bahcall, J. N. 2000, ApJ, 541, 707

Weekes, T. C. 1992, Space Sci. Rev., 59, 315

Weekes, T. C. 2003, Very high energy gamma-ray astronomy, ch. 1. pp. 5, London, UK: Institute of Physics Publishing.

Weekes, T. C., et al. 1989, ApJ, 342, 379

Wei, D.-M., & Fan, Y.-Z., 2007, ChJAA, 7, 509

Wei, D.-M., & Lu, T., 1998, ApJ, 505, 252

Wei, D.-M., & Lu, T., 2000, A&A, 360, L13

Wijnands, R., Rol, E., Cackett, E. M., Starling, R. L. C., & Remillard, R. A. 2008, MNRAS, in press, preprint [arXiv:0709.0061]

Woosley, S. E., & Wallace, R. K. 1982, ApJ, 258, 716

Xu, D., et al. 2009, in preparation

Yost, S. A., Aharonian, F., Akerlof, C. W., et al. 2007a, ApJ, 669, 1107

Yost, S. A., Swan, H. F., Rykoff, E. S., et al. 2007b, ApJ, 657, 925

Yu, Y. W., Liu, X. W., & Dai, Z. G. 2007, ApJ, 671, 637

Zdziarski, A. A., Svensson, R., & Paczyński, B. 1991, ApJ, 366, 343

Zhang, B., & Mészáros, P. 2001a, ApJ, 552, L35

Zhang, B., & Mészáros, P. 2001b, ApJ, 559, 110

Zhang, B., & Mészáros, P. 2004, Int. J. Mod. Phys. A., 19, 2385

Zhang, B., Fan, Y. Z, Dyks, J., Kobayashi, S., Mészáros, P., Burrows, D. N., Nousek, J. A., & Gehrels, N. 2006, ApJ, 642, 354

Zhou, X. X. 2003, 30th ICRC proceeding, p. 2757

Acknowledgments